Geophysical Imaging of Earth Processes: Electromagnetic Induction in Rough Geologic Media, and Back-Projection Imaging of Earthquake Aftershocks

Güngör Didem Beşkardeş

Dissertation submitted to the Faculty of the
Virginia Polytechnic Institute and State University
in partial fulfillment of the requirements for the degree of

Doctor of Philosophy
in
Geosciences

John A. Hole, Chair
Chester J. Weiss
Martin C. Chapman
Ying Zhou
James A. Spotila

May 5, 2017
Blacksburg, Virginia

Keywords: Electromagnetic induction, Numerical Modeling, Multiscale heterogeneity, Backprojection imaging, Dense arrays, Virginia earthquake

Geophysical Imaging of Earth Processes: Electromagnetic Induction in Rough Geologic Media, and Back-Projection Imaging of Earthquake Aftershocks

Güngör Didem Beşkardeş

ABSTRACT

This dissertation focuses on two different types of responses of Earth; that is, seismic and electromagnetic, and aims to better understand Earth processes at a wider range of scales than those conventional approaches offer.

Electromagnetic responses resulting from the subsurface diffusion of applied electromagnetic fields through heterogeneous geoelectrical structures are utilized to characterize the underlying geology. Geology exhibits multiscale hierarchical structure which brought about by almost all geological processes operating across multiple length scales and the relationship between multiscale electrical properties of underlying geology and the observed electromagnetic response has not yet been fully understood. To quantify this relationship, the electromagnetic responses of textured and spatially correlated, stochastic geologic media are herein presented. The modelling results demonstrate that the resulting electromagnetic responses present a power law distribution, rather than a smooth response polluted with random, incoherent noise as commonly assumed; moreover, they are examples of fractional Brownian motion. Furthermore, the results indicate that the fractal behavior of electromagnetic responses is correlated with the degree of the spatial correlation, the contrasts in ground electrical conductivity, and the preferred orientation of small-scale heterogeneity. In addition, these inferences are also supported by the observed electromagnetic responses from a fault zone comprising different lithological units and varying wavelengths of geologic heterogeneity.

Seismic signals generated by aftershocks are generally recorded by local aftershock networks consisted of insufficient number of stations which result in strongly spatially-aliased aftershock data. This limits aftershock detections and locations at smaller magnitudes. Following the 23 August 2011 Mineral, Virginia earthquake, to drastically reduce spatial aliasing, a temporary dense array (AIDA) consisting of ~200 stations at 200-400 m spacing was deployed near the epicenter to record the 12 days of the aftershocks. The backprojection imaging method is applied to the entire AIDA dataset to detect and locate aftershocks. The method takes advantage of staking of many seismograms and improves the signal-to-noise ratio for detection. The catalog obtained from the co-deployed, unusually large temporal

traditional network of 36 stations enabled a quantitative comparison. The aftershock catalog derived from the dense AIDA array and the backprojection indicates event detection an order of magnitude smaller including events as small as M–1.8. The catalog is complete to magnitude –1.0 while the traditional network catalog was complete to M–0.27 for the same time period. The AIDA backprojection catalog indicate the same major patterns of seismicity in the epicentral region, but additional details are revealed indicating a more complex fault zone and a new shallow cluster. The b-value or the temporal decay constant were not changed by inclusion of the small events; however, they are different for two completeness periods and are different at shallow depth than greater depth.

Geophysical Imaging of Earth Processes: Electromagnetic Induction in Rough Geologic Media, and Back-Projection Imaging of Earthquake Aftershocks

Güngör Didem Beşkardeş

GENERAL AUDIENCE ABSTRACT

This dissertation revolves around two ends of geophysics: seismology and electromagnetics.

The electromagnetic method of exploration geophysics aims to characterize the underlying geology by evaluating the electromagnetic responses resulting from the interaction between the applied electromagnetic fields and the subsurface electrical properties. In case of rough geology comprising heterogeneity at every scale, the electromagnetic responses are more complicated than the response of a piecewise smooth Earth structure. Most analyses treat the responses of small-scale heterogeneities as random, uncorrelated noise. Here, more realistic geologic models comprising spatially-correlated, fine-scale heterogeneities are incorporated into electromagnetic modeling to better understand the relationship between the causative multiscale geoelectrical heterogeneities and the electromagnetic responses. The numerical results indicate that these electromagnetic responses are not random as commonly assumed, in contrast, they are repeatable and fractally distributed presenting spatial fluctuations that appear on all length scales. Moreover, the numerical results indicate that the fractal behavior of electromagnetic responses is correlated with the degree of the spatial correlation, the contrasts in ground electrical conductivity, and the preferred orientation of small-scale heterogeneity. In addition, the analysis of the observed electromagnetic responses from a fault zone comprising multiscale heterogeneity also support these inferences.

Seismic signals generated by aftershocks are generally recorded by local aftershock networks consisted of insufficient number of stations which result in strongly spatially-aliased aftershock data. This limits aftershock detections and locations at smaller magnitudes. Following the 23 August 2011 Mineral, Virginia earthquake, to drastically reduce spatial aliasing, a temporary dense array (AIDA) consisting of ~200 stations at 200-400 m spacing was deployed near the epicenter to record the 12 days of the aftershocks. The backprojection imaging method is applied to the entire AIDA dataset to detect and locate aftershocks. The method takes advantage of summing of many seismograms and improves the signal-to-noise ratio for detection. The catalog obtained from the co-deployed, unusually large temporal traditional network of 36 stations enabled a quantitative comparison. The aftershock cat-

alog derived from the dense AIDA array and the backprojection indicates event detection an order of magnitude smaller. The AIDA backprojection catalog indicate the same major patterns of seismicity in the epicentral region, but additional details are revealed indicating a more complex fault zone and a new shallow cluster. The decay of aftershock rate and the distribution of earthquakes with respect to the magnitude do not show a significant change by inclusion of the small events; however, they differ at shallow and greater depth, and for different completeness periods.

In dedication to my mother, Hediye Beskardes

Acknowledgments

I would like to express my sincere gratitude to my advisor, Dr. John A. Hole for his patient guidance, mentoring and unwavering support during my time at Virginia Tech. I am grateful to my previous advisor and my current committee member, Dr. Chester J. Weiss for his mentoring and continuous support. Thanks also go to my committee members: Dr. Martin Chapman, Dr. Ying Zhou and Dr. James A. Spotila for their insightful comments that contributed greatly to enrich this dissertation. I especially thank Dr. Chapman for his support and advice.

I would like to thank my fellow graduate students for sharing this adventure with me and making my stay in Blacksburg much more pleasurable. I would particularly like to thank Qimin Wu and Kannikha Kolandaivelu for their support and encouragement.

I thank the office and the technical staff of the Department of Geosciences at Virginia Tech, especially thank Connie Lowe, Mark Lemon and Marry McMurray.

I will always be grateful to my mentor Dr. Emin U. Ulugergerli for being great professor and helping me realize my potential.

Most of all, I would like to thank my family for their love and support. I am especially indebted to the efforts made by my parents.

Contents

List of Figures

List of Tables

Chapter 1

Introduction

This dissertation focuses on two different types of responses of Earth; that is, seismic and electromagnetic, and aims to reveal more information regarding the underlying geology beyond the resolution limit that conventional approaches offer.

1.1 Electromagnetic responses over multi-scale heterogeneous media

Electromagnetic methods of geophysical exploration are used to map variations in electrical conductivity of the subsurface. The electromagnetic responses resulting from the diffusion of induced electromagnetic fields through geoelectrical structures are assessed to characterize the underlying geology. The electromagnetic methods can be carried out in frequency or time domain, and employ either active (controlled-source) or passive sources. Nowadays, the controlled-source electromagnetic systems allow to operate in land, airborne, marine and borehole environments, and have a wide range of applications including geological imaging (Everett and Edwards, 1993), mining studies (Meju, 2002), hydrocarbon exploration studies (Edwards, 1988; Eidesmo et al., 2002; Wilt and Alumbaugh, 1998), environmental studies (Tezkan, 1999), and hydrogeological studies (Meju et al., 2002), etc.

Almost all geological processes (sedimentary, igneous and metamorphic), that show spatial and temporal variability, operate across multiple length scales from the mineral scale to the continental scale. The resulting underlying geology is therefore inherently rough and comprises heterogeneity at every scale. The electromagnetic diffusion process through a piecewise smooth Earth structure is well described by the familiar Maxwell equations; however, the relationship between the causative multiscale geoelectrical heterogeneities and the

electromagnetic responses has not yet been fully clarified.

Most studies treat fine-scale heterogeneities too small to be individually modelled as random and uncorrelated (white) noise. In contrast, the observational controlled-source electromagnetic study of Everett and Weiss (2002) indicated that underlying geology comprising geoelectrical heterogeneity produces correlated, repeatable electromagnetic responses whose spatial fluctuations span multiple length scales. Moreover, they showed that these electromagnetic responses are examples of fractional Brownian motion, a class of non-stationary signals (Mandelbrot and van Ness, 1968). Conventional modeling approaches oversimplify the multiscale heterogeneity of Earth structure as a coarse, piecewise smooth medium and do not enable to account for the responses of small-scale heterogeneities. This results in a lack of understanding of the relationship between the roughness of EM responses and the roughness of the causative geoelectrical structure, and can lead misinterpretations.

Chapter 2 focuses on developing a better understanding of the relationship between multiscale electrical properties and the observed electromagnetic responses. Fine-scale heterogeneities produced by spatially correlated rock textures are incorporated into classical controlled-source electromagnetic forward modeling. Conductivity models possessing different directions and correlation lengths of small scale heterogeneity are considered. The power-density functions of the resulting electromagnetic responses are examined to better understand the fractal properties of these responses. In addition, a real data example from a fault zone that is a good representative of multiscale hierarchical structure is presented.

A version of this manuscript was published as Beskardes, G.D., Weiss C.J. and Everett M.E., 2017. Estimating the power-law distributions of Earth electrical conductivity from

low-frequency, controlled source electromagnetic data, *Geophysical Journal International*, 208, no. 2, pp. 639–651.

1.2 Imaging aftershocks by using dense arrays

Earthquake rupture changes stress and cause aftershocks to occur in regions where stress increases (King et al., 1994). Aftershocks provide valuable information about the complex geometry of the main shocks rupture plane and the spatiotemporal distribution of the released tectonic stress. Regardless of their weak energies, they can sometimes be more damaging than the mainshock since they shake already weakened structures. Therefore, studying aftershock sequences is important to better understand earthquake sources, spatiotemporal evolution of stress and postseismic strain as well as future seismic hazards.

Aftershocks are generally recorded by local permanent seismic networks consisted of a few dozen stations. The sparse distribution of traditional network stations result in spatially aliased records of earthquake wavefields and consequently, limits aftershock detections at smaller magnitudes as well as attainable accuracies of aftershock locations. The resultant aftershock catalogs derived from these traditional network datasets are inherently incomplete and therefore, do not properly delineate active fault zones. On the other hand, well-sampled aftershock datasets enable to capture non- or weakly aliased earthquake wavefields rather than isolated waveforms, and enable detections for small magnitude and low signal-to-noise events through trace-to-trace correlation. Moreover, such datasets allow to employ array analysis methods (e.g. Davenport et al., 2015, Quiros et al., in press). It is feasible to image real earthquake sources at higher spatial resolution compared to traditional location

algorithms, by using reflector imaging methods such as migration or back-projection (e.g. McMechan, 1982; McMechan, 1985; Ishii et al., 2005). The aftershock catalogs derived from densely-sampled aftershock data and such imaging methods has great potential to produce a more complete characterization of seismicity that allows to better delineate earthquake source processes, detailed fault geometries, the evolving state of stress, dynamic and static stress triggering, and the geologic features that control stress and strength.

The M_w5.8 earthquake occurred on 23 August 2011 near Mineral, Virginia. This event was the most widely-felt earthquake in US history. Shortly after the main shock, to illustrate the merits of dense arrays, a local dense (AIDA) array was deployed over the main shock and primary aftershock cluster (Davenport et al., 2015; Quiros et al., in press). The AIDA array of ~ 200 closely-spaced, single-component seismographs recorded 12 days of the aftershock sequence.

The backprojection method is a simultaneous earthquake detection and location algorithm. Compared to single-seismogram detection algortihms, the primary advantage of using this method is its capability to improve the signal-to-noise ratio of the weak aftershocks by stacking of many seismograms, and consequently to detect events that can not be picked on individual seimograms. Therefore, the backprojection method has become a common approach for dense array datasets to produce earthquake catalogs. Its applications comprise a wide range of magnitude scales and interests including induced micoseismicity (e.g., Vlček et al., 2015), tectonic microseismicity (e.g., Hole et al., 2014, Ben Zion et al., 2015) and volcano seismicity (e.g., Langet et al., 2014) and induced seismicity associated with wastewater or CO_2 injection, stimulation in enhanced geothermal energy systems, and mining rock-burst

hazard studies.

Chapter 3 starts with an overview of the influence of the seismic array, noise, and velocity model in the scope of backprojection approach. The main objective of the chapter is to continuously and automatically back-project the entire dataset recorded by the dense AIDA array to fully take advantage of stacking to detect and locate the smallest possible events. Four previously-used, pre-processing backprojection approaches are considered. Their performances for detection and location are evaluated towards an efficient and robust strategy for automated backprojection process.

Chapter 4 presents the results of the 12-day aftershock catalog derived from the AIDA array and automated back-projection, including spatial-temporal patterns of seismicity, the earthquake statistics as well as a quantitative comparison with the catalog obtained from the co-deployed, unusually large temporal traditional network of 36 stations.

References

Ben-Zion, Y., Vernon, F. L., Ozakin, Y., Zigone, D., Ross, Z. E., Meng, H., & Barklage, M. (2015). Basic data features and results from a spatially dense seismic array on the San Jacinto fault zone. *Geophysical Journal International*, **202**, 1, 370–380.

Davenport, K. K., Hole, J. A., Quiros, D. A., Brown, L. D., Chapman, M. C., Han, L., & Mooney, W. D., 2015. Aftershock imaging using a dense seismometer array (AIDA) after the 2011 Mineral, Virginia earthquake, in The 2011 Mineral, Virginia, Earthquake and Its Significance for Seismic Hazards in Eastern North America, J.W. Horton Jr.,M. C. Chapman,

& R. A. Green (Editors). *Geological Society of America Special Papers*, **509**, 273–283.

Edwards, R. N., 1988. Two-dimensional modeling of a towed in-line electric dipole-dipole sea-floor electromagnetic system: The optimum time delay or frequency for target resolution. *Geophysics*, **53**, 6, 846–853.

Eidesmo, T., Ellingsrud, S., MacGregor, L. M., Constable, S., Sinha, M. C., Johansen, S. E., Kong, F.N., & Westerdahl, H., 2002. Sea bed logging (SBL), a new method for remote and direct identification of hydrocarbon filled layers in deepwater areas. *First break*, **20**, 3, 144–152.

Everett, M. E., & Edwards, R. N., 1993. Transient marine electromagnetics: The 2.5-D forward problem. *Geophysical Journal International*, **113**, 3, 545–561.

Everett M.E., & Weiss, C.J., 2002. Geological noise in near-surface electromagnetic induction data, *Geophysical Research Letters*, **29**, 1, 10-1–10-4.

Hole, J. A., Wang, K., Davenport, K. K., Chapman, M. C., Beskardes, G. D., Quiros, D. A., Brown, L. D., & Mooney, W. D., 2014. Back-Projection Imaging of Aftershocks Recorded by the Dense AIDA Array After the 2011 Virginia Earthquake. *Seismol. Res. Lett.*, **85**, 2, 434.

Ishii, M., Shearer, P. M., Houston, H. & Vidale, J. E., 2005. Extent, duration and speed of the 2004 SumatraAndaman earthquake imaged by the Hi-Net array, *Nature*, **435**, 7044, 933–936.

King, C. P. G. , Stein, R. S., & Lin, J, 1994. Static Stress Changes and the triggering of

earthquakes. *Bull. Seismol. Soc. Am.*, **84**, 935–953.

Langet, N., Maggi, A., Michelini, A., & Brenguier, F., 2014. Continuous Kurtosisbased migration for seismic event detection and location, with application to Piton de la Fournaise Volcano, La Runion, *Bulletin of the Seismological Society of America*, **104**, 1, 229–246.

Mandelbrot, B. B. & Van Ness, J. W., 1968. Fractional brownian motions, fractional noises and applications, *SIAM review*, **10**, 4, 422–437.

McMechan, G. A., Luetgert, J. H., & Mooney, W. D., 1985, Imaging of earthquake sources in Long Valley Caldera, California, 1983. *Bulletin of the Seismological Society of America*, **75**, 4, 1005–1020.

McMechan, George A., 1982. Determination of source parameters by wavefield extrapolation, *Geophysical Journal International*, **71**, 3, 613–628.

Meju, M. A., 2002. Geoelectromagnetic exploration for natural resources: models, case studies and challenges. *Surveys in Geophysics*, *23*, 2-3, 133–206.

Meju, M. A., Denton, P., & Fenning, P., 2002. Surface NMR sounding and inversion to detect groundwater in key aquifers in England: comparisons with VESTEM methods. *Journal of Applied Geophysics*, *50*, 1, 95–111.

Quiros, D. A., Brown, L. D., Davenport, K. K., Hole, J. A., Cabolova, A., Chen, C., Han, L., Chapman, M. C., Mooney, W. (in press). Reflection imaging with earthquake sources and dense arrays. *Journal of Geophysical Research (Solid Earth).* doi:10.1002/2016JB013677

Tezkan, B. 1999. A review of environmental applications of quasi-stationary electromagnetic techniques. *Surveys in Geophysics*, **20**, 3, 279–308.

Vlček, J., Fischer, T., & Vilhelm, J., 2015. Backprojection stacking of Pand Swaves to determine location and focal mechanism of microseismic events recorded by a surface array. *Geophysical Prospecting*, **64**, 6, 1428–1440.

Wilt, M., & Alumbaugh, D., 1998. Electromagnetic methods for development and production: State of the art. *The Leading Edge*, **17**, 4, 487–487.

Chapter 2

Estimating the power law distribution of Earth electrical conductivity from low-frequency, controlled-source electromagnetic responses

†**Citation:** Beskardes, G.D., Weiss C.J. and Everett M.E., (2017). Estimating the power-law distributions of Earth electrical conductivity from low-frequency, controlled source electromagnetic data, *Geophysical Journal International*, 208, no. 2, pp. 639–651.

Abstract

Electromagnetic responses reflect the interaction between applied electromagnetic fields and heterogeneous geoelectrical structures. Quantifying the relationship between multiscale electrical properties and the observed electromagnetic response is therefore important for meaningful geologic interpretation. We present here examples of near-surface electromagnetic responses whose spatial fluctuations appear on all length scales, are repeatable and fractally distributed, supporting the notion of a "rough geology" exhibiting multi-scale hierarchical structure. Bounded by end member cases from homogenized isotropic and anisotropic media, we present numerical modeling results of the electromagnetic responses of textured and spatially-correlated, stochastic geologic media, demonstrating that the electromagnetic response is a power law distribution, rather than a smooth response polluted with random, incoherent noise as commonly assumed. Our modeling results show that these electromagnetic responses due to spatially-correlated geologic textures are examples of fractional Brownian motion. Furthermore, our results suggest that the fractal behavior of the electromagnetic responses is correlated with degree of the spatial correlation, the contrasts in ground conductivity, and the preferred orientation of small-scale heterogeneity. In addition, the EM responses acquired across a fault zone comprising different lithological units and varying wavelengths of geologic heterogeneity also support our inferences from numerical modeling.

2.1 Introduction

Electromagnetic (EM) methods of geophysical exploration are diagnostic of the spatial and, sometimes, the temporal variability in ground electrical conductivity, a macroscopic physical property that is a function of many parameters including lithology, pore-scale surface chemistry, fracture networks, and the presence and distribution of fluids. When an EM source is applied, the Earth's macroscopic response is a multi-scale integration of the effects of charges that build up at conductivity gradients and contrasts, and currents that follow specific pathways in accordance with the bulk electrical properties of the medium. Most geophysicists agree that the underlying geology is inherently rough, containing multi-scale structure (e.g., Weiss and Everett, 2007; Barton and Zoback, 1992; Pilkington and Todoeschuck, 1993; Bailey and Smith, 2005; Aharonov and Rothman, 1996; Radlinski et al., 1999; Schlager, 2004; Acocella and Neri, 2005; and Purkis et al., 2005); with some but not all of them embracing a fractal viewpoint. While low-frequency EM induction in an idealized piecewise smooth Earth is well described as a diffusion process by the familiar Maxwell equations, in the case of a rough geological medium containing long-range-dependent heterogeneity, the relationship between multi-scale electrical properties and the EM responses has not yet been fully clarified. Fine-scale heterogeneities too small to be individually modeled have been treated as random and uncorrelated (white) noise in most analyses, i.e. the same as random instrumental or environmental effects. In contrast, based on previous observational controlled-source EM (CSEM) studies, subsurface geology comprising a self-similar distribution of electrical conductivity produces correlated, reproducible fluctuations of CSEM responses which are examples of fractional Brownian motion (fBm), a class of non-stationary signals (Everett

and Weiss, 2002). Multi-scale hierarchical geoelectrical structure is ubiquitous and its effects on CSEM responses cannot be properly modeled with traditional approaches based on coarse, piecewise smooth representations of Earth structure. This oversimplification has long contributed to a lack of understanding and, ultimately, has limited acceptance of the CSEM method as a viable and robust tool in exploration, solid Earth, environmental and other disciplines of geophysics. Herein we discuss methods that can directly introduce multi-scale heterogeneities into CSEM forward modeling. Our results provide an improved understanding of observed CSEM responses which should lead to a greater embrace of the method across a broad spectrum of geophysicists.

In geosciences, fractal concepts have been widely used in seismicity and volcanology as well as geomorphological and hydrogeological studies (Turcotte, 2007). Moreover, studies which refer to the fractal properties of multi-scale heterogeneity have recently been introduced in the geophysical literature. Nyquist and Boufadel (2008) developed scale-dependent models for characterizing the background geologic noise referring to small-scale heterogeneities in magnetic prospecting data, and White et al. (2002) analyzed the statistical properties of small-scale scatterers in magnetotelluric (MT) data. For the CSEM method, Everett and Weiss (2002) showed that observed CSEM responses can be represented as fractal signals due to the inherent and ubiquitous roughness of geology and placed an emphasis on the need for multi-scale analysis to develop rough geology models that would permit easier recognization of its CSEM signature. Benavides and Everett (2005) reaffirmed the aforementioned finding that spatial fluctuations due to rough geology spanning multiple length scales on CSEM responses are coherent and exhibit a fBm behavior; moreover, they showed some promising results based on wavelet transforms and variograms regarding man-made target detection

and localization. While their work attempts to separate target EM responses from rough fBm signal caused by geologic background, Ge et al. (2012, 2015) incorporates the roughness of geological medium directly into EM fractional diffusion modeling as a model parameter to assess the EM responses due to subsurfaces with multi-scale fractures. Recently, Weymer (2016) used the CSEM method to characterize large-scale framework geology controls on barrier island morphology. His statistical analyses for evaluating short- and long-range correlations (multivariate analysis and ARIMA) demonstrated that CSEM responses are governed by long-range dependence effects. Even though the studies mentioned herein are encouraging, discriminating the signatures of small-scale heterogeneities overlain by the responses due to resolvable large scale heterogeneities is still challenging, owing to unclear linkage between the statistical properties of multi-scale heterogeneity and their correspondence to measurable physical parameters.

Realistic subsurface geometries can be represented as the superposition of geologic rock types spanning multiple length scales. For example; spatial-correlated textures are evident in sedimentary rocks due to different depositional histories or the development of complex fracture networks (Korvin, 1992), or can be seen in metamorphic rocks formed at elevated temperatures and/or high pressure due to lineations, foliations, etc. Across all scales, the corresponding electrical conductivities of the spatial-correlated geologic textures in rocks should generate long-range-dependent, or fractal-like EM responses. This is not surprising in view of the fact that a fractal signal is simply a realization resulting from a fractional filter applied to a linear time-variant excitation (Li, 2009). To demonstrate the applicability of this concept in electromagnetic geophysics, Everett and Weiss (2002) collected CSEM responses across a floodplain and a fractured sandstone aquifer that are both strongly heterogeneous

at every scale from the smallest ($\sim 1\ m$, intercoil spacing) to the largest ($\sim 100\ m$, length of survey profile) scales probed. The floodplain responses were acquired using an azimuthal geometry with the transmitter loop fixed at the center of a circle, and with the receiver coil moving to different stations along the circumference; whereas the sandstone aquifer responses were acquired along a linear survey profile while keeping a fixed transmitter-receiver offset. The authors examined the power spectral density (PSD) functions of the CSEM responses and their spatial increments, and showed that they exhibited power-law distributions in the wavenumber domain. The PSD's power-law relation indicates a fractal property that is different from uncorrelated and random noise (Everett and Weiss, 2002). The responses are examples of fBm, a class of non-stationary signals that describe self-similar processes with long-range correlations (Mandelbrot and van Ness, 1968).

In this paper, we mainly focus on developing a better understanding of the relationship between the roughness of EM responses and the roughness of the causative subsurface variations in ground conductivity. We examine herein, using numerical modeling, the appearance in CSEM responses of multi-scale heterogeneities produced by spatially-correlated rock textures. Lineations and foliations in rock are modeled as multi-scale geologic textures. A line integral convolution algorithm is used to generate synthetic, textured 3D ground conductivity models representing spatially-correlated distributions. The CSEM responses for these synthetic conductivity models are calculated using a 3D finite difference algorithm (Weiss, 2013) and the appearance of multi-scale heterogeneities in the resulting CSEM responses is examined via PSD analysis. Our results show that the PSDs of synthetic CSEM responses over both the lineated and the foliated models present a power-law relation, indicating a fBm nature. Furthermore, our numerical models suggest that the fractal parameters of the CSEM

responses are controlled by the degree of the spatial correlation, the contrast in ground conductivity, and the direction of fine-scale heterogeneities. In addition, we present herein a real data example from a fault zone that is a good representative of multi-scale hierarchical structure. The PSDs of the observed EM data also exhibit fractal behavior and support our inferences from numerical modeling. The results of this paper suggest a viable physical mechanism for explaining observed CSEM responses across a variety of natural geological settings.

2.2 Geologic Model Construction - Line Integral Convolution (LIC)

One method for generating electrical conductivity models with complex 3D lineation textures is the line integral convolution (LIC) method (Cabral and Leedom, 1993, Shen and Kao, 1998). Its ostensible purpose is to visualize vector fields. The algorithm is a convolution of a vector field with a 3D white-noise scalar field, the resulting volume being an image of the defined vector field. Here we apply this visualization technique to construct a textured scalar field. Folded sedimentary beddings (Hobbs and Ord, 2014), metamorphic fabrics (such as lineation, foliation, cleavage etc.), or power-law distributed fracture networks (Fagereng, 2011) can be generated by LIC by selecting an appropriate underlying vector field.

In the LIC algorithm, the nodes of a regular grid are initially populated (Fig. 2.1a) with random numbers on the interval (0,1). With a vector field whose streamlines represent the direction and tortuosity of the geologic texture to be modeled, the initial grid is convolved (Figs 2.1b and 2.c) along segments of these streamlines, where the length of the convolution

segment N reflects the spatial extent of correlation (Fig. 2.1d) in the lineation direction. Large convolution length produces smoother lineation texture, and increased amount of spatial correlation.

For definiteness, we focus herein on lineations in metamorphic rock as generators of fine-scale geological heterogeneity, but our methods apply equally to sedimentary bedding, fracture networks and other generators of geological texture. To explore ground conductivity models possessing spatially-correlated metamorphic fabric, we vary the direction and the correlation length of small-scale heterogeneity. To investigate the effect of the direction of the small-scale heterogeneity, we generate unidirectional as well as azimuthal (circular) lineated models by the LIC algorithm (with correlation length $N = 10$, Fig. 2.2). The unidirectional lineations are fully uncorrelated in the other directions except the lineation direction. We also construct the same lineated models but with a higher spatial correlation length ($N = 40$) to better understand its effect on the resulting CSEM responses. As an initial input to the LIC algorithm, a random (white noise) field ($N = 1$) is populated with a conductivity range of $[0.1\ S/m,\ 1\ S/m]$. Additionally, traditional foliated conductivity models are built as a sequence of parallel sheets of random thickness and conductivity, without using the LIC algorithm (Fig. 2.2d). The chosen conductivity range may correspond to graphitic schist, clay, alluvium with highly conductive fluids (salt water, water contaminated by inorganic solvents, etc.), magnetite (neglecting its magnetic properties, i.e. $\mu \neq \mu_0$), etc. Further, representative conductivities of rocks that show fractal properties, such as self-similar fractures, lineations or foliations, etc. vary in the range of about $0.00001\ S/m$ to $0.1\ S/m$.

2.3 CSEM Responses

The computation of CSEM responses of the textured 3D conductivity models is performed using a recently-developed, broad-band finite difference algorithm for discretization and solution of the Maxwell equations that accommodates the full physics of field propagation by including the effects of heterogeneity in electrical conductivity, polarization, relaxation and chargeability subject to arbitrary grounded, or inductively-coupled, compact and plane wave sources (Weiss, 2013). The method works by discretizing the model domain into a rectilinear Cartesian mesh, on whose edges and nodes reside the mimetic staggered "Yee" grid components of the Lorenz-gauged magnetic vector potential and electric scalar potential, respectively (Yee, 1966). The coupled system of potentials, which constitute the solution to a sparse system of linear equations, is found iteratively using a matrix-free implementation of the Quasi-Minimal-Residual (QMR) method for complex symmetric coefficient matrices (Freund and Nachtigal, 1991). The matrix-free aspect yields a reduction in memory storage requirements from $64M^3$ to $24M^3$ on an $M \times M \times M$ node mesh with no negative impact on computation throughput (Weiss, 2001).

The CSEM responses are herein simulated to model an EM-34 survey (McNeill, 1980); however, EM-34 specificity is not required and any CSEM system can be selected for modeling. The EM-34 utilizes two coils. One coil operates as a transmitter (TX) and the other one operates as a receiver (RX). An alternating electrical current at a specified frequency passes through the transmitter coil, creating an alternating magnetic field ("primary field") of the same frequency. Because of its time-dependence, the primary field induces current to flow in the subsurface at depth according to its electrical conductivity. The induced current gen-

erates a weaker magnetic field ("secondary field") which is inferred from measurements at the receiver coil. Over a uniform halfspace and at low frequencies, i.e. for intercoil spacings much less than the skin depth such that the low-induction number approximation holds (McNeill, 1980), the ratio of the quadrature secondary to the (real) primary magnetic field is directly proportional to the ground conductivity. Hence, for a fixed primary field intensity at the receiver coil, variations in quadrature (Im) magnetic field are a direct proxy measure for reported values of apparent conductivity from low-induction-number survey/profiling instruments (McNeill, 1980).

In our simulations, the EM-34 transmitter in "vertical dipole" mode is approximated by a square current loop of 0.75-m lying directly on the air-earth interface at the origin of the computational grid. The loop is excited with an alternating current of amplitude 1.0 A at frequency 1600 Hz. Instead of circular coil that is utilized by EM-34 ground conductivity meter in real applications, we here consider a square current loop that is computationally easier to define due to its filaments coincident with the edge of the primal finite volume mesh, knowing that the resulting vertical magnetic dipole does not depend strongly on the shape of current loop and each current loop can be simply expressed in forms of an integration of vertical magnetic dipoles over the area of itself. Here, it should be noted that it is feasible to compare the simulated EM fields as a result of a square loop excitation to observed EM-34 data (the EM-34 benchmark example; Weiss, 2013).

The conductivity model is discretized using a 400×400×50 interior uniform mesh with cell-size $0.75 \times 0.75 \times 3$ m, within the limits of $[-150\ m, 150\ m]$, $[-150\ m, 150\ m]$ and $[0\ m, -150\ m]$ in the x,y and z directions, respectively. The EM-34 survey profile is designed using a

circular RX path with fixed TX at the center. This is done to avoid any effect of the direction of the survey profile relative to the lineation direction. For each model, both the ground conductivity (σ_{true}) and the resulting CSEM responses (herein reported in the form of apparent ground conductivity, σ_{true}) are sampled at the cell-size of the calculation mesh along the circular paths for 10, 40 and 80 m intercoil spacings.

Before going further with the analysis, we tested whether there is an equivalent classical halfspace which produces the same CSEM response as the lineated heterogeneity constructed by LIC. We manually searched for the equivalent homogeneous medium whose EM response best fits the response of the unidirectional lineated model (N = 5, Fig. 2.3). Even though we repeated the process for a different lineated model with a longer correlation length (N = 40), in both cases, either the near-offset response fits, or the far-offset response fits, but not both. This result indicates that there is no equivalent halfspace representation for the LIC lineated models tested. Moreover, the responses of the lineated models qualitatively resemble an intermediate response in comparison with the end-member responses of the two homogeneous models that bound the conductivity range of the lineations (Fig. 2.4). This is because while a homogeneous medium does not possess a broad spectrum of scale variation of heterogeneities, the LIC models comprise spatial correlations spanning multiple length scales that result in averaging at different length scales by the diffusion process.

2.4 Results

As a more quantitative approach, we examine CSEM responses of models containing spatially-correlated, small-scale heterogeneity using a power spectral density (PSD) analysis. In the

spatial domain, the PSD shows the power of a signal as a function of wavenumber. We use a 1D Fast Fourier Transform (FFT) to decompose both the CSEM responses and the ground conductivities, sampled along the survey profile, into their wavenumber components. We find that the PSDs both present a power-law behavior, i.e. they are linear on a log-log plot. A power-law relation can be expressed in the form $|A(k)|^2 \propto k^\beta$ where A is the amplitude of the decomposed signal at the given wavenumber k and β is the spectral index or exponent (Eke et al., 2000). The β exponent describes the heterogeneity of the signal and is a measure of "roughness". Fractal signals with $|\beta| < 1$ are defined as fGn; they have constant variance at all sample points, which classifies them as stationary signals. The PSDs of the ground conductivity profiles suggest that LIC-constructed models are examples of fGn; i.e. not fractal (self-similar) but nevertheless representative of spatially-correlated, small-scale heterogeneity (Fig. 2.5). On the other hand, the PSDs of the CSEM responses reveal that they are non-Gaussian fractal signals. The lack of stationarity associated with fBm is characterized by the condition of $1 < |\beta| < 3$ (Eke et al.,2000). An fBm signal can be recognized by its stationary (fGn) increments with no significant long-range dependence. The mean of the CSEM responses is irregular and fluctuates along a profile (Fig. 2.5), while the mean value of the increments is stationary with zero mean (Fig. 2.6) over an entire profile; thereby indicating that the CSEM responses are fBm. It should also be noted that the spatial correlations of geologic fabric result in strong cyclic behavior of the CSEM responses, which is not surprising given that the governing (frequency domain) Maxwell second-order differential equations connecting the ground electrical conductivity to the EM response operate as a smoothing filter. This idea is best captured by the statement well-known to geophysicists: The Earth acts as a low-pass filter. Further, the PSDs bring out an important point that

not necessarily self-similar Earth models, but rather a wider class of spatially-correlated multi-scale heterogeneity, may produce fractal-like EM responses.

In the following section, we delve further into the fBm behavior of CSEM responses due to spatially-correlated, small-scale heterogeneity by examining the β (roughness) values in more detail.

2.5 Analysis

Herein, we present a graphical summary of the roughness (β values) of both the CSEM responses and their causative ground conductivities (Fig. 2.7). We obtain the β value from the slope of the best-fit line on the PSD log-log plot. This has been done for both the CSEM and the ground conductivity profiles belonging to simulated EM34 experiments for offsets in the range $10 - 80\ m$. The $|\beta| < 1$ values of the ground conductivity PSDs signify that the conductivity models are not fully fractal exhibiting long-range dependence, but represent spatially-correlated fGn (Fig. 2.7). On the other hand, the $|\beta| > 1$ values for the CSEM PDSs indicate that power is concentrated at smaller wavenumbers rather than spread across the entire spectrum, as it would be in the case of random (white) noise. This result implies that, in the presence of spatially-correlated, multi-scale heterogeneity, the random noise assumption as commonly used for the fluctuations of CSEM responses is not valid.

For unidirectionally-lineated models (such as $N = 10, 40$), where lineation is not along the circular survey profile, our results suggest that lineated models with different correlation lengths i.e., 7.5 and 30 m, have similar roughness values. This implies that correlation length

does not significantly affect the degree of the roughness of the CSEM responses for cross-lineation profiles. However, for the circular-lineated models, where the direction of lineation is along the profile, our results indicate that the roughness of the CSEM fluctuations are distinguishably different in accordance with the correlation length of lineations (N = 10 vs. N = 40): the longer correlation length of the lineation results in smoother CSEM responses. Based on the comparison of unidirectional and circular-lineated models, it can be inferred that the direction of the lineation plays an important role in determining the fractal behavior of a CSEM response. For foliated models which have the same directivity but have much more dramatic and sharp contrasts in small-scale heterogeneity, in comparison with unidirectional lineated models, it is evident that the resulting CSEM responses are considerably more rough and their β values are beyond the fractal limit ($3 < |\beta|$). This indication suggests that not only the correlation length but also the contrast in ground conductivity of small-scale heterogeneity may contribute to the degree of the roughness of the CSEM responses.

Overall, our results show that the degree of the spatial correlation, the direction of lineation, and the contrast in ground conductivity of the small-scale heterogeneity directly affect the fractal signature of the CSEM response. Particularly, the correlation length has more control on the roughness for along-lineation profiles while the contrast in ground conductivity becomes more important for cross-lineation profiles.

2.6 EM Survey Near Mason, Texas

The field site is located on the Edwards Plateau of central Texas, specifically, at the western margin of the Llano Uplift, a $\sim 9000\ km^2$ geologic dome comprised of exposed Precambrian

granite, gneiss and schist formations. The Precambrian history of the uplift is described by Levine and Mosher (2010). It is widely believed to have originated with the Mesoproterozoic Grenvillian collision $1.15 - 1.2\ Ga$ between Laurentia and a southern continent, possibly the Kalahari craton, during assembly of supercontinent Rodinia (Dalziel et al., 2000; Reese et al., 2000). The syntectonic and post-tectonic intrusion of granites into the folded metamorphic terrain is thought to have been initiated by the eventual breakoff of the subducting Laurentian slab (Mosher et al., 2008) at $1.12 - 1.07\ Ga$.

The sandstones overlying the Precambrian formations at the field site were deposited at $\sim 530\ Ma$ during the early part of the widespread Cambrian-Ordovician marine transgression. According to a first hypothesis, the sandstones were later fractured and faulted in a predominantly NE-SW alignment due to lithospheric plate flexure, likely during the Pennsylvanian (Becker, 1985) as a direct consequence of the Ouachita orogeny. According to a second hypothesis (Amsbury and Haenggi, 1993), the steeply dipping Pennsylvanian-age faults are predominantly strike-slip and caused by brief episodes of north-south compression that sliced the central Texas craton into blocks.

The field site is located within the Mason Mountain Wildlife Management Area (MMWMA) $\sim 12\ km$ north of the town of Mason, Texas. Electromagnetic loop-loop data at $0.25\ m$ station spacing and $8\ kHz$ frequency were acquired using the GSSI EM-Profiler (GSSI, 2016) along two profiles (Fig. 2.8) that cross a NE-SW steeply dipping normal fault, comprising a half-graben, that has been previously mapped by Helper (2006). The footwall to the northwest is composed of Precambrian age Town Mountain granite (Fig. 2.9a) while the hanging wall to the southeast is composed of Cambrian age Hickory sandstone. The footwall and the fault

zone also contains abundant Precambrian marble (Fig. 2.9b), an important component of the Packsaddle Schist formation.

The Hickory Sandstone is comprised of fluvial, marine and shoreline transgressive strata (Randolph, 1991) and is organized into upper, middle and lower units. The lower Hickory quartz sandstone unit is light brown, medium to coarse-grained, poorly-sorted, and friable to weakly-cemented. The middle Hickory sandstone is, on average, finer-grained, better-sorted, and more thinly-bedded with common laterally extensive siltstone and shale interbeds. The upper Hickory quartz sandstone is red to maroon, coarse-grained, well-rounded, moderately well-sorted, with abundant iron-oxide ooids and cement.

The first EM data profile $A-A'$ runs north-south for $\sim 340\ m$ and, from the trail intersection, bends first to the southwest and then to the west for the final $\sim 295\ m$. The second profile $B-B'$ runs east-west for $\sim 220\ m$. The surface trace of the fault zone is shown by the dotted lines and crosses both profiles at approximately 45°. The fault zone where it crosses profile $A-A'$ at $\sim 100\ m$ north of the trail intersection is well-defined by surface exposures of marble and is $\sim 20\ m$ wide. The fault zone appears to be wider, $\sim 80\ m$, but is less well-defined where it crosses profile $B-B'$ at $\sim 65\ m$ west of the trail intersection. The sandstone portions of profiles $A-A'$ and $B-B'$ contain the lighter-colored lower and middle units (Fig. 2.9c) with the exception of a minor outcrop of the maroon-colored upper unit $10-20\ m$ to the north of the trail intersection and, in the southwest-trending portion of profile $A-A'$, a more extensive $\sim 130\ m$-wide zone of weathered maroon soil (Fig. 2.9d) likely sourced from the upper unit.

To examine our previous inferences from the modeling results, we consider the Mason EM

dataset for PSD analysis. The PSD β values of both apparent ground conductivity profiles fall within the fBm limit with their stationary increments (Figs 2.10a and b). The β slopes of -2.530 and -2.261 do not present a significant difference regarding to directionally-varying geologic roughness for these perpendicular profiles. In addition, we also consider PSD β slopes of each lithologic zone along the perpendicular profiles for a relative and stochastic comparison of geologic heterogeneity of these units (Fig. 2.11). The β slopes along each profile vary around the slope value of entire profile implying that the survey length determines the relative contribution of short and long wavelengths to the spectrum (Figs 2.10c and d). Moreover, our PSD analysis show that not only the entire profiles but also each lithologic unit itself exhibits a fBm behavior reflecting a multi-scale heterogeneous nature. Especially, the fault zone (marble) on the Profile $B - B'$, where the zone gets wider, shows relatively higher β value comparingly with its neighbour lithologic units, referring to a higher degree of spatial correlation or self-similarity of the fractures within the fault zone as pointed out by our modeling results. Further, significantly higher β value of the granite zone on the Profile $A - A'$ comparingly with the granite zone on the Profile $B - B'$ suggests a directional variation in the geologic roughness of the granite unit; in other words, the granite may be more fractured/damaged towards northeast, perhaps as a result of a variation in the local stress field. However, this indication needs to be further investigated. Our spectral inspection on the observed EM dataset herein strengthens the notion that spectral exponent β value provides a direct inference regarding the geologic roughness and may be considered as a parameter to characterize stochastic geologic medium.

2.7 Discussion

Multi-scale heterogeneity is a result of the tremendous spatial and temporal variability of geological process which operate across multiple length scales from the mineral scale to the continental scale; it is brought about by almost all geological processes: sedimentary, igneous and metamorphic. The relationship between the causative multi-scale geoelectrical heterogeneity and the CSEM response has not been completely understood due to the limited observations and the insufficiency of traditional modeling approaches which oversimplify the Earth structure as an idealized piecewise smooth medium. Here, we incorporate spatially-correlated geologic heterogeneity directly into CSEM forward modeling by texturing the Earth's geoelectrical structure in the form of spatial correlations via the LIC algorithm. Our modeling results show that the spatially-correlated, small-scale heterogeneities produce power-law distributed, fractal-like EM responses like those that are observed in actual surveys. Further, our results indicate that properties of small-scale heterogeneities such as the preferred orientation, the correlation length, and the contrast in ground conductivity determine the fractal signature of CSEM responses, which may require geophysicists to re-visit conventional interpretations of near-surface EM data. In our analysis, the power spectrum of a CSEM response points out that the common random (white) noise assumption is not valid whereas fractal-based interpretations are more reliable and appropriate. Further development of mathematical models to account for the fractal-like fluctuations due to multi-scale heterogeneity within near surface CSEM responses should substantially improve the interpretation of EM survey data.

Characterizing the signature of small-scale heterogeneities is a critical step to interpret the

EM signatures of buried targets (Benavides and Everett, 2005). Based on our results, we suggest that a fractal analysis of EM observations might also be helpful to obtain information about the directivity and the correlation degree of metamorphic fabric which are direct controls on ore mineralisation and oil traps. Moreover, monitoring changes in the roughness of EM observations over a complex fracture network may provide some information (e.g. complementary to microseismic monitoring) regarding the extent and direction of progressive fractures. More observational studies will give a valuable opportunity to investigate the enigmatic relationship between geologic structure and spectral exponent (β value). Ultimately, a measurement of the spectral exponent may enable a direct inference about the roughness of the underlying geologic structure as demonstrated in the given real data example.

Herein, we present a method to generate EM responses with dependencies over short, medium and long-range scales, i.e. a fBm signal. The LIC algorithm provides multi-scale length dependence of the ground electrical conductivity by convolving random noise, which provides the short-range dependence, with a deterministic trend, which provides the long-range dependence. Furthermore, the forward-modeling step from the conductivity to the EM response, which operates as a smoothing spatial filter over the instrument footprint, provides a medium-range dependence. The resultant of these three processes generated fractal-like behavior exhibiting multi-scale dependence. The model-generating process can be adapted to generate realistic ground conductivity models that contain both rough background geology and buried man-made conductive targets to study the fractal statistics of CSEM responses to improve detection and buried target classification. This topic was earlier explored by Benavides and Everett (2005).

In this study, we focus mainly on horizontal spatial correlation of geologic textures and do not take account of vertical correlation. The latter would result in variations in signal penetration depth, which should have an effect on the apparent roughness of the resulting EM responses. By numerical modeling, an investigation of the effects of vertical spatial correlations of heterogeneity on the power-law distributions of the EM responses would enable a better understanding of the effective depth of the penetration in rough geological environments.

Finally, there is a great need for further experiments to support the theoretical concepts presented herein. Observational studies will substantially improve our understanding about the fractional Brownian motion nature of CSEM responses. Especially, a comprehensive 3-D dataset would provide a valuable opportunity to better clarify the linkage between geoelectric roughness and its electromagnetic response.

2.8 Conclusions

Our study shows that EM responses due to spatially-correlated, fine scale heterogeneities exhibit a fBm behavior agreeing with the findings of previous observations and they are much more diagnostic than a classical halfspace's response. Moreover, our modeling results suggest that fractal-like EM responses may result from not necessarily self-similar, but rather a wider class of spatially-correlated heterogeneities. Based on our PSD analyses, it is indicated that the fBm behavior is correlated with degree of the spatial correlation, the contrasts in ground conductivity, and the preferred orientation of multi-scale heterogeneity. In addition, the PSD analyses of both synthetic and real data demonstrate that higher β spectral exponent values

(1 <) correspond to higher degree of geological roughness presenting long-range dependency, and thus suggest that β value may be used as a property to characterize stochastic geologic medium. Finally, we highlight the need of more observational and modeling studies to confirm the aforementioned findings as well as to better understand the signatures of multi-scale spatially-correlated and self similar geologic features that appear on resolution-limited geophysical EM data, and to further investigate how we can reveal information from these signatures regarding the physical properties of rough underlying geology.

Acknowledgments

The authors would like to thank Mark Mitchell of MMWMA for his ongoing support of our field research efforts and Mike Heaney for help with interpreting the geologic structure. The authors are thankful to Emin Ulugergerli for beneficial comments during the manuscript preparation. The authors also would like to thank Ute Weckmann, Niclas Linde and an anonymous reviewer for their constructive and insightful comments that contributed greatly to enrich this manuscript. This work was supported by the United States National Science Foundation, Hydrologic Sciences Program under awards EAR-1519221 and EAR-0943598. Portions of this work were conducted at Sandia National Laboratories. Sandia National Laboratories is a multi-mission laboratory managed and operated by Sandia Corporation, a wholly owned subsidiary of Lockheed Martin Corporation, for the U.S. Department of Energy's National Nuclear Security Administration under contract DE-AC04-94AL85000.

References

Acocella, V., & Neri, M., 2005. Structural features of an active strike-slip fault on the sliding flank of Mt. Etna (Italy). *Journal of Structural Geology*, **27**, 343–355.

Aharonov, E., & Rothman, D. H., 1996. Growth of correlated pore-scale structures in sedimentary rocks: A dynamical model. *Journal of Geophysical Research*, **101**, 2973–2988.

Amsbury, D.L. & Haenggi, W. T. 1993. Middle Pennsylvanian strike-slip faulting in the Llano Uplift, central Texas. *Bull. Houston Geol. Soc.*, **35**, 20–23 and 56–58.

Bailey, R.J., & Smith, D.G., 2005. Quantitative evidence for the fractal nature of the stratigraphic record: results and implications. *Proceedings of the Geologists' Association*, **116**, 129–138.

Barton, C., & Zoback M., 1992. The self-similar distribution and properties of macroscopic fractures at depth in crystalline rock in the Cajon Passscientific drill hole. *Journal of Geophysical Research*, **97**, 5181–5200.

Becker, J.E. 1985. Structural analysis of the western Llano uplift with emphasis on the Mason fault. *M.S. Thesis*, Texas A & M University.

Benavides, A., & M. E. Everett, 2005. Target signal enhancement in near-surface controlled-source electromagnetic data. *Geophysics*, **70**, 3, G59–G67.

Cabral, B., & Leedom, L., 1993. Imaging vector fields using line integral convolution. *Computer Graphics* **27**, 4, 263–272.

Dalziel, I.W.D., Mosher, S. & Gahagan, L.M., 2000. Laurentia-Kalahari collision and the assembly of Rodinia. *The Journal of Geology*, **108**, 499–513.

Eke A., Herman, P., Bassingthwaighte, J.B., Raymond, G., Percival, D., Cannon, M., Balla, I., & Ikrényi, C., 2000. Physiological time series: distinguishing fractal noises from motions. *Pflügers Archiv*, **439**, 4, 403–415.

Everett M.E., & Weiss, C.J., 2002. Geological noise in near-surface electromagnetic induction data. *Geophysical Research Letters*, **29**, 2001 GL 014049.

Fagereng A., 2011. Fractal vein distributions within a fault-fracture mesh in an exhumed accretionary mélange, Chrystalls Beach Complex, New Zealand. *Journal of Structural Geology*, **33**, 918–927.

Freund R.W., & Nachtigal, M.N., 1991. QMR - A quasi-minimal-residual method for non-Hermitian linear systems. *Numerische Mathematik*, **60**, 315–339.

Ge, J., Everett, M.E., & Weiss, C.J. 2012. Fractional diffusion analysis of the electromagnetic field in fractured media Part I: 2D approach. *Geophysics*, **77**, 4, WB213–WB218.

Ge, J., Everett, M.E., & Weiss, C.J. 2015. Fractional diffusion analysis of the electromagnetic field in fractured media–Part 2: 3D approach. *Geophysics*, **80**, 3, E175–E185.

GSSI 2016, http://www.geophysical.com/profiler.htm, accessed Oct. 18, 2016.

Helper, M. 2006. Geological map of the Mason Mountain W.M.A., Mason Co., TX, www.geo.utexas.edu/courses/420k/Trips/trip5/`MasonMt_GAT_geo_final_april`.pdf, accessed

Oct. 18 2016.

Hobbs B.E., & Ord A., 2014. *Structural Geology: The Mechanics of Deforming Metamorphic Rocks*, Elsevier, 30–34.

Korvin G., 1992. *Fractal Models in the Earth Sciences*, Elsevier, Amsterdam.

Levine, J.S.F. & Mosher, S. 2010. Contrasting Grenville-aged tectonic histories across the Llano Uplift, Texas: new evidence for deep-seated high-temperature deformation in the western uplift. *Lithosphere*, **2**, 399–410.

Mandelbrot, B. B. & Van Ness, J. W., 1968. Fractional brownian motions, fractional noises and applications. *SIAM review*, **10**, 4, 422–437.

McNeill, J. D., 1980. Electromagnetic terrain conductivity measurement at low induction numbers. Geonics Ltd. Technical Note TN-6.

Mosher, S., Levine, J. & Carlson, W., 2008. Mesoproterozoic plate tectonics: A collisional model for the Grenville-aged orogenic belt in the Llano uplift, central Texas. *Geology*, **36**, 55–58.

Li, M., 2009. Fractal time seriesa tutorial review. *Mathematical Problems in Engineering*, 2010.

Nyquist J.E., & Boufadel M., 2008. Multifractal Characterization of Geologic Noise for Improved UXO Detection and Discrimination. Final Report, SERDP Project MM-1508.

Pilkington, M., & Todoeschuck, J. P., 1993. Fractal magnetization of continental crust. *Geophysical Research Letters*, **20**, 627–630.

Purkis, S. J., Reigl, B. M., & Andrefouet, S., 2005. Remote sensing of geomorphology and facies patterns on a modern carbonate ramp (Arabian Gulf, Dubai, UAE). *Journal of Sedimentary Research*, **75**, 861–876.

Radlinski, A. P., Radlinska, E. Z., Agamalian, M., & Wignall, G. D., 1999. Fractal geometry of rocks. *Physical Review Letters*, **82**, 3078–3081.

Randolph, L.C. 1991. The effects of faults on the groundwater system in the Hickory sandstone aquifer in central Texas. *M.S. Thesis*, Texas A & M University.

Reese, J.F., Mosher, S., Connelly, J., & Roback, R., 2000. Mesoproterozoic chronostratigraphy of the southeastern Llano uplift, central Texas. *Geological Society of America Bulletin*, **112**, 278–291.

Schlager, W., 2004. Fractal nature of stratigraphic sequences. *Geology*, **32**, 185–188.

Shen H. W., & Kao, D. L., 1998. A new line-integral convolution algorithm for visualizing time-varying flow fields. *Computers & Geoscicenes*, **4**, 98–108.

Turcotte D.L., 1997. *Fractals and Chaos in Geology and Geophysics*, 2nd edn. Cambridge University Press, Cambridge.

Weiss, C. J., 2001. A matrix-free approach to solving the fully 3D electromagnetic induction problem. 71st Annual International Meeting, SEG, Expanded Abstracts.

Weiss CJ and Everett M.E., 2007. Anomalous diffusion of electromagnetic eddy currents in geological formations. *Journal of Geophysical Research*, **112**, B08102.

Weiss C.J., 2013. Project APhiD: A Lorenz-gauged A-Phi decomposition for parallelized computation of ultra-broadband electromagnetic induction in a fully heterogeneous Earth. *Computers & Geosciences*, **58**, 40–52.

Weymer B.A., 2016. An investigation of the role of the framework geology on modern barrier island transgression. *PhD thesis*, Texas A & M University.

White, B.S., Kohler, W., & Srnka L. J., 2002. Random Scattering and the Detection Capability of the Magnetotelluric Method, *IUTAM Symposium on Mechanical and Electromagnetic Waves in Structured Media Solid Mechanics and Its Applications*. **91**, 31–42.

Yee, K., 1966. Numerical solution of initial boundary value problems involving Maxwell's equations in isotropic media. *IEEE Transactions on Antennas and Propagation*, **14**, 302–307.

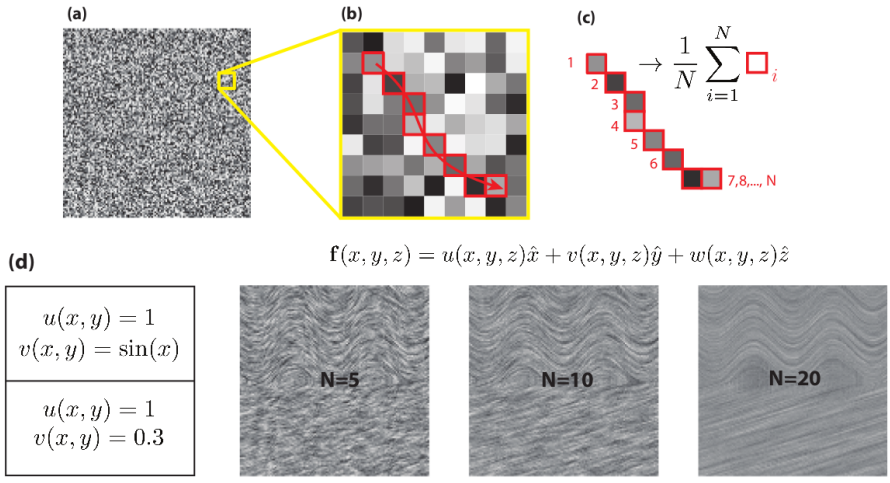

Figure 2.1: (a) White noise populated with interval $(0, 1)$, (b) streamline along segments, (c) LIC along the streamline path, (d) LIC models with $N = 5$, $N = 10$ and $N = 20$ degree of correlation.

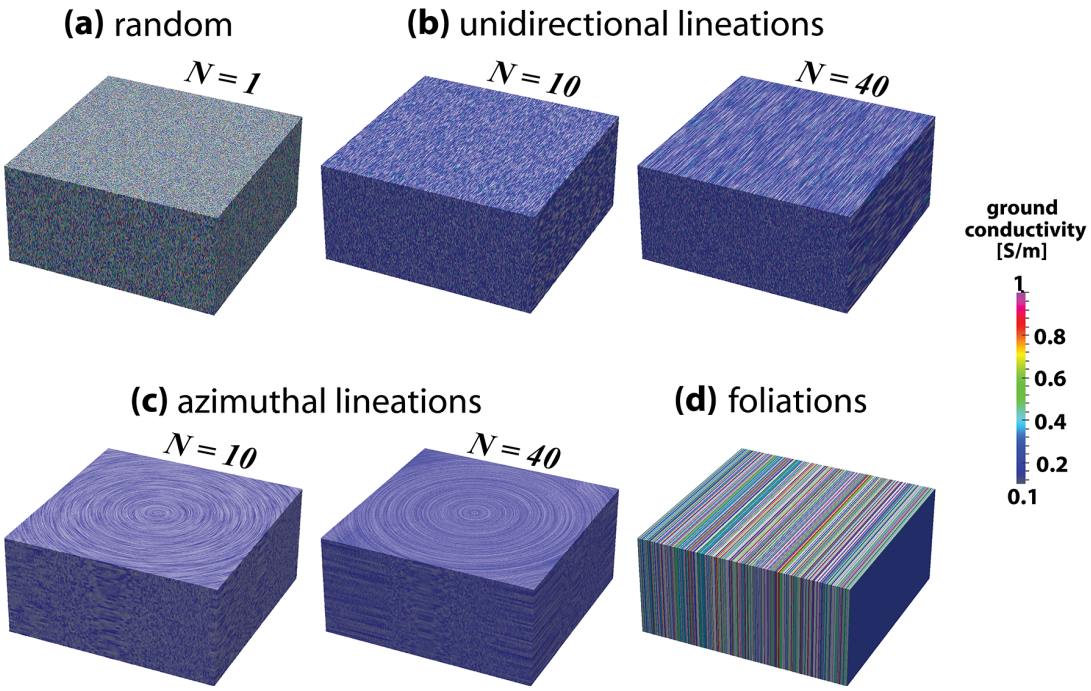

Figure 2.2: (a) Random populated model, (b) unidirectional lineated LIC models with N = 10 and N = 40 degree of spatial correlation, (c) azimuthal (circular) lineated LIC models with N = 10 and N = 40 degree of spatial correlation, (d) foliated/sheeted model.

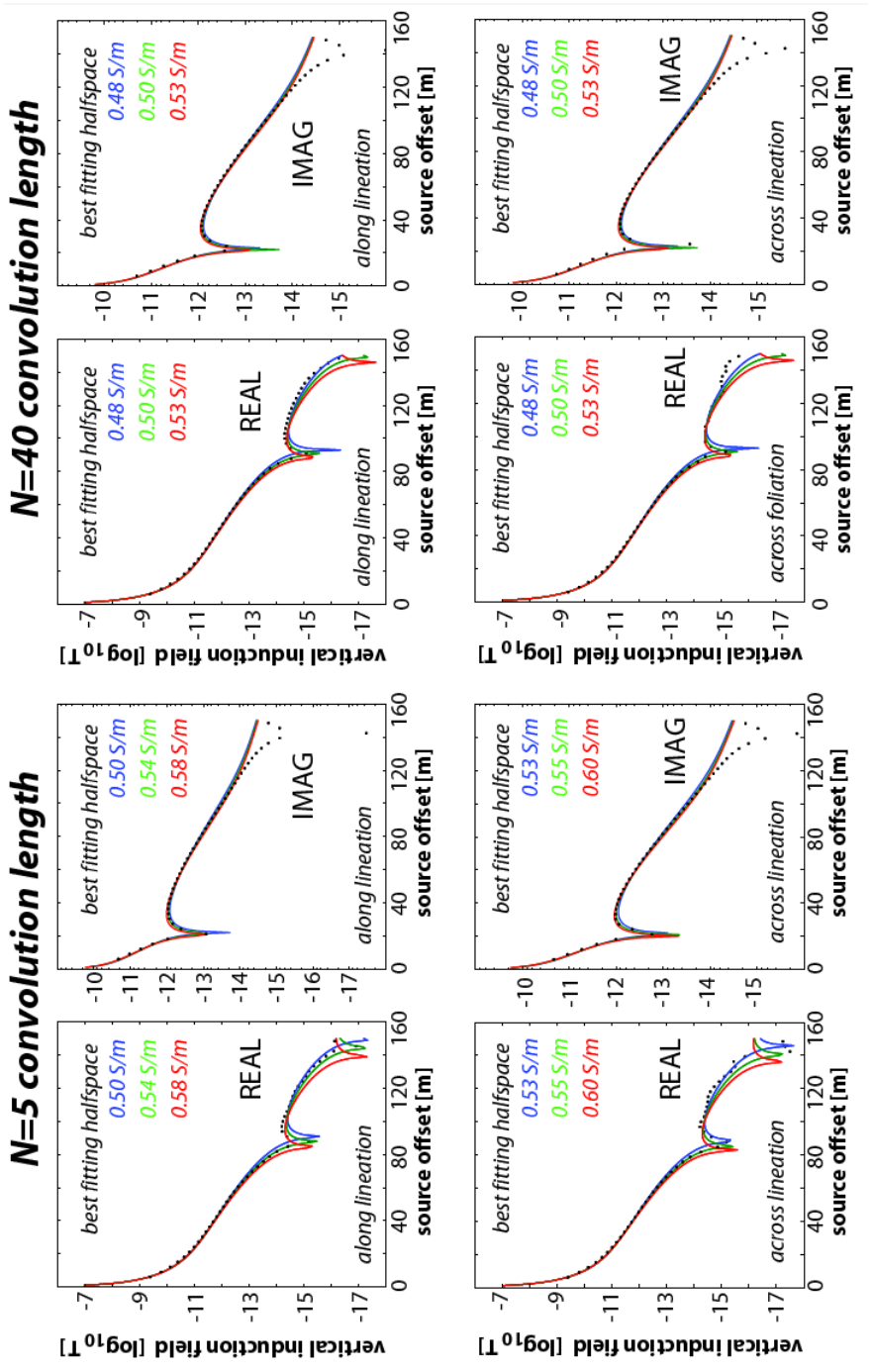

Figure 2.3: Finite difference solutions of the unidirectional lineated models with N = 5 and 40 degree of correlation which are textured in the conductivity range of 0.1-1 S/m (shown as black dots). Both across and along lineation profiles are given. The best-fit lines to the solutions of the lineated models are shown in colored solid lines. For both lineation directions and both components of the induction fields, either the near offset fits, or the far offset fits, but not both; indicating that there is no equivalent homogeneous media representation for the LIC lineated models.

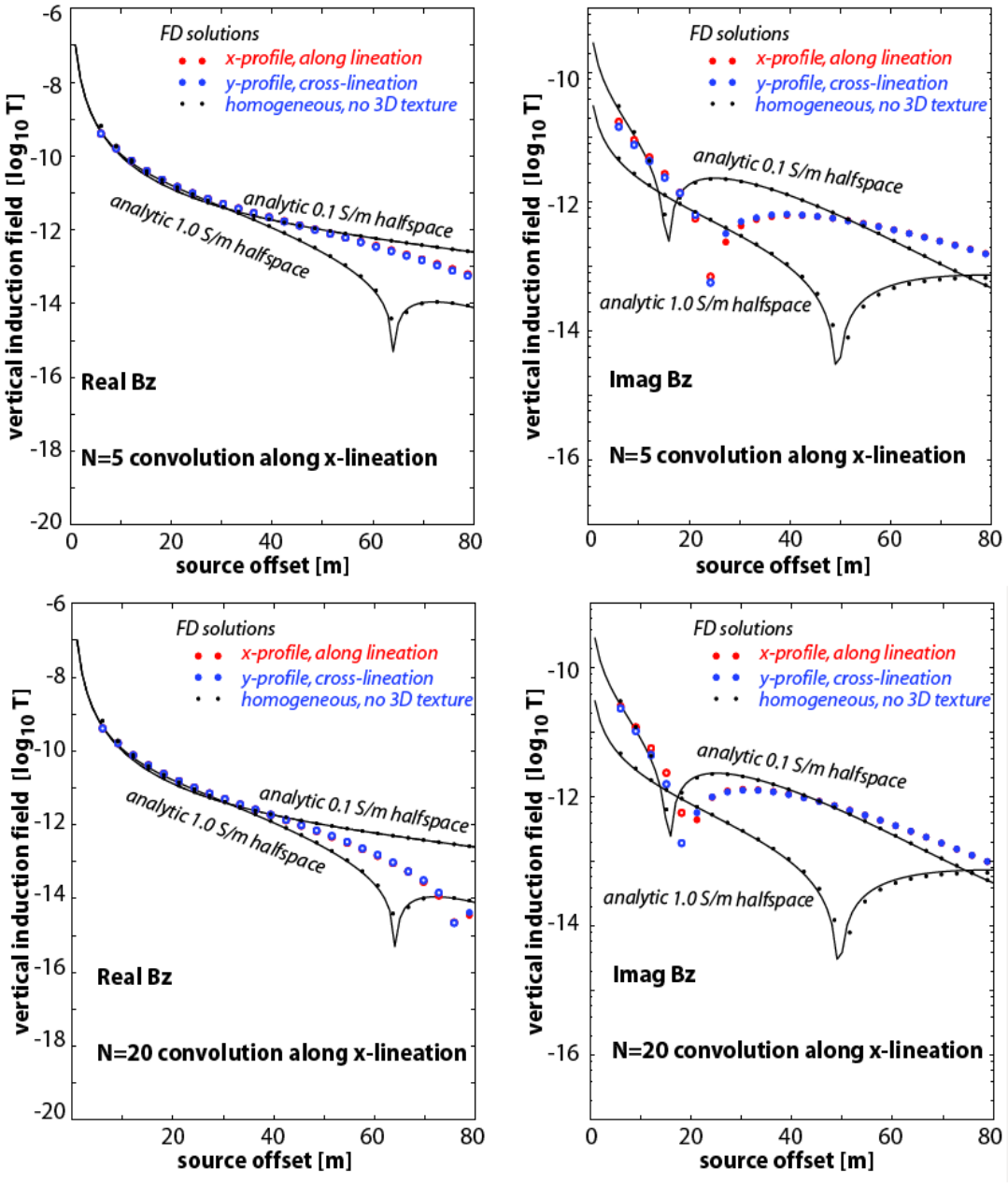

Figure 2.4: Finite difference solutions of the homogeneous models with the ground conductivity of 0.1 and 1 S/m and the unidirectional lineated models with $N = 5$ and 20 degree of correlation which are textured in the conductivity range of 0.1-1 S/m. The first column shows the real component of the resulting vertical induction field; the second column shows the imaginary component. The responses of the lineated models qualitatively resemble to some intermediate responses in comparison to the responses of the homogeneous models.

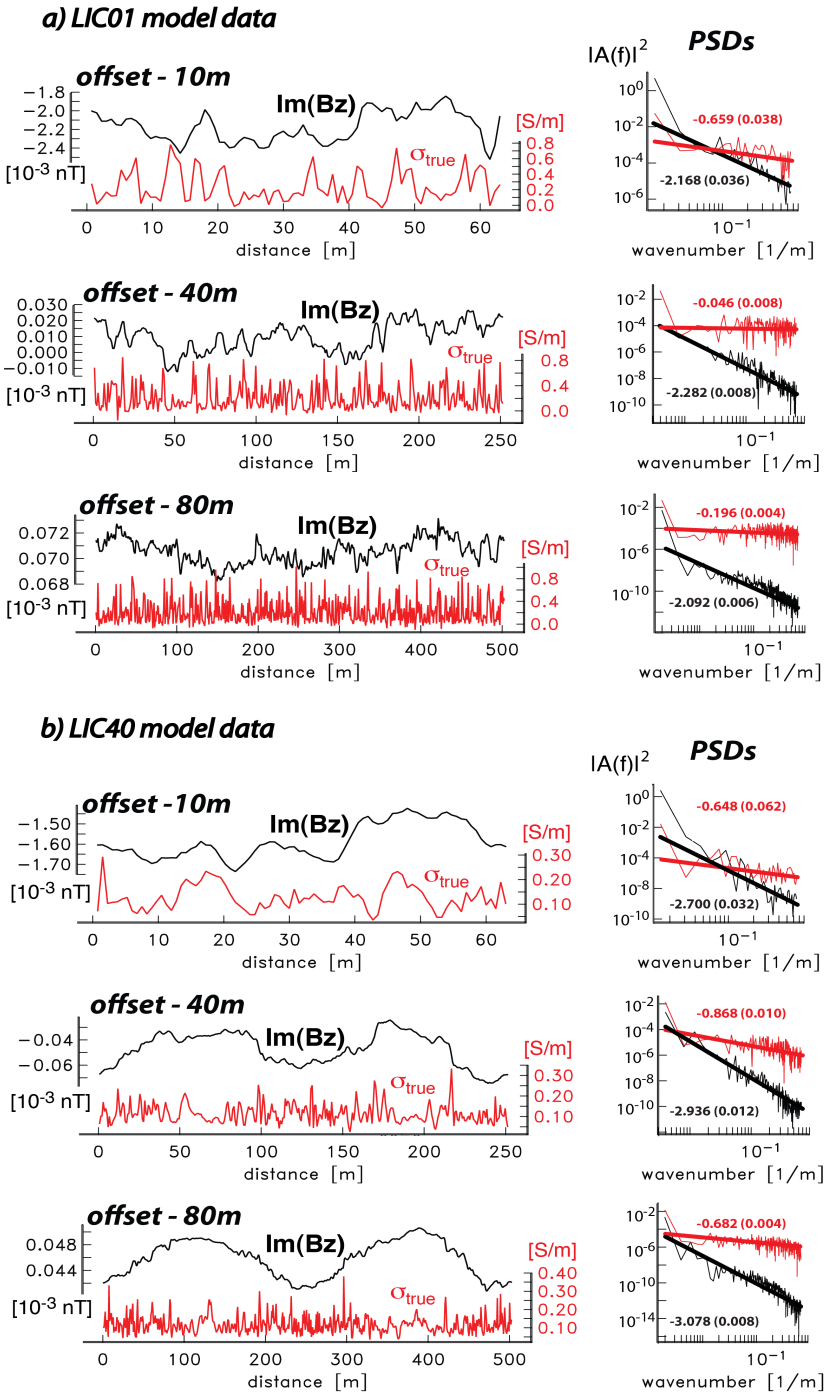

Figure 2.5: The ground conductivity (σ_{true}) and the CSEM responses (Im(Bz)) profiles along the circular survey paths and their corresponding PSDs are shown above. The PSDs are presented with their best-fit lines calculated by the jackknife procedure. The β values represent the slopes of the best-fit lines. (a): The conductivity and the CSEM profiles (LIC01), and their PSDs for a randomly populated model (convolution length, N=1) for 10 m, 40 m, 80 m TX-RX intercoil spacing. (b): The σ_{true} and the CSEM profiles (LIC40 model), and their PSDs for the x-lineated geologic texture model (convolution length, N=40) for 10 m, 40 m, 80 m TX-RX intercoil spacing. A PSD slope $|\beta| > 1$ is characteristic of fractional Brownian motion. The PSD slopes of the CSEM responses (in black) indicate a fBm with the slopes of $|\beta| > 1$.

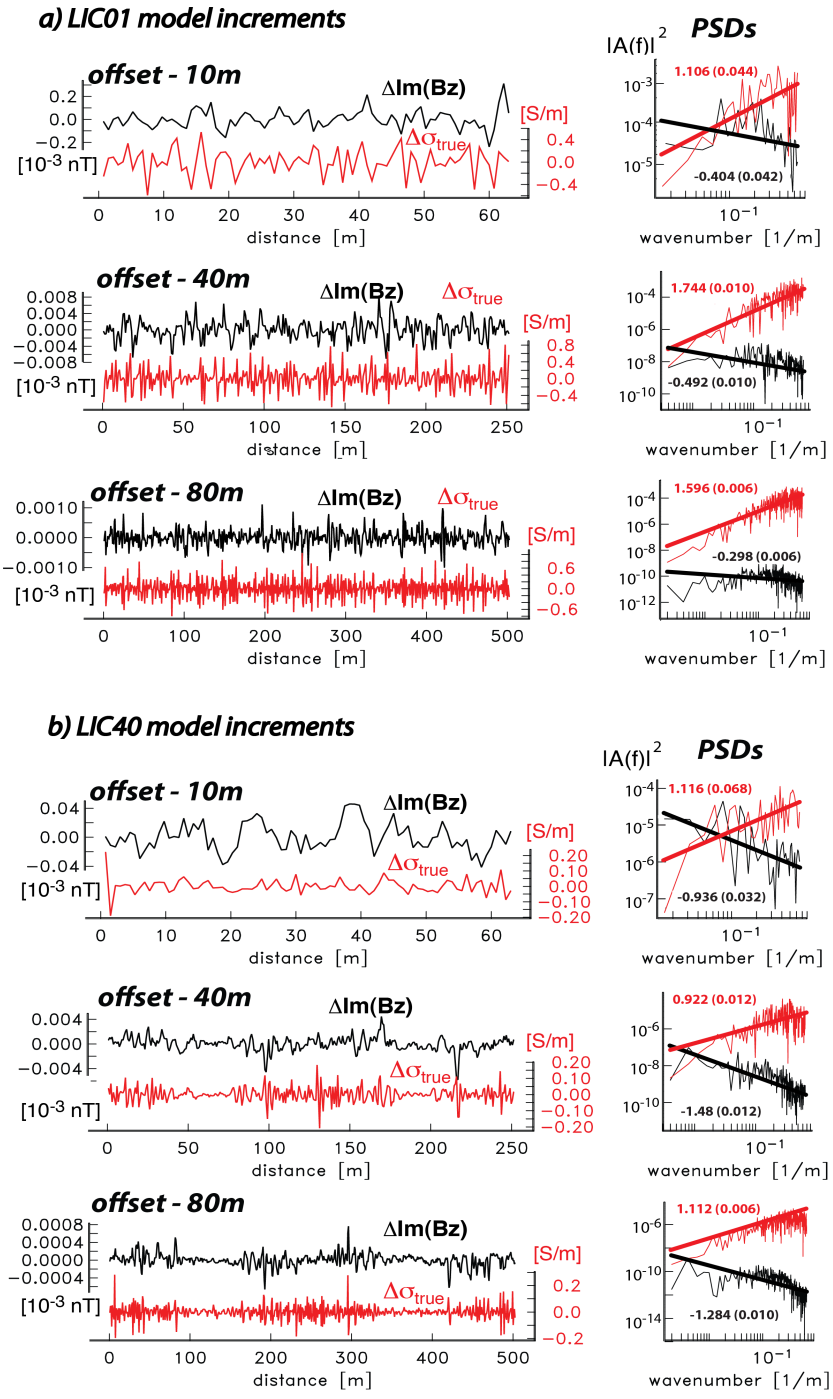

Figure 2.6: The increments of σ_{true} and the CSEM profiles shown in Fig 2.5 and their corresponding PSDs are shown above. The slopes of the increments of the CSEM responses for the x-lineated geologic textured model indicates that the increments of the CSEM responses are fractional Gaussian noise ($|\beta| < 1$).

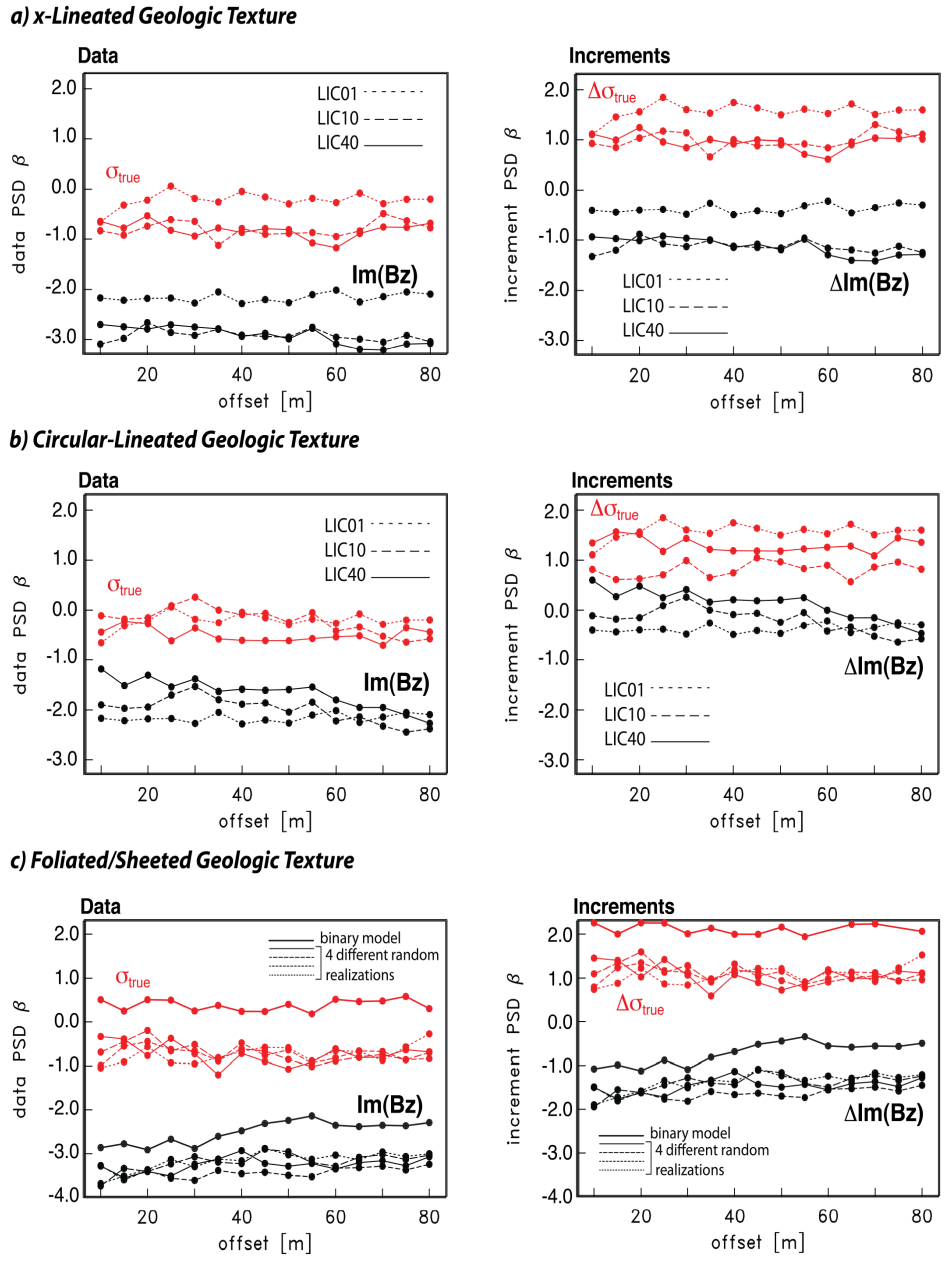

Figure 2.7: The slopes (β) of the PSDs of σ_{true}, the CSEM responses and their increments respect to the TX-RX offset for (a): the x-lineated geologic texture models (b): the circular-lineated geologic texture models (Fig. 2.2) with convolution length $N = 1, 10, 40$ and (c): a binary model whose sheets are 0.1 S/m and 1 S/m repeatedly and 4 different foliated models as sheeted with random conductivity in the range of [0.1 S/m, 1 S/m].

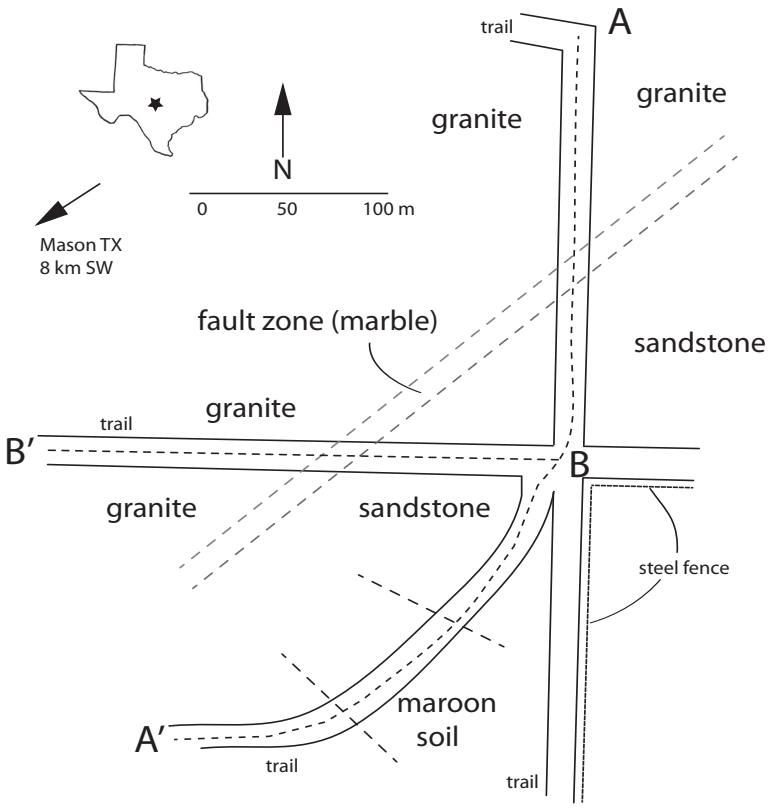

Figure 2.8: Site map, showing the lithologic units in the field and the locations of the EM survey profiles $A - A'$ and $B - B'$.

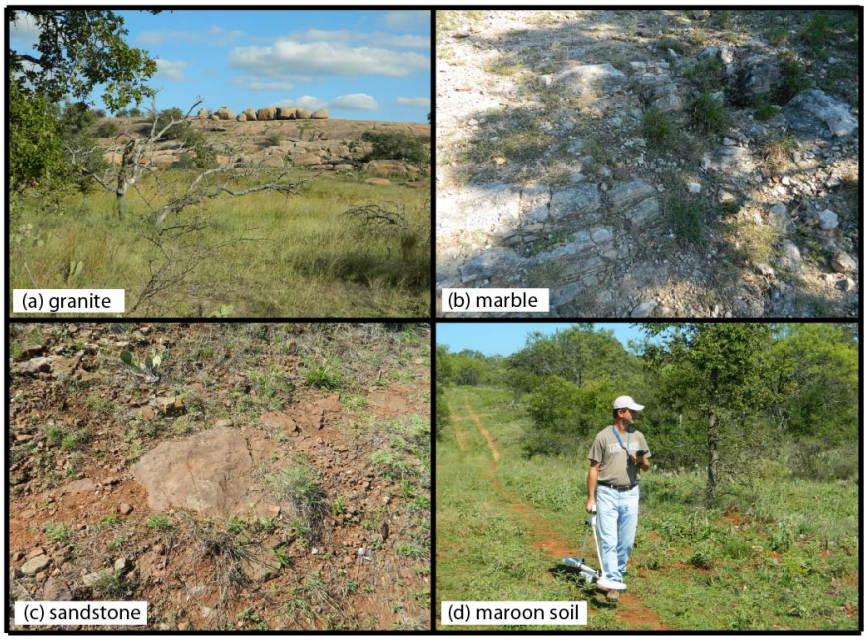

Figure 2.9: Photos of (a) Precambrian age Town Mountain granite, (b) Precambrian marble, (c) The Hickory Sandstone, (d) acquiring EM data using GSSI EM-Profiler along weathered maroon soil (photo credit: Elaine Everett).

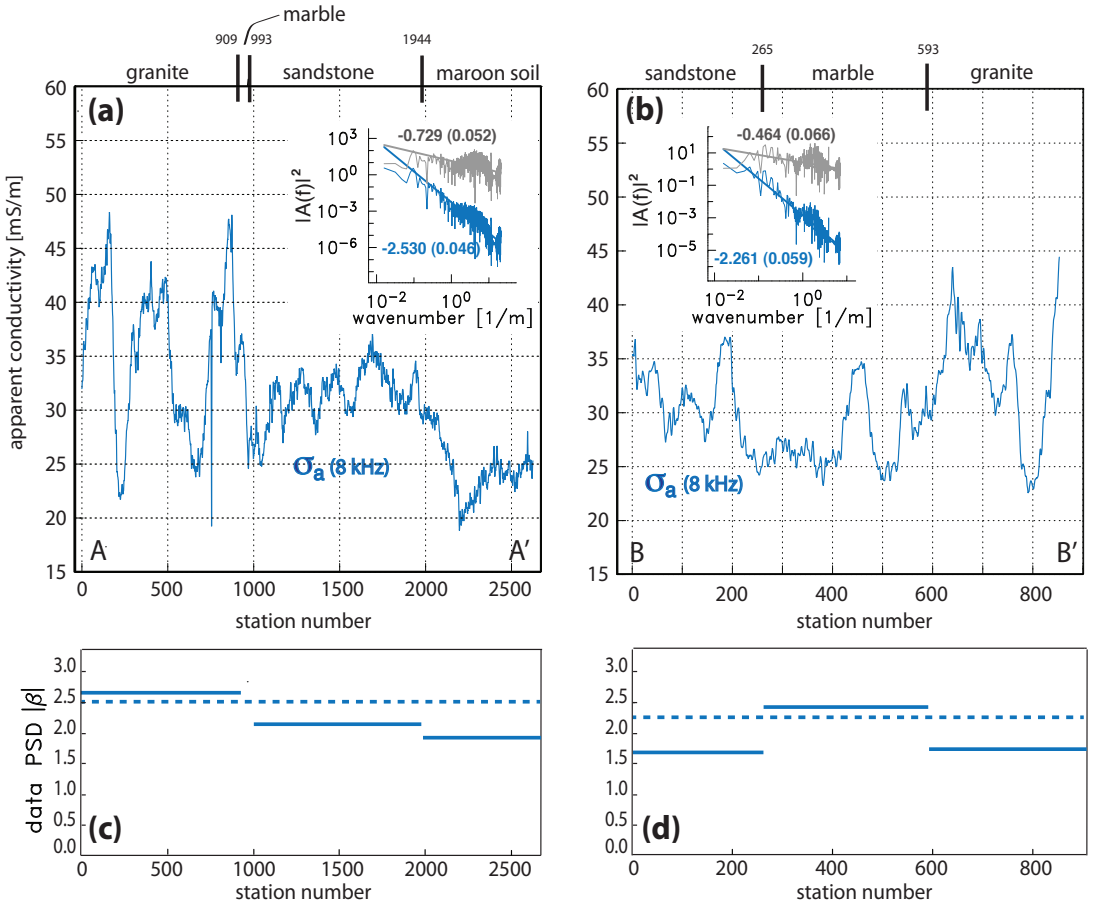

Figure 2.10: The observed apparent ground conductivity profile (σ_a, in blue) along (a) $A-A'$ and (b) $B-B'$ survey lines. PSDs of the apparent conductivity profiles (in blue) and their increments (in gray) are shown with their best-fit lines in the inset. Lithological boundaries are marked with their corresponding station numbers. The PSD β slope variations along (c) Profile $A-A'$ and (d) Profile $B-B'$ are shown. Solid lines represents the corresponding PSD slopes of the different lithologic units in the field. The dash lines indicates the PSD slopes of the entire profiles. The PSD slope of the narrow fault zone (marble) along Profile $A-A'$ is not considered, owing to the limited number of readings.

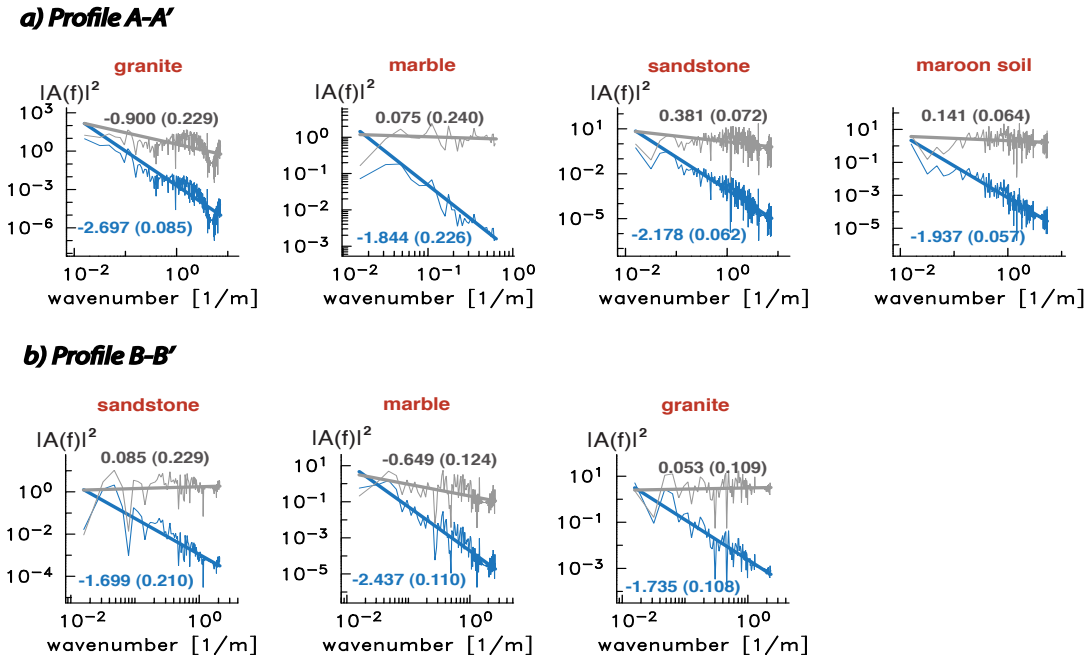

Figure 2.11: The PSDs of the apparent ground conductivities (σ_a, in blue) and their increments ($\Delta\sigma_a$, in gray) are shown with their best-fit lines for (a) Profile $A - A'$ and (b) Profile $B - B'$.

Chapter 3

A Comparison of Earthquake Back-Projection Imaging Methods for Dense Local Arrays

†**Citation:** Beskardes, G.D., Hole J.A., Wang K., Michaelides M., Wu Q., Chapman, M.C., Davenport K.K., Brown L.D. and Quiros D.A. (*in preparation*). A Comparison of Earthquake Back-Projection Imaging Methods for Dense Local Arrays.

Abstract

Back-projection imaging has recently become a practical method for local earthquake detection and location due to the deployment of densely sampled, continuously recorded, local seismograph arrays. While back-projection sometimes utilizes the full seismic waveform, the waveforms are often pre-processed and simplified to overcome imaging challenges. Real data issues include aliased station spacing, inadequate array aperture, inaccurate velocity model, low signal-to-noise ratio, large noise bursts, and varying waveform polarity. We compare the performance of back-projection with four previously used data pre-processing methods: raw waveform, envelope, short-term averaging / long-term averaging (STA/LTA), and kurtosis. Our primary goal is to detect and locate events smaller than noise by stacking prior to detection to improve the signal to noise ratio. The objective is to identify an optimized strategy for automated imaging that is robust in the presence of real-data issues, has the lowest signal-to-noise thresholds for detection and for location, has the best spatial resolution of the energy release at the source, preserves magnitude, and considers computational cost. Imaging method performance is assessed using a real aftershock dataset recorded by the dense AIDA array following the 2011 Virginia earthquake. Our comparison show that raw-wavefrom back-projection provides the best spatial resolution, preserves magnitude, and boosts signal to detect events smaller than noise, but is most sensitive to velocity error, polarity error, and noise bursts. On the other hand, the other methods avoid polarity error and reduce sensitivity to velocity error, but sacrifice spatial resolution and cannot effectively reduce noise by stacking. Of these, only kurtosis is insensitive to large noise bursts and performs as efficient as the raw-waveform method to lower the detection threshold; however, it

does not preserve the magnitude information. For automatic detection and location of events in a large dataset, we therefore recommend back-projecting kurtosis waveforms, followed by a second pass on the detected events using noise-filtered raw waveforms to achieve the best of all criteria.

3.1 Introduction

Reverse-time migration (RTM) is traditionally used as an imaging algorithm in exploration seismology to delineate structural boundaries (McMechan, 1983; Whitmore, 1983; Kosloff and Baysal, 1983; Loewenthal and Mufti, 1983; Baysal et al., 1983; Levin, 1984). RTM utilizes the reversibility of the wave equation which enables extrapolation of an observed seismic wavefield backward in time. By using recorded seismograms as time-dependent boundary values, RTM computes the wavefield back in time and space through a known seismic velocity structure to the energy source or to a diffractor secondary source. The result is an image of the source or scatterer when and where the released energy converges (McMechan, 1982; Baysal et al., 1983; Chang and McMechan, 1987). RTM was first developed for reflector imaging using controlled active sources as an alternative to depth extrapolation-based migration techniques, where diffractors and reflectors are secondary source. This approach can be also applied to earthquake data to determine the earthquake source in both time and space (McMechan, 1982). Early papers showed that imaging of real earthquake point sources as well as spatially and temporally extended sources is feasible via RTM if the recording aperture is sufficiently large and the data are not spatially aliased at wavelengths of interest (e.g. McMechan, 1982; McMechan, 1985; McMechan, Wen and Morales, 1988; Chang and

McMechan, 1991; Rietbrock and Scherbaum, 1994). RTM requires both a densely-recorded dataset and a very good velocity model for the accuracy of the wave equation's computation, and real datasets satisfying these prerequisites were not generally available in earthquake seismology.

RTM can be simplified in the form of back-projection imaging (BPI) by ignoring amplitudes during wavefield propagation and of the source focal mechanism. The BPI does not require extensive wavefield computations and is based on time-shifting observed seismograms based on travel-time computation through a known velocity model. Stacking the time-shifted traces will correctly image energy release at the source, but absolute amplitudes of source projection and focal mechanisms can not be recovered.

Relevant datasets for BPI have become more available recently due to denser regional networks as well as dense local temporary array deployments and therefore BPI has become more widespread in earthquake seismology. The method has been applied to large-magnitude earthquakes to back-project energy in time and space through a global velocity model to its source. Successful images of earthquake sources have been produced without phase picking or discrimination of different phases, imaging the rupture/slip time as a function of space and time without a priori knowledge of fault geometry or duration (e.g. Kao and Shan, 2004; Ishii et al., 2005; Kiser et al., 2011; Kiser and Ishii, 2012). Back-projection is scalable to earthquakes with a wide range of magnitudes. In addition to large subduction-zone earthquakes (e.g., Ishii et al., 2007; Kiser and Ishii, 2012; Koper et al., 2012), BPI has been applied to large to moderate-sized earthquakes on a thrust belt in China (Xu et al., 2009), a normal fault in Italy (D'Amico et al., 2010), and a strike-slip fault in northern Tibet (Walker

and Shearer, 2009).

Local dense array deployments have recently become feasible, capturing full seismic wavefields rather than isolated waveforms. It has therefore become possible to capture very tiny events by having more stations closer to the epicenter and by eliminating or drastically reducing spatial aliasing, enabling inter-station correlation and wavefield imaging. Additional stations near the epicenter enables the detection of smaller events using traditional single-station records, simply because more stations are likely to observe signal above the noise. However, events that produce signals similar or smaller than the noise cannot be detected by single-station triggering methods, regardless of relevant station spacing. Station-to-station correlation of weak signal on stations that are not spatially aliased enables visual detection of events smaller than the noise. Spatial-temporal coherency methods (e.g., Neidell and Taner, 1971) could enhance and automatically detect this signal. Alternatively, direct imaging methods such as migration can stack this energy at its source, improving the signal to noise ratio, and detection can occur using the stacked signal. BPI stacking of a large number of seismograms has recently been used to detect and locate tiny events smaller than noise that traditional methods fail to detect (e.g., Xu et al., 2009, Chambers et al., 2010). The identification and characterization of smaller events could enable an improved understanding of how rupture and slip processes scale to small size and of the transfer of stress by static, dynamic, and fluid processes. BPI has been used to detect hydraulic fracturing in the hydrocarbon industry (e.g., Gajewski and Tessmer, 2005; Chambers et al., 2010; Artman et al., 2010; Zhebel and Eisner, 2012, Vlček et al., 2015), tectonic microseismicity (e.g., Hole et al., 2014, Inbal et al., 2015, Ben Zion et al., 2015) and volcano seismicity (e.g., Haney, 2014, Langet et al., 2014, Hansen and Schmandt, 2015), Other obvious applications include

induced seismicity associated with wastewater or CO_2 injection, stimulation in enhanced geothermal energy systems, and mining rock-burst hazard studies.

BPI consists of two basic processing steps; time-shifting and stacking. The efficiency of these steps is strongly affected by the quality of seismic data and inaccuracies in the velocity model. Real earthquake data that possess a low signal-to-noise (S/N) ratio resulting from seismic background noise, incoherent noise bursts generated by human activities or weather conditions, and opposite polarities of arrival onsets associated with the source radiation pattern have a large influence on the effectiveness of stacking. BPI stacking may not be succeed due to signal below seismic noise levels or coherent seismic noise (Chambers et al., 2010); large noise bursts cannot be cancelled by stacking because they are spatially aliased or incoherent across the array; or coherent earthquake waveforms can stack destructively due to opposite focal-mechanism polarities. A poor velocity model produces inaccurate time delays for BPI and either destroys by destructive interference or smears the source image.

Several methods have been proposed to overcome these challenges to make this inherently simple imaging procedure robust for automation. Based on the stage that these methods are carried out, it is possible to consider them as either simultaneous or preprocessing methods. Particularly, the simultaneous methods aim to avoid the imaging issues by weighting time-corrected seismograms by different attributes prior to stacking. For instance, the diversity stack, which is based on scaling shifted seismograms inversely proportional to their powers calculated in a certain time gate (Embree, 1968), can be used to minimize the effects of non-equal noise, such as noise bursts and spikes. Similarly, the median stack uses the ratio of the time-gated maximum absolute value of each seismogram to the median absolute value

as weighting coefficients during stacking (Anderson and McMechan, 1989). Coherency-based methodologies such as the semblance stack (e.g., Neidell and Taner, 1971, Chambers et al., 2010) or cross-correlation weighting (Eisner et al., 2008) can enhance coherent signal as well as be used to adjust residual time shifts to better align seismograms (Ishii et al., 2007).

Using the absolute value of amplitudes of normalized seismograms during stacking (source scanning algorithm; Kao and Shan, 2004); flipping waveforms according to the coherency of phase amplitudes (phase doubling method; Drew et al., 2014); or correcting the polarities according to a pre-known radiation pattern (Vlček et al., 2015) can be employed to avoid the effects of opposite polarities caused by the source focal mechanism. Alternatively, moment tensor inversion can be simultaneously incorporated into BPI by inverting for the spatial variation of polarization (e.g. Gharti et al., 2011; Zhebel and Eisner, 2012; Chambers et al., 2014). A third approach is to abandon polarity by converting the data to their envelope (e.g., Gharti et al., 2010), signal-to-noise ratio via short-term average divided by prior long-term average (STA/LTA) (e.g., Vlček et al., 2015, Trojanowski and Eisner, 2016), or kurtosis, the fourth moment of local amplitude distribution (e.g., Langet et al., 2014). While these methods avoid the polarity problem by producing a positive signal that will always constructively stack, the noise will also constructively stack, losing the benefits of improving the signal-to-noise ratio.

The aforementioned simultaneous methods and similar stacking techniques can be applied individually to improve the efficiency of the shift-and-stack process or in tandem with the aim of overcoming more than one imaging challenge. On the other hand, the simultaneous application of these approaches imposes repetitive calculations for any given speculative

hypocentral location and earthquake time in a large search volume, and consequently imposes a high computational cost. One common strategy to avoid extensive computations is to carry out BPI for only time windows predetermined by a priori event detection as employed by teleseismic and hydraulic fracturing studies. However, this means that BPI will only detect and locate the events that were previously detected on single seismograms, losing the benefits of stacking to detect smaller events.

Our primary objective in this study is to continuously and automatically migrate the entire dataset recorded by a dense array to fully take advantage of stacking to detect and locate the smallest possible events. For this reason, we consider preprocessing methods for event detection and location that utilize raw seismograms or simple pre-processed waveforms and do not require extra computational effort during the BPI procedure. We evaluate the performances of four previously used pre-processing methods: the raw seismogram, envelope, short-term average / long-term average (STA/LTA) and kurtosis. We examine their effectiveness on overcoming real data issues by considering their capabilities to achieve: the lowest detection and location thresholds in the presence of a low S/N ratio, the best spatial resolution for the source images, and magnitude preservation, as well as computational efficiency for an entirely automated imaging process for continuously-recorded earthquake data. Towards identifying an optimum imaging strategy, we present a comparison using real data from the 2011 Virginia aftershock data recorded by the dense AIDA array.

3.2 The 2011 Virginia Aftershocks recorded by Aftershock Imaging Dense Array (AIDA)

The Aftershock Imaging with Dense Arrays (AIDA) project (Davenport et al., 2015; Quiros et al., in press) recorded 12 days of the aftershock sequence following the 23 August 2011 Mw 5.7 earthquake in central Virginia (Chapman, 2013, McNamara et al., 2014). AIDAs goal was to drastically reduce spatial aliasing and thereby to lower detection and location thresholds for aftershocks as compared to traditional aftershock networks. AIDA utilized 4.5-Hz, vertical-component geophones recorded by Reftek RT-125A "Texan" seismographs at 200-400 m spacing and 100 samples per second. Both spacing and temporal sampling were limited by 1990s technology that limited memory and power, requiring frequent site visits. In the first week, 103 stations were deployed (Lines 1 and 2, Fig. 3.1), and 116 stations in were deployed the second week in a revised array geometry (Lines 1, 2, 4, 5 and 6, Fig. 3.1) to better cover the updated mainshock's hypocenter and aftershock zone. AIDA recorded earthquake magnitudes from –1.8 to 3.6 (Davenport et al., 2015) and complete to M–1 (Fig. 3.2) (Chapter 4). A 3D seismic velocity model for a 12 km x 12 km x 9 km volume was derived by tomographic inversion of P- and S-wave arrival times for more than 300 aftershocks. The best 3D model is a constant P-wave velocity of 6.2 km/s and S-wave velocity of 3.62 km/s, indicating homogeneity within a single crystalline-rock terrane (Davenport et al., 2015). The 50 Hz Nyquist frequency reduced signal to a dominant frequency of 25 Hz, corresponding to an average dominant wavelength of ~250 m for the P-wave.

The AIDA data is a continuous 12-day record of the aftershocks that comprises different array geometries, different signal-to-noise ratios and large noise bursts generated by traffic,

wind, tropical storm, and thunderstorms, as well as spatially varying polarizations due to source radiation patterns. This makes the AIDA dataset representative of realistic data issues and suitable for an objective comparison of BPI methods. We only consider events recorded during the second week when the array has a better array coverage.

3.3 Back-projection Imaging

RTM and BPI imaging are based on propagating the emitted seismic energy backward from observed seismograms to the source in time and space. The classical RTM imaging problem is performed by computing the elastic wave equations backward in time from the observed seismograms (McMechan, 1982). To reduce computational cost, BPI acts as a simple time shifting and stacking process of the recorded seismograms (Ishii et al., 2005). Observed energy is stacked along arrival time curves (moveout curves) corresponding to the travel time between the hypocenter and each station (Fig. 3.3):

$$Stack_i(t) = \frac{1}{N}\sum_{k=1}^{N} S_k(t - t_{ik})$$

where $Stack_i(t)$ is the stack seismogram for the ith grid point, $S_k(t)$ is the observed seismogram at kth station, N is the number of stations, and t_{ik} is the predicted travel time from ith grid point to kth station calculated from a known 3D velocity model (Ishii *et al.*, 2007). Either P or S waves can be imaged by using the appropriate velocity model; only P waves are used here.

By assuming that the true source location is within the 3D search grid and every grid point is a potential source, the seismograms are time-shifted according to the predicted travel times from each possible source location to each station and stacked for each potential source location. If the grid point is the true hypocenter, the arrivals will be lined up after time shifting and will stack constructively at the earthquake time. For other grid points, they will not align and will stack out. This repetitive process produces a 4D BPI image comprising the time history of the stack amplitude at each potential hypocenter within the search volume. Each events hypocenter is indicated by a maximum in amplitude at the corresponding grid point and earthquake time.

For automated event detection and location for a large dataset, the search volume needs to span a large 3D zone that comprises the suspected seismicity zone. A full 3D image of potential hypocenters exists for each time step, typically the sampling interval. Thus, storing the 4D imaging results requires excessive computer storage. Therefore, 4D imaging results must be searched and event detections made as the volume is being computed. Standard threshold or running triggering algorithms (e.g., STA/LTA) could be performed on stack amplitude traces of every grid node. A simpler method is to store the maximum stack value that occurs anywhere within the 3D volume at each time, the "maximum stack seismogram". Additional time series are saved to record the grid locations of the maximum at each time. Standard detection algorithms can then be applied to the maximum stack seismogram. Herein we record and use for detection the trace energy calculated by integrating over 4 samples, corresponding to the dominant period of the signal. The advantages of using the maximum stack seismogram are trivial storage requirements (4 time-series) and the ability to test and tune the detection algorithms for post-imaging. The disadvantage is

the potential to miss events that overlap in time. Once detected, it is trivial to re-compute the BPI for the tiny space-time volume containing the hypocenter if we wish to inspect the 4D image. The largest computational effort is in back-projecting at all possible hypocentral points in the large search volume through all time. For a zone of seismicity that is 10s of km in size and signal at 10s of Hz requiring a grid sampling of 25-100 m, BPI must be computed to $10^7 - 10^9$ grid points.

The advantage of detection via RTM or BPI is that stacking increases the signal-to-noise ratio, enabling the detection of smaller events. In addition, many events that can be detected by single-station (non-stack) methods cannot be located due to the small number of sparse stations that recorded them,. Dense-array RTM and BPI cannot only detect smaller events, but all of these events are automatically located. In addition, as we will demonstrate below, the hypocentral accuracy is comparable to double-difference methods.

3.4 Influence of the Array, Noise, and Velocity model

The impulse response of BPI to a point-source earthquake is a function of both time and space. This is due to the band-limited frequency of the recorded signal, to the aperture and station spacing of the array, to the inevitable tradeoff between earthquake time and distance from the array, to errors in the velocity model, and to seismic noise.

3.4.1 Recording Array

Fig. 3.4 illustrates the P-wave impulse response (array response) of BPI to a point source earthquake as it would be recorded by the second-week AIDA array. The 4D source image (Fig. 3.4b) shows that the maximum stacked amplitude migrates through time, growing and shrinking in amplitude. While we call this the shooting star artefact, it is the same as the swimming artefact of Koper et al. (2012). It represents a tradeoff between earthquake time and distance from an amplitude-weighted centroid of the station array. The shooting star moves from earlier earthquake time further from the array and moves towards the centroid of the array with time. For an earthquake beneath the array, such as for Fig. 3.4, the shooting star is roughly vertical, but for other events, including those outside the array, the shooting star will point along the raypath direction towards the array centroid. Only an ideal array that completely surrounds the event can prevent this artefact, which of course is impractical. Fig. 3.4d illustrates that the shooting star is different for the week-1 AIDA array, which is not as well centered over the event. The length of the shooting star is controlled by the aperture (spatial extent) of the array and the distance of the event from the array (e.g., Artman et al., 2010). Together, these parameters control the solid angle of rays taking off from the source towards active stations. Higher frequencies are more sensitive to temporal changes in moveout during stacking, and therefore to changes in earthquake location that cannot accurately trade off with event time. Lower frequencies therefore produce a longer shooting star. Since the shooting star systematically grows and shrinks in amplitude, passing through a maximum, we choose this maximum as the preferred, best-stacking 4D hypocenter, while measuring temporal and spatial resolution as elongated along the shooting star.

Fig. 3.4a shows the BPI image at the preferred earthquake time. It is roughly spherical, and has a full width of ~250 m, corresponding to the dominant wavelength at the dominant ~25 Hz frequency of the data. This size scales proportional to the frequency content of the data (e.g., Artman et al., 2010). The peak energy indicating the hypocenter can be more accurately measured, at a fraction of a wavelength. We measure uncertainty as the distance and time at 95% of the maximum stack energy, producing errors < 50 m and < 20 ms, or about 1/5 of the dominant wavelength and period. Assuming the velocity model is accurate, these errors represent absolute hypocentral accuracy of a fraction of a wavelength. Thus, relative hypocentral locations are comparable to that achieved by double-difference methods; arrival-time alignment and stacking effectively perform the cross-correlation and minimization in the double-difference method.

Also visible in Fig. 3.4a are low-amplitude curved smearing artefacts that are dominantly perpendicular to the shooting star artefact. These are migration artefacts caused by the array aperture, resulting from incomplete destructive interference by stations missing beyond the array. Figs. 3.4c-d illustrate larger artefacts of this type for AIDAs first-week array due to its smaller aperture further from the events. Similar artefacts, but non-symmetric and non-perpendicular to the shooting star, are created by aliased spatial sampling in the cross-line direction, due to spacing between the sparse AIDA lines (Figs. 3.4a-d).

3.4.2 Seismic Noise

Real data records a variety of seismic noise sources, including random background noise and local events. Large noise bursts can caused by nearby human activities such as traffic or

weather effects such as wind and lightning. Seismic noise substantially masks the waveforms generated by the very small events we aim to target. BPI does not require the arrivals of such weak events to be detectable on individual seismograms but to be large enough at a sufficient number of stations so that stacking can boost the signal above noise. Noise bursts are incoherent and spatially aliased, and their amplitudes are often many times larger than the recorded weak signals. These high amplitude bursts cannot be easily suppressed by stacking a large number of seismograms and can act as false triggers during event detection. Manual denoising is not feasible for continuous recordings and automated approaches applied during BPI such as sliding coherency, diversity, or median filters impose additional computation time at each potential hypocenter, which makes the pre-processing approaches more advantageous for large volumes of data.

S waves and surface waves produce large amplitudes following the P waves on earthquake seismograms. The arrivals of these phases do not align after BPI time shifts computed using P-wave velocities for any possible subsurface hypocenter (Fig. 3.2b). Thus they destructively interfere during stacking. In practice, however, the large amplitudes must be over-sampled to fully cancel out. In addition, the slower velocities are more easily spatially aliased. If so, they will partially stack in owing to cycle skips in their waveforms recorded at nearby stations. The remaining S-wave energy can act as a false trigger on BPI maximum stack seismograms. This S and surface wave zone may mask P waves generated by a subsequent event and may act as a shadow zone for event detection. For AIDA, the S waves are weakly aliased inline and badly aliased between the sparse array arms, resulting in only partial cancellation during stacking.

BPI does not inherently take account of spatially varying polarization of recorded waveforms caused by the earthquake radiation pattern, but it can be included as a correction term (e.g., Ishii et al., 2005). If not corrected, a mix of positive and negative polarity will reduce the desired signal by destructive interference. For large events, automated cross-correlation methods can identify and correct polarity, but it is very difficult for smaller events with low signal-to-noise ratio such as those targeted here. The percentage of positive and negative polarity depends upon the focal mechanism of the event and the relative location and geometry of the array. A balanced mix seems unlikely, so some signal seems likely to stack in. However, one can imagine an array that is centered on a fault, the focal plane, that mostly stacks out the signal. Avoiding the problem of polarity is one of the primary reasons many authors apply pre-processing to produce a strictly positive signal (e.g., envelope, STA/LTA, kurtosis).

3.4.3 Velocity Model

BPI is based on the assumption that the velocity model is accurate. Inaccuracies in the model lead to errors in the predicted travel times used to shift the data, and thus result in misaligned signal during stacking. This results in spatial and temporal smearing and weakening in amplitude of BPI source images, and could ultimately result in failure to detect an event. Higher frequency waveforms are more sensitive to small-scale errors in the velocity model (e.g,. Usher et al., 2013). Errors in the velocity model also result in systematic mis-location of the hypocenters. A tradeoff between velocity and location affects absolute accuracy, but not relative accuracy. A densely sampled array is capable of producing a high-quality

velocity model by auto-picking large events that are well-distributed through the aftershock volume and performing high-resolution local earthquake tomography (e.g., Davenport et al., 2015). However, local earthquake tomography using traditional earthquake arrays is incapable of producing a high-resolution velocity model for high-frequency imaging. The second primary reason (along with polarity) that many authors use pre-processed waveforms for BPI is to overcome inaccuracies in the velocity model. Pre-processing that produces a temporally broader signal (e.g., low-frequency filter, envelope, STA/LTA) reduces sensitivity to the velocity model. Pre-processing that produces a strictly positive signal (e.g., envelope, STA/LTA, kurtosis) disables destructive interference by the misaligned negative phase of the waveform. Both intentionally sacrifice spatial resolution for imaging robustness. In this manuscript, we do not explore errors in the velocity model.

Based on the issues and challenges described in this section, we define our imaging goals towards an efficient and robust strategy for automated BPI: high spatial resolution of source images, detection and location with low signal-to-noise, and robustness in the presence of opposite polarities, large noise bursts and spatially-aliased, large S-waves. Due to the value of magnitude in an earthquake catalog, we also include magnitude preservation as an imaging goal.

3.5 Preprocessing Methods

To overcome the aforementioned challenges arising from real data issues and the effects of array geometry and the velocity model, raw seismograms can be pre-processed into simpler forms. We herein consider three characteristic functions of raw seismograms: envelope,

short-term average / long-term average (STA/LTA), and kurtosis (Fig. 3.5). All of these methods have been used for automatic picking algorithms as well as for pre-processing for BPI.

The envelope of a seismogram is the amplitude of its analytic signal, which can be calculated via Hilbert transform. The envelope has amplitude similar to the raw seismogram, but is much smoother with a broader, strictly positive, peak of lower effective frequency (Fig. 3.5b). Due to this simple structure, it has long been used for automatic picking algorithms (e.g., Baer and Kradolfer 1987). It has also used as input for BPI to avoid cycle skipping in stacking created by incorrect time alignment caused by a poor velocity model (e.g., Hansen and Schmandt, 2015), and to overcome the opposite polarization caused by the source mechanism (e.g., Gharti et al., 2010).

The STA/LTA method measures the energy signal-to-noise of a seismogram using two adjacent moving time windows (Allen, 1978). The average energy within a short window (STA) captures the strong first arrival of an event, while the average energy within the preceding long window (LTA) is a measure of the background noise. STA/LTA produces a time series that represents an abrupt increase in energy coincident with strong arrivals. With appropriate tuning of the window lengths, the large positive peak can be as short as half the dominant period of the raw seismogram (Fig. 3.5c). STA/LTA time series are commonly used as an event detector in global seismology (e.g. Withers et al. ,1998), local microseismic studies (e.g., Wu et al., 2015) and hydraulic fracturing studies (e.g. Miyazawa et al., 2008, Forghani-Arani et al, 2013). A STA/LTA detection triggering threshold of ~4 is a typical compromise between minimizing false triggers and maximizing detection of small events

(e.g., Trnkoczy, 1998). A 5-sample STA and an immediately preceding 45-sample LTA time window provided robust event detection on individual seismograms for the AIDA dataset, which contained earthquake signal up to the Nyquist frequency. STA/LTA is commonly used for BPI to eliminate the negative lobes of the seismogram, eliminating the polarity problem and reducing the dependence upon the starting model by eliminating destructive interference (e.g., Drew et al., 2005; Michaud and Leaney, 2008; Grigoli et al. 2013 and 2014, Vlček et al., 2015, Trojanowski and Eisner, 2016).

Kurtosis is the fourth central moment in statistics, which includes dependency on the three previous moments (mean, variance, and skewness). This coefficient describes the shape of a statistical distribution and is a measure of peakedness in relation to tails (Spanos, 1999). Usually relative kurtosis, or the fourth moments difference from a Gaussian, is cited. A positive relative kurtosis indicates a distribution with a larger central peak and larger tails than a Gaussian and smaller values at one standard deviation from the mean; negative kurtosis is the reverse. Using the amplitudes of the samples in a seismic time window as the density distribution, background seismic noise has a slightly negative relative kurtosis (near Gaussian) while an impulsive earthquake arrival has a positive kurtosis (Fig. 3.5e). This characteristic difference in the density distributions enables kurtosis to be used as an earthquake detector that produce more accurate results for phase picking compared to other traditional methods (e.g. Saragiotis et al., 2002; Kuperkoch et al., 2010; Nippress et al., 2010; Ross and Ben-Zion, 2014). For BPI, it has similar advantages to STA/LTA in eliminating polarity and reducing sensitivity to the velocity model (e.g., Langet et al., 2014). Rather than using the kurtosis itself, Langet et al. (2014) used the positive gradient of the kurtosis in order to obtain a sharper peak (Fig. 3.5e); we adopt this method. The sensitivity of

the kurtosis method is calibrated by the size of the moving time window that defines the distribution and is affected by the frequency of data. We found that a 50-sample moving window provides the optimum sensitivity for the AIDA dataset.

3.6 Comparison Results

We compare the performances of BPI using raw, envelope, STA/LTA and kurtosis seismograms. Our evaluation for the effectiveness of these methods is based upon our imaging goals, including: high spatial resolution; detection and location of weak events with low signal-to-noise ratio; robustness in the presence of large noise bursts, spatially-aliased large S-waves, and opposite polarization due to the source's radiation pattern, and magnitude preservation.

3.6.1 Spatial Resolution

To examine the spatial resolution of source images obtained from BPI using the four preprocessing methods, the magnitude 2.5 event of Fig. 3.2 was imaged using P waves. This event has a high S/N ratio so that imaging results are not affected by noise. The first-motion polarity (Fig. 3.2b) was manually corrected prior to stacking. To approximately preserve amplitudes, a geometric spreading correction was applied, multiplying each seismogram by the distance between the subsurface grid point and station.

Each method successfully images the emitted source energy at the same hypocenter, but with different spatial resolutions (Fig. 3.6). All include a near-vertical shooting star artefact

due to the tradeoff between distance from the array centroid (depth) and time. BPI using raw seismograms produces a well-focussed image of the source. The peak can be picked with an accuracy of ±(x: 10 m, y: 56 m, z: 74 m, t: 20 ms) at 95% of the peak energy. The other three methods show wider images with larger-amplitude migration artefacts from the array-geometry (Fig. 3.6, Table 3.1). Envelopes are the broadest representations of the raw seismograms with the widest signal in time (Fig. 3.5b) and therefore produce a BPI image with the worst spatial resolution (Fig. 3.6). BPI of the STA/LTA signal provides spatial resolution approaching that of the full waveforms, while kurtosis BPI produces an image quality between those of the envelope and STA/LTA (Fig. 3.6, Table 3.1). Both STA/LTA and kurtosis gradient have single-trace signals that are as narrow in time as the raw waveforms (Fig. 3.5), yet produce lower-resolution BPI images. This is because the lack of equally narrow negative lobes prevents destructive interference adjacent to the optimum location. Eliminating destructive interference reduces the dependence upon the starting model, spreading out the energy and reducing image resolution as errors grow in the velocity model. In contrast, the raw waveforms stack out if the velocity-model time errors are too large, preventing imaging. For a good velocity model, however, raw waveforms produce the best spatial resolution (Fig. 3.6, Table 3.1). A dense local array should enable traveltime tomography to produce a sufficiently accurate velocity model from the largest, automatically picked events (e.g., Davenport et al., 2015). Further, residual errors in traveltime alignment could be minimized in migration moveout analysis to improve the velocity model (e.g., Adler et al., 2008).

3.6.2 S-waves

The BPI normalized maximum stack seismograms for all methods (fourth column of Fig. 3.6) produce easily detectable maxima for P-waves at the event time. The maximum stack seismograms from BPI of raw seismograms and of envelopes show a wide, large-amplitude zone that follows the first detection peak (Figs. 3.6a-b). These are S-waves that are not fully cancelled by stacking using the P-wave velocity. Provided that the S-waves are spatially over-sampled, stacking raw seismograms can completely cancel the S-waves. The AIDA data are well sampled, but not sufficiently to completely remove the large S waves (Fig. 3.6a). Regardless of spatial sampling, stacking of broad, always-positive envelopes will always be sensitive to S-waves (Fig. 3.6b). Depending on how they are designed, STA/LTA and kurtosis operators tend to have insensitivity to S-waves due to the prior P-waves (Figs. 3.6c-d, Table 3.1).

While the S-waves can produce large stacked amplitudes in P-wave BPI, they do not produce focussed energy in time and space in the impulse response shooting star pattern. Therefore, spatio-temporal patterns in the 4-D images could be used to prevent false event detection from the S waves. For example, deconvolution of the 4-D shooting star impulse response can both sharpen the P-wave image and discriminate against large S-wave energy that does not have the correct pattern (e.g., Haney, 2014). Nevertheless, it is important to note that for every method, the time window of the S and surface waves is a shadow zone for detection of the next event.

3.6.3 Polarity

For the event shown in Fig. 3.2, the polarities of the first arrivals were manually corrected to produce Fig. 3.6a. The data have 30 percent negative polarization (Fig. 3.2b), so that signal amplitude is 40% of that in Fig. 3.6 after stacking without polarization correction. Fig. 3.6a (right panel) illustrates the effects of artificially reversing 0%, 30% and 50% of the seismograms. As expected, signal is reduced proportionally, illustrating the need for polarity correction for BPI of raw seismograms. The pre-processed envelope, STA/LTA, and kurtosis traces, by design, are not affected by signal polarity (Fig. 3.6, Table 3.1).

3.6.4 Low Signal-to-Noise Ratio

The detection efficiency of the methods was tested for different S/N ratios. Rather than comparing different earthquakes, random noise was added to the earthquake of Fig. 3.2 for consistency (Fig. 3.7a). Rather than using randomly generated noise that does not fully represent the nature of the seismic noise, a panel of real but visually random seismic noise was extracted from the AIDA dataset. We chose a panel of seismograms consisting of only background seismic noise, excluding noise bursts and impulsive events. The noise gathers energy was normalized between traces, and then scaled to add to the earthquake signal at a range of P-wave signal-to-noise ratios. In order to treat each method fairly, we corrected the polarities of the raw seismograms.

The resultant maximum stack seismograms show that BPI using raw seismograms and kurtosis waveforms detect the event at the lowest threshold, with a S/N ratio of ~0.6 (Figs. 3.7b

and 3.7e, Table 3.1). BPI of envelopes does not allow noise cancellation owing to the lack of negative values, and consequently requires a higher S/N ratio of 1.6 for event detection (Fig. 3.7c). STA/LTA requires the highest S/N ratio of 2 (Fig. 3.7d). Since envelopes, STA/LTA, and kurtosis prevent destructive interference of noise by their lack of negative amplitudes, they can only improve S/N by constructive interference of signal. The detection thresholds observed after BPI are lower than is typical for a single trace due to successfully stacking weak signal. However, if individual pre-stack traces have S/N≤1, then signal cannot stack. BPI of raw seismograms detects signal smaller than noise by constructive interference of signal and destructive interference of noise. The theoretical improvement of $\sqrt{N}$, or a factor of ~11 from stacking 116 traces, is not achieved. This is likely because of other sources of error, such as coherent noise, the velocity model, non-uniform energy from the focal mechanism, and performing BPI which ignores amplitudes rather than RTM. Stacking of raw seismograms from an array much larger than AIDA, such as those routinely deployed by industry, could lower the detection threshold. Since the low threshold of kurtosis does not come primarily from stacking, only modest improvement is expected from a larger array.

3.6.5 Noise Bursts

Fig. 3.8a displays a 5-minute time window consisting of seismograms contaminated by large seismic noise. Some traces are noisy due to local human activities, such as farm machinery, and large noise bursts travel down the seismic lines as vehicles drive along the roads used for deployment. These data were blindly back-projected using each imaging method to test robustness. The maximum stack seismograms (Figs. 3.8b-e) show that the kurtosis method

provides one probable event detection while the other methods contain many false triggers created by the noise bursts.

To examine the probable event detected by the kurtosis method more closely, the raw seismograms and pre-processed traces were time shifted according to its hypocentral location (Fig. 3.9). The P-wave arrivals of a very small event are aligned, but the data in this short time window are still contaminated by large noise. The notable exception is the kurtosis processed traces, which show clear pre-stack signal on most traces and no large noise (Fig. 3.9d). Kurtosis is insensitive to amplitude, instead measuring a statistic of the amplitude distribution. The kurtosis pre-processing has drastically reduced noise energy, as the kurtosis of the noise bursts is between that of background noise and an impulsive source. The signal extracted by kurtosis is easily stacked and imaged by BPI (Figs. 3.8e, 3.9d and 3.10). In contrast, the other methods perform poorly due to their sensitivities to the large amplitude noise (Figs. 3.9a-c, Table 3.1). BPI of the raw seismograms and envelope detect a possible event at the correct time (arrows), but it is comparable to numerous false triggers. STA/LTA creates a strong signal at the sudden onset of noise bursts, and thus performs the worst (Fig. 3.9c). The magnitude of this event is estimated as about –0.7.

3.6.6 Velocity Model

We did not quantitatively assess the sensitivity of the four BPI methods to errors in the velocity model. However, such sensitivity and polarity are the two reasons that many studies pre-process the raw waveforms into the other three characteristic functions. The high spatial resolution of the raw waveform images comes with a tradeoff of the strongest sensitivity to

errors in the velocity model (Table 3.1). Detection is still possible if a subset of the traces align; this was observed for some of the AIDA events. The other three methods in the presence of velocity-model traveltime errors produce a smeared image with lower resolution and amplitude, presumably reducing the detection threshold. For all of the methods, once an event has been detected, residual traveltime errors can be used to correct the velocity model and improve the image, perhaps detecting additional events.

3.6.7 Magnitude Preservation

In addition to hypocenter locations and origin times, earthquake magnitudes provide important information to assess an earthquake cluster. To examine the capability of the four methods to preserve magnitude information, we considered 25 events whose duration magnitudes have been reported in an existing catalog (Wu et. al, 2015). Before imaging these earthquakes, we manually edited the seismograms to delete noise and corrected them for both polarity and geometric spreading. We do not delve into whether the P-wave arrivals at further offsets have lower frequencies associated with attenuation (Eisner et al, 2013) and neglect this effect because the epicentral region is relatively small and comprises a roughly homogeneous velocity structure consisting of low-attenuation crystalline rock (Davenport et al., 2015).

We assess the base-10 logarithm of the detection peak on BPI maximum stack seismograms as a proxy for magnitude. If this proxy is linearly related to the magnitude of larger events measured using traditional methods, then it can be scaled to obtain a good estimate for magnitude of the smaller events detected by BPI. For the four imaging methods, we investigate

whether such a correlation exists with the catalog of Wu et al. (2015). The back-projection magnitudes of both raw and envelope seismograms show a strong linear correlation with the catalog magnitudes (Figs. 3.11a and 3.11b, Table 3.1), as they directly measure the strength of ground shaking. Kurtosis is independent of amplitude, measuring instead the peakedness of the amplitude distribution. As expected, the back-projection image amplitude from kurtosis is insensitive to earthquake magnitudes (Fig. 3.11d). It decreases with signal-to-noise ratio at smaller magnitudes, where kurtosis measures a mix of signal and noise statistics. Despite STA/LTA being associated with energy, STA/LTA back-projection provides a poor correlation with magnitude (Fig. 3.11c). While STA should correlate with magnitude, LTA depends upon the noise energy, which varies with time. BPI of raw seismograms and envelopes enable an approximation to actual earthquake magnitudes without analysing individual seismograms (Table 3.1). However, this assumes that the data have been corrected for geometric spreading and polarity and noisy traces have been eliminated. BPI does not properly consider non-spherical geometric or intrinsic attenuation, so these magnitude estimates will have larger errors in more complex velocity models. RTM properly considers these effects, but is more computationally expensive.

3.7 Discussion

Table 3.1 synthesizes the results of the comparisons made in the previous section. We aim to identify a robust automated back projection process for a large volume of seismic data and a large hypocentral search volume. Our primary goal is to detect and locate events smaller than noise by stacking prior to detection to improve the signal to noise ratio. Other evaluation

criteria are robustness in the presence of large noise bursts, polarity reversals and velocity model errors, high spatial resolution of the source image, and magnitude preservation.

The most accurate and highest resolution imaging method in principle is RTM or BPI of the observed seismograms (Fig. 3.6, Table 3.1). It is capable of a significant improvement in signal-to-noise by stacking data from a large array, and is therefore capable of detecting and locating events smaller than the noise (Fig. 3.7, Table 3.1). This is the primary advantage of using back-projection as a detection method over traditional single-trace methods. However, BPI of raw seismograms is dependent upon correcting the polarity (Fig. 3.6a, Table 3.1), having an accurate velocity model, and overcoming large noise bursts (Figs. 3.8 and 3.9, Table 3.1). These are challenges for sparse arrays and for low signal-to-noise ratios. For these reasons, many workers have pre-processed the data to back-project the envelope, STA/LTA, or kurtosis. All of these methods eliminate sensitivity to polarity and reduce sensitivity to velocity model errors, but come at the expense of lower spatial resolution (Fig. 3.6, Table 3.1). The envelope and STA/LTA remain sensitive to large noise bursts, including aliased S and surface waves (Figs. 3.6, 3.8, and 3.9, Table 3.1). Both require detectability of the event in single traces so that stacking can improve the signal-to-noise ratio, and they are thus incapable of detecting events below noise (Fig. 3.7, Table 3.1). There is therefore only a minor benefit of event detection using BPI of envelopes or STA/LTA. Kurtosis, on the other hand, is robust in the presence of all types of noise and error (Figs. 3.8 and 3.10, Table 3.1). In addition, it is capable of detecting events in case of low S/N ratios, enabling stacking to further improve detection sensitivity (Fig. 3.7, Table 3.1). Kurtosis does not preserve magnitude information (Fig. 3.11, Table 3.1) and produces a lower resolution image (Fig. 3.6, Table 3.1). However, for detection, it performs similar to raw seismograms and in

the view of the fact that no other method rather than the kurtosis can achieve the robust detection in the presence of polarity, noise bursts, the success of the kurtosis in detection and location is remarkable.

A combined multi-pass method achieves all of our goals. The kurtosis-based BPI is the most robust method in the presence of real data issues, while BPI of raw seismograms provides the best spatial resolution and preserves magnitudes. Both benefit from stacking to detect small events that can not be detected on a single seismogram. We conclude that the optimum strategy to achieve the most robust detection and highest-quality event catalog is to use the kurtosis-based back-projection to detect and locate earthquake sources within a large volume of continuous seismic data and a large hypocentral search volume. Subsequently, using the kurtosis hypocenters as prior knowledge, BPI of raw seismograms within constrained time zones and search volumes can be used to enhance spatial resolution and to obtain the magnitude. The computational effort of the second pass is orders of magnitude smaller than the original detection. Thus extra effort can be applied to remove noisy traces, correct polarity, and improve the velocity model. These extra efforts are computationally expensive if applied to the entire 4D search volume, but are practical with pre-detected hypocenters. They are routinely applied when back-projecting a single large earthquake (e.g., Ishii et al., 2005, 2007).

The spatial resolution of backprojection can be improved by using both P- and S-waves (e.g., Kiser et al., 2011; Vlcek et al., 2015). It is also possible to lower the BPI detection threshold by stacking the larger S-waves. The backprojection of S-waves provides a better spatial resolution than P-waves at a given frequency due to a shorter wavelength. Correcting

S-wave polarities is still necessary for the backprojection of raw seismograms and is more challenging, especially on vertical geophones. The STA/LTA and kurtosis windows would need to be tuned to emphasize the S waves. The joint backprojection of P- and S-waves requires not just accurate P and S velocity, but also an accurate velocity ratio so the images co-locate (e.g., Kiser et al., 2011). Back-projection of the S-waves for larger AIDA events produced a slightly better spatial resolution, but the image was displaced from that of the P-waves. The two images were within absolute errors of each other, but not within relative errors due to different small errors on the two velocity models. Additional velocity analysis to co-locate the BPI images could be performed to achieve hypocenters with higher spatial resolution but has not been performed for this study.

The kurtosis waveforms of the first 48 hours of the continuous AIDA dataset were blindly back-projected for a search volume of 12 km x 12 km x 9 km spanning the primary aftershock region covered by the AIDA array. For AIDA, a 50-m grid provided optimum spatial resolution for imaging from raw seismograms, but 100 m spacing was used for kurtosis-based event detection, saving a factor of 8 in computation time. The detection on the maximum stack seismogram (e.g,. right column of Figs. 3.6 and 3.10) used a constant threshold. The back projection hypocenters were compared to hypocenters obtained from a careful analysis of data from a co-located traditional array with ~5 km average station spacing (Wu et al., 2015) (Fig. 3.12). The automated kurtosis-based back projection successfully recovered 100% of the traditionally detected events that occurred in the same time window and search volume, as well as detected and located ~570 additional events, improving the completeness of the earthquake catalog. This corresponds to an improved detection and location efficiency of about an factor of 7 more events, moving the detection threshold ~0.8 lower in

magnitude. The spatial pattern of the additional small earthquakes detected by dense-array back-projection is similar to that of the traditional network (Fig. 3.12), but better delineate the complexity of the fault zone. Inclusion of smaller events enables a more detailed investigation of stress propagation and strain release during the aftershock sequence. Back projection of the full AIDA dataset and analysis of the aftershock sequence are presented in Chapter 4.

Computational efficiency also needs to be considered for an automated migration for large, continuous data volumes. Fortunately, the BPI algorithm is embarrassingly parallel, and therefore a parallel version of the algorithm was implemented the using slice-level partition in depth. Using modern computers, BPI of the AIDA data (1,296,000 potential hypocentral grid points) using one CPU for each slice takes 3 times the length of the data time window. Oct-tree approaches may be preferred to increase the computation efficiency (Vlček et al., 2015) by using an initial coarser search grid for detection triggering and zooming to detected hypocenters. However, the initial grid partition must be optimized with care so as not to miss events between grid points.

One of the great successes of BPI has been the ability to resolve energy release as a function of time and space (e.g., Ishii et al., 2005, 2007, Kiser and Ishii, 2012; Koper et al., 2012). This has provided great insights into rupture processes without the uniqueness issues inherent from inversions based upon sparse stations. Combining multiple arrays and/or additional phases such as the S wave have increased the spatial resolution (e.g., Kiser et al., 2011; Koper et al., 2012; Kiser and Ishii, 2012, Vlček et al., 2015). Unfortunately, the largest events recorded by AIDA had magnitude 2.5-3.6 (Wu et al., 2015) and had generally high

stress drops (Wu et al., submitted). The size of the expected slip patch is therefore 50-200 m, similar to the size of the BPI point-source image. On the other hand, the shooting star artefact on fault planes must also be considered. We have been unable to image rupture propagation from the AIDA data, but the evidence suggests we came close to the required resolution. If a larger earthquake had occurred or if AIDA had deployed stations more closely and at higher temporal sampling, rupture propagation could have been imaged.

Finally, we wish to emphasize that we do not consider AIDA to be an ideal deployment. Industry hydraulic fracturing studies are routinely deploying an order of magnitude more sensors (e.g., Anikiev et al., 2014, Vlček et al., 2015). The aperture of AIDA was limited but successfully recorded the majority of the main aftershock zone because it was spatially small. However, AIDA failed to image triggered off-fault seismicity to the northeast that was discovered by the larger-aperture traditional network (Wu et al., 2015).

Gaps between the array arms, station spacing, and temporal sampling all limited the spatial resolution of the images. In a more complex geology and velocity model, denser spacing and larger aperture might be required to improve the velocity model. We advocate larger arrays, with both denser spacing and larger aperture, and recording at a much higher temporal sampling rate. With such an array, BPI has the potential to detect and locate events so small they cannot be observed in the non-stacked array data. Expanding the earthquake catalog to smaller magnitudes would enable improved testing of mechanisms of stress transfer and strain release.

3.8 Conclusions

The performances of back projection imaging with four previously-used preprocessing methods were examined to identify a robust strategy to automatically migrate large volumes of data. The primary goal was to automatically detect smaller earthquakes than traditional methods, utilizing stacking to improve the signal to noise ratio prior to detection. For evaluation, the four imaging methods were applied to the aftershock sequence of the 2011 Virginia earthquake as densely recorded by the AIDA array. The dataset comprises highly variable signal to noise, spatially aliased noise, large noise bursts, and variable signal polarity: realistic issues in many environments. Back-projection of kurtosis waveforms was the most robust at detecting the smallest-magnitude events. Back-projection of raw waveforms produced the best spatial resolution and preserved magnitude. Therefore, we suggest a two-phase back-projection imaging process: 1- back projection of kurtosis gradient waveforms for event detection and location within large data volumes and large hypocentral search volumes, 2- back projection of raw seismograms of the previously detected events to improve the location accuracy of the hypocenters and to obtain earthquake magnitudes. Automated kurtosis-based back projection of the AIDA data demonstrated detection and location of significantly more and smaller events than previous work based on a sparse array and traditional detection to smaller magnitudes. The results highlight that dense arrays and back projection imaging are capable of producing a more complete earthquake catalog, which will enable a better understanding of stress and strain evolution, earthquake triggering, earthquake mechanisms, and how these processes scale to very small magnitude.

References

Adler, F., Baina, R., Soudani, M. A., Cardon, P., & Richard, J. B., 2008. Nonlinear 3D tomographic least-squares inversion of residual moveout in Kirchhoff prestack-depth-migration common-image gathers. Geophysics, **73**, 5, VE13-VE23.

Allen, R. V., 1978. Automatic earthquake recognition and timing from single traces. *Bulletin of the Seismological Society of America*, **68**, 1521–1532.

Anderson, R. G., & McMechan, G. A., 1989. Automatic editing of noisy seismic data. *Geophysical Prospecting*, **37**, 8, 875–892.

Anikiev, D., Valenta, J., Stanek, F., & Eisner, L., 2014. Joint location and source mechanism inversion of microseismic events: benchmarking on seismicity induced by hydraulic fracturing. *Geophysical Journal International*, **198**, 1, 249–258.

Artman, B., Podladtchikov, I., & Witten, B., 2010. Source location using time-reverse imaging. *Geophysical Prospecting*, **58**, 5, 861–873.

Baer, M. & Kradolfer, U., 1987. An automatic phase picker for local and teleseismic events. *Bull. seism. Soc. Am.*, **77**, 1437–1445.

Baysal, E., Kosloff, D., & Sherwood, J., 1983. Reverse time migration. *Geophysics*, **48**, 11, 1514–1524, doi : 10:1190/1:1441434.

Ben-Zion, Y., Vernon, F. L., Ozakin, Y., Zigone, D., Ross, Z. E., Meng, H., & Barklage, M., 2015. Basic data features and results from a spatially dense seismic array on the San Jacinto

fault zone. *Geophysical Journal International*, **202**, 1, 370–380.

Chang, W. F., & McMechan, G. A., 1991. Wavefield extrapolation of body waves for 3-D imaging of earthquake sources. *Geophysical Journal International*, **106**, 1, 85–98.

Chang, W. F., & McMechan, G. A., 1987. Elastic reverse-time migration. *Geophysics*, **52**, 10, 1365–1375.

Chambers, K., Dando, B. D. E., Jones, G.A., Velasco, R. & Wilson, S.A. 2014. Moment tensor migration imaging. *Geophysical Prospecting*, **62**, 4, 879–896.

Chambers, K., Kendall, J., BrandsbergDahl, S., & Rueda, J., 2010. Testing the ability of surface arrays to monitor microseismic activity. *Geophysical Prospecting*, **58**, 5, 821–830.

D'Amico, S., Koper, K. D., Herrmann, R. B., Akinci, A., & Malagnini, L., 2010. Imaging the rupture of the Mw 6.3 April 6, 2009. L'Aquila, Italy earthquake using back-projection of teleseismic P-waves. *Geophysical Research Letters*, **37**, 3.

Chapman, M. C., 2013. On the rupture process of the 23 August 2011 Virginia earthquake. *Bull. Seismol. Soc. Am.*, **103**, 613–628.

Davenport, K. K., Hole, J. A., Quiros, D. A., Brown, L. D., Chapman, M. C., Han, L., & Mooney, W. D., 2015. Aftershock imaging using a dense seismometer array (AIDA) after the 2011 Mineral, Virginia earthquake, in The 2011 Mineral, Virginia, Earthquake and Its Significance for Seismic Hazards in Eastern North America, J.W. Horton Jr.,M. C. Chapman, & R. A. Green (Editors). *Geological Society of America Special Papers*, **509**, 273–283.

Drew, J., Zhang, J., & Le Calves, J., 2014. The impact of channel count on microseismic event detection for a surface array. *84th SEG meeting*, Denver, USA, Expanded Abstracts, 2183–2187.

Drew J., Leslie D., Armstrong P. & Michaud G., 2005. Automated microseismic event detection and location by continuous spatial mapping. *2005 SPE Annual Technical Conference and Exhibition*, Dallas, USA, SPE95513.

Eisner, L., Gei, D., Hallo, M., Opršal, I. & Ali, M., 2013. The peak frequency of direct waves for microseismic events. *Geophysics*, **78**, 6, A45– A49.

Eisner, L., Abbott, D., Barker, W. B., Lakings, J., & Thornton, M. P., 2008. Noise suppression for detection and location of microseismic events using a matched filter. *In SEG Technical Program Expanded Abstracts 2008*, 1431–1435. Society of Exploration Geophysicists.

Embree, P. 1968, Diversity seismic record stacking method and system. *U.S. Patent*, No.3, 398,396.

Forghani-Arani, F., Behura, J., Haines, S. S., & Batzle, M., 2013. An automated crosscorrelation based event detection technique and its application to a surface passive data set. *Geophysical Prospecting*, **61**, 4, 778–787.

Gajewski, D., & Tessmer, E., 2005. Reverse modelling for seismic event characterization. *Geophysical Journal International*, **163**, 1, 276–284.

Gharti, H. N., Oye, V., Kühn, D. & Zhao, P., 2011. Simultaneous microearthquake location

and moment-tensor estimation using timereversal imaging. *81st SEG meeting*, San Antonio, USA, 1632–1637.

Gharti, H. N., Oye, V., Roth, M. & Kühn, D., 2010. Automated microearthquake location using envelope stacking and robust global optimization. *Geophysics*, **75**, 4, MA27–MA46.

Grigoli, F., Cesca, S., Amoroso, O., Emolo, A., Zollo, A., & Dahm, T., 2014. Automated seismic event location by waveform coherence analysis. *Geophysical Journal International*, **196**, 1742–1753.

Grigoli, F., Cesca, S., Vassallo, M., & Dahm, T., 2013. Automated seismic event location by travel-time stacking: An application to mining induced seismicity. *Seismological Research Letters*, **84**, 666–677.

Haney, M. M., 2014. Backprojection of volcanic tremor. *Geophysical Research Letters*, **41**, 6, 1923–1928.

Hansen, S. M., & Schmandt, B., 2015. Automated detection and location of microseismicity at Mount St. Helens with a largeN geophone array. *Geophysical Research Letters*, **42**, 18, 7390–7397.

Hole, J. A., Wang, K., Davenport, K. K., Chapman, M. C., Beskardes, G. D., Quiros, D. A., Brown, L. D., & Mooney, W. D., 2014. Back-Projection Imaging of Aftershocks Recorded by the Dense AIDA Array After the 2011 Virginia Earthquake (abstract). Seismol. Res. Lett., **85**, 2, 434.

Inbal, A., Clayton, R. W., & Ampuero, J. P., 2015. Imaging widespread seismicity at

midlower crustal depths beneath Long Beach, CA, with a dense seismic array: Evidence for a depthdependent earthquake size distribution. *Geophysical Research Letters*, **42**, 15, 6314–6323.

Ishii, M., Shearer, P. M., Houston, H. & Vidale, J. E., 2005. Extent, duration and speed of the 2004 SumatraAndaman earthquake imaged by the Hi-Net array. *Nature*, **435**, 7044, 933–936.

Ishii, M., Shearer, P. M., Houston, H., & Vidale, J. E., 2007. Teleseismic P wave imaging of the 26 December 2004 SumatraAndaman and 28 March 2005 Sumatra earthquake ruptures using the Hinet array. *Journal of Geophysical Research: Solid Earth*, **112**, B11.

Kao, H., & Shan, S., 2004. The source-scanning algorithm: mapping the distribution of seismic sources in time and space. *Geophysical Journal International*, **157**, 589–594.

Kiser, E., Ishii, M., Langmuir, C. H., Shearer, P. M., & Hirose, H., 2011. Insights into the mechanism of intermediate-depth earthquakes from source properties as imaged by back projection of multiple seismic phases. *Journal of Geophysical Research: Solid Earth*, **116**, B6.

Kiser, E., & Ishii, M., 2012. The March 11, 2011 Tohoku-oki earthquake and cascading failure of the plate interface. *Geophysical Research Letters*, **39**, 7.

Koper, K. D., Hutko, A. R., Lay, T., & Sufri, O., 2012. Imaging short-period seismic radiation from the 27 February 2010 Chile (Mw 8.8) earthquake by back-projection of P, PP, and PKIKP waves. *Journal of Geophysical Research: Solid Earth*, **117**, no.B2.

Kosloff, D. D., & Baysal, E., 1983. Migration with the full acoustic wave equation. *Geophysics*. **48**, 6, 677–687.

Kuperkoch, L., Meier, T., Lee, J., Friederich, W., & EGELADOS Working Group, 2010. Automated determination of P-phase arrival times at regional and local distances using higher order statistics. *Geophysical Journal International*, **181**, 1159–1170.

Langet, N., Maggi, A., Michelini, A., & Brenguier, F., 2014. Continuous Kurtosisbased migration for seismic event detection and location, with application to Piton de la Fournaise Volcano, La Runion. *Bulletin of the Seismological Society of America*, **104**, 1, 229–246.

Levin, S. A., 1984. Principle of reverse-time migration. *Geophysics*, **49**, 5, 581–583.

Loewenthal, D., & Mufti, I. R., 1983. Reversed time migration in spatial frequency domain. *Geophysics*, **48**, 5, 627–635.

McMechan, G. A., Wen, J., & Morales, J. A., 1988. 3-D acoustic modelling and imaging for earthquake data. *Geophysical Journal International*, **92**, 2, 339–344.

McMechan, G. A., Luetgert, J. H., & Mooney, W. D., 1985, Imaging of earthquake sources in Long Valley Caldera, California, 1983. *Bulletin of the Seismological Society of America*, **75**, 4, 1005–1020.

McMechan, G. A., 1983. Migration by extrapolation of time dependent boundary values. *Geophysical Prospecting*, **31**, 413–420.

McMechan, George A., 1982. Determination of source parameters by wavefield extrapolation.

Geophysical Journal International, **71**, 3, 613–628.

McNamara, D. E., Benz, H. M., Herrmann, R. B., Bergman, E. A., Earle, P., Meltzer, A., Withers, M., & Chapman, M., 2014. The Mw 5.8 Mineral, Virginia, earthquake of August 2011 and aftershock sequence: Constraints on earthquake source parameters and fault geometry. *Bull. Seismol. Soc. Am.*, **104**, 40–54.

Michaud, G., & Leaney, S., 2008. Continuous microseismic mapping for real-time event detection and location. *SEG Technical Program Expanded Abstracts 2008*. Society of Exploration Geophysicists, 1357–1361.

Miyazawa, M., Venkataraman, A., Snieder, R., & Payne, M. A., 2008. Analysis of microearthquake data at Cold Lake and its applications to reservoir monitoring. *Geophysics*, **73**, 3, O15–O21.

Neidell, N. S., & Taner, M. T., 1971. Semblance and other coherency measures for multichannel data. *Geophysics*, **36**, 3, 482–497.

Nippress, S. E. J., Rietbrock, A., & Heath, A.E., 2010. Optimized automatic pickers: application to the ANCORP data set. *Geophysical Journal International*, **181**, 911–925.

Quiros, D. A., Brown, L. D., Davenport, K. K., Hole, J. A., Cabolova, A., Chen, C., Han, L., Chapman, M. C., & Mooney, W. (in press). Reflection imaging with earthquake sources and dense arrays. *Journal of Geophysical Research (Solid Earth)*. doi:10.1002/2016JB013677

Rietbrock, A. & Scherbaum, F., 1994. Acoustic imaging of earthquake sources from the Chalfant Valley, 1986, aftershock series. *Geophysical Journal International*, **119**, 1, 260–

268.

Ross, Z. E., & Ben-Zion, Y., 2014. Automatic picking of direct P, S seismic phases and fault zone head waves. *Geophysical Journal International*, **199**, no. 1, 368–381.

Saragiotis, C., Hadjileontiadis, L. & Panas, S., 2002. PAI-S/K: a robust automatic seismic P phase arrival identification scheme. *IEEE Trans. Geosci. Remote Sens.*, **40**, 1395–1404.

Spanos, A., 1999. Probability theory and statistical inference: econometric modeling with observational data. *Cambridge University Press*, 117–124.

Trnkoczy, A., 1998. Understanding & setting sta/lta trigger algorithm parameters for the k2. Appl Note, 41, 16–20.

Trojanowski, J., & Eisner, L., 2016. Comparison of migrationbased location and detection methods for microseismic events. *Geophysical Prospecting*, **65**, 1, 47–63.

Usher, P. J., Angus, D. A.,& Verdon, J. P., 2013. Influence of a velocity model and source frequency on microseismic waveforms: some implications for microseismic locations. *Geophysical Prospecting*, **61**, s1, 334–345.

Vlček, J., Fischer, T., & Vilhelm, J., 2015. Backprojection stacking of Pand Swaves to determine location and focal mechanism of microseismic events recorded by a surface array. *Geophysical Prospecting*, **64**, 6, 1428–1440.

Walker, K. T., & Shearer, P.M., 2009. Illuminating the nearsonic rupture velocities of the intracontinental Kokoxili Mw 7.8 and Denali fault Mw 7.9 strikeslip earthquakes with global

P wave back projection imaging.. *Journal of Geophysical Research: Solid Earth*, **114**, B2.

Withers, M., Aster, R., Young, C., Beiriger, J., Harris, M., Moore, S., & Trujillo, J., 1998. A comparison of select trigger algorithms for automated global seismic phase and event detection. *Bulletin of the Seismological Society of America*, **88**, 95–106.

Whitmore, N. D., 1983. Iterative depth migration by backward time propagation. *In SEG Technical Program Expanded Abstracts 1983*, 382–385. Society of Exploration Geophysicists.

Wu, Q., Chapman, M. C., & Beale, J. N., 2015. The aftershock sequence of the 2011 Mineral, Virginia, earthquake: Temporal and spatial distribution, focal mechanisms, regional stress, and the role of Coulomb stress transfer. *Bulletin of the Seismological Society of America*, **105**, 5, 2521–2537.

Wu, Q. & Chapman, M.C., 2017. Stress Drop Estimates and Source Scaling of the 2011 Mineral, Virginia Mainshock and Aftershocks (Submitted to *Bull. Seismol. Soc. Am.*).

Xu, X., Wen, X., Yu, G., Chen, G., Klinger, Y., Hubbard, J., & Shaw, J., 2009. Coseismic reverse- and oblique-slip surface faulting generated by the 2008 Mw 7.9 Wenchuan earthquake, China. *Geology*, **37**, 6, 515–518.

Zhebel, O., & Eisner, L., 2012. Simultaneous microseismic event localization and source mechanism determination. *82nd SEG meeting*, Expanded Abstracts, 1–5.

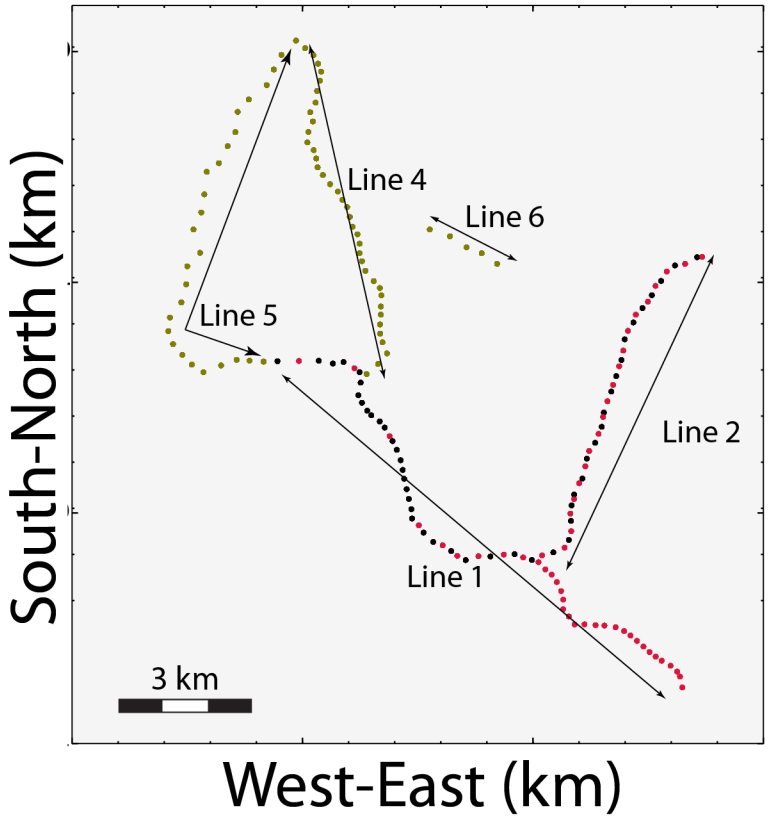

Figure 3.1: The Virginia aftershock AIDA array for the first (red) and the second (green) week. Black dots denote the common stations for both deployment phases.

Table 3.1: Summary of the performances of preprocessing methods.

Evaluation Criteria	**Raw**	**Envelope**	**STA/LTA**	**Kurtosis**
High spatial resolution	best	worst	good	fair
Detection & location of tiny events				
-Low signal-to-noise ratio	best	poor	worst	best
Robustness				
-Large S-waves (spatially aliased)	sensitive	sensitive	robust	robust
-Polarity (focal mechanism)	sensitive	robust	robust	robust
-Noise bursts	sensitive	sensitive	sensitive	robust
Magnitude preservation	good	good	poor	none
Sensitivity to velocity errors	high	low	low	low

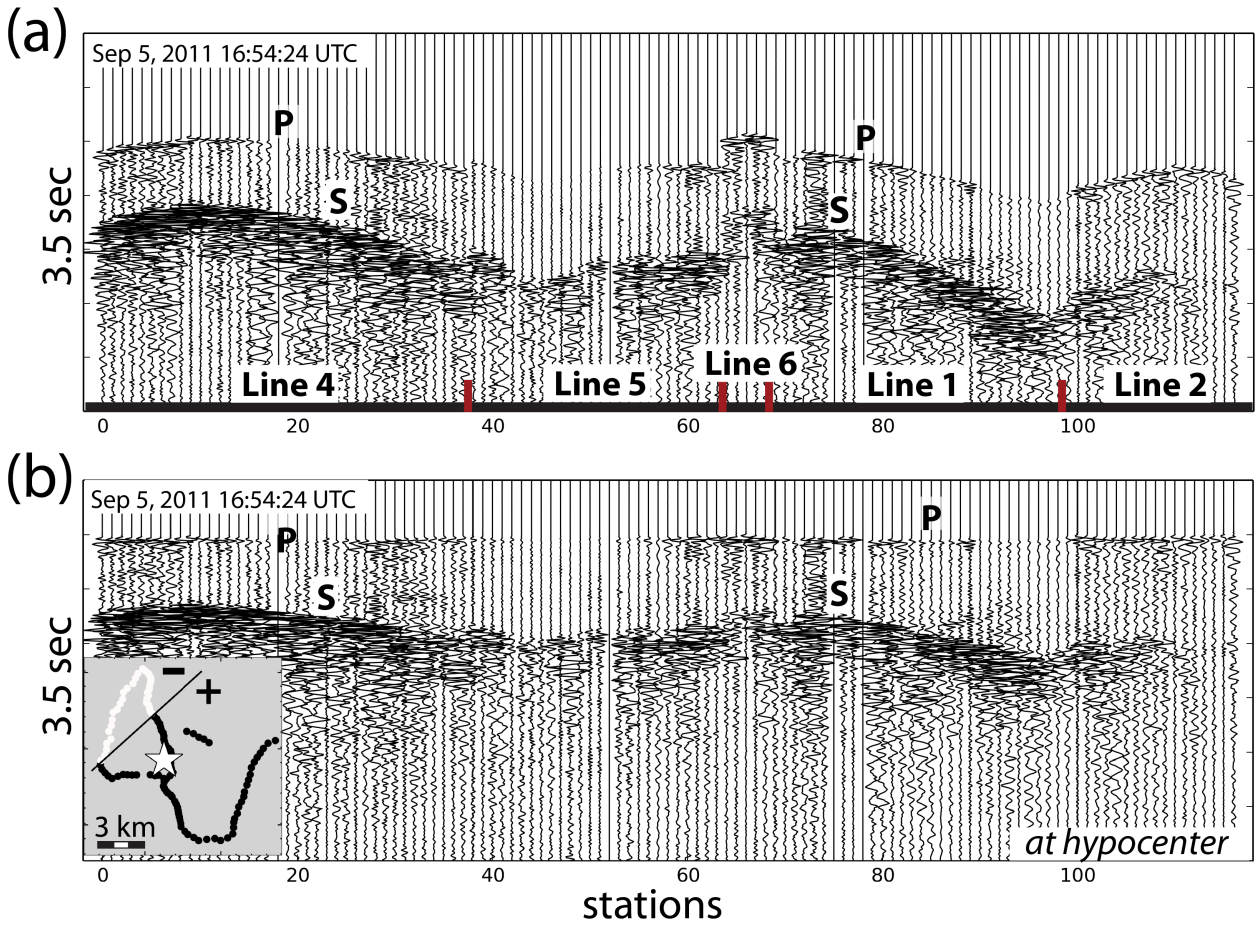

Figure 3.2: (a) An aftershock of magnitude 2.5 recorded by the AIDA array during the second week. Seismograms are sorted along the lines (Fig. 3.1). True relative amplitudes are shown after removal of the trace mean. (b) Seismograms from (a) shifted by the hypocenter-to-station time corresponding with the hypocenter derived by P-wave BPI. P-waves are horizontally aligned, but S-waves are not. Map of up (black) and down (white) first P-wave motion and corresponding focal plane at the surface. Star indicates epicenter of the event at 5.5 km depth.

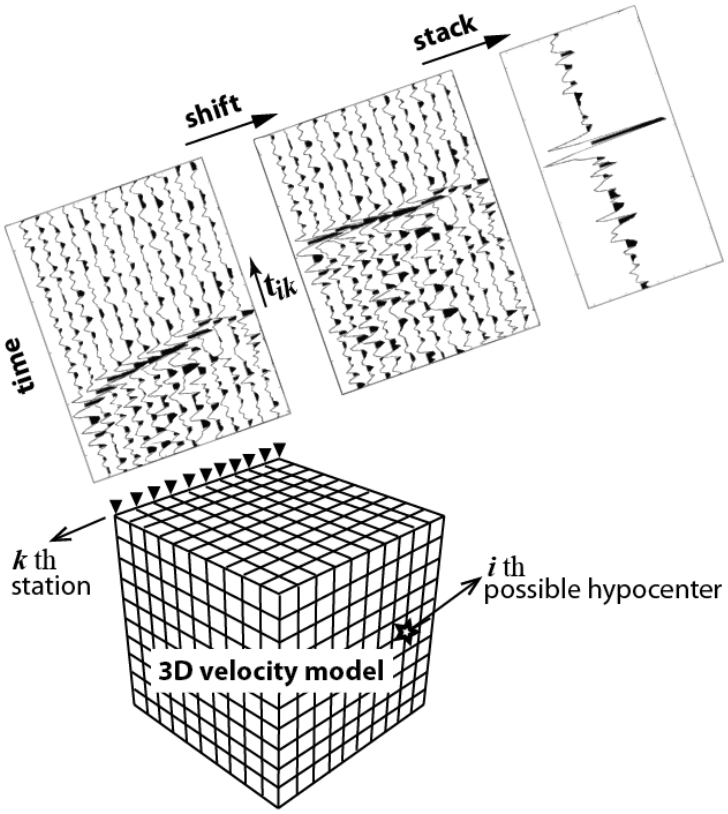

Figure 3.3: Illustration of the back-projection imaging method. Refer to text.

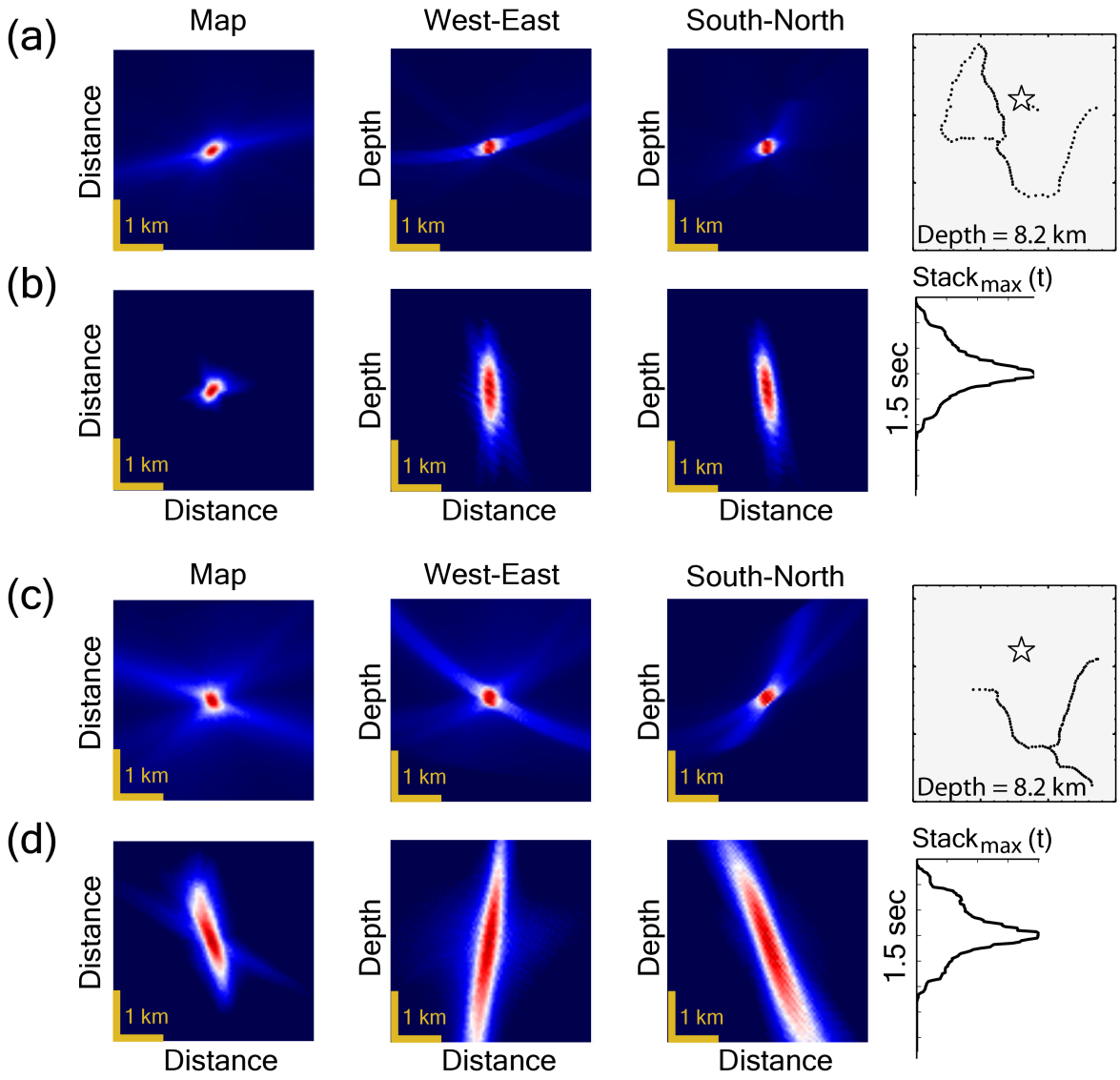

Figure 3.4: BPI images of a synthetic P-wave point source, bandpassed to <45 Hz to represent the Nyquist frequency of the AIDA data, computed using the AIDA week 2 array geometry. Rather than plotting cross-sections through the 3D volume, maximum stacked energy is projected through the stack volume onto 2D sections. (a) Projections from the 3D volume at the earthquake time onto 2D slices. Earthquake time is defined as time of the peak image magnitude. Right-hand panel shows the hypocenter (star) on the map. b) Projection of the 4D volume to 2D slices, adding through time and the shooting star tradeoff between earthquake time and distance from the array. Right-hand panel shows the maximum stack value anywhere within the 3D volume as a function of time; this trace is used for event detection. (c) and (d) shows projections from the 3D volume at the earthquake time onto 2D slice and projection of the 4D volume to 2D slices adding through time obtained from the AIDAs first-week array. The shooting star points in a different direction, and migration smearing artefacts are different, illustrating the effects of array location and aperture.

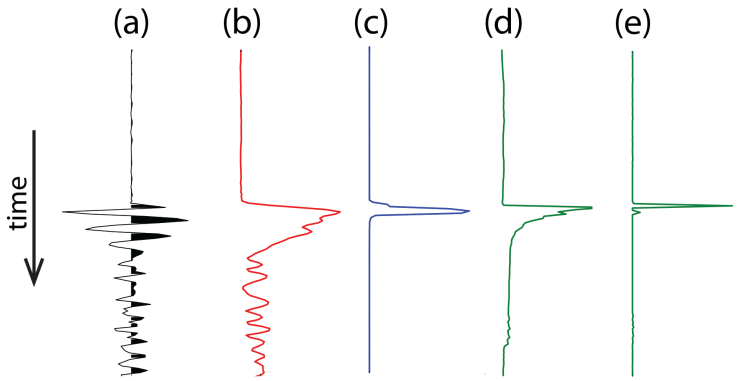

Figure 3.5: (a) Raw AIDA seismogram for an earthquake with strong signal. (b) envelope. (c) STA/LTA. (d) kurtosis. (e) positive gradient of the kurtosis.

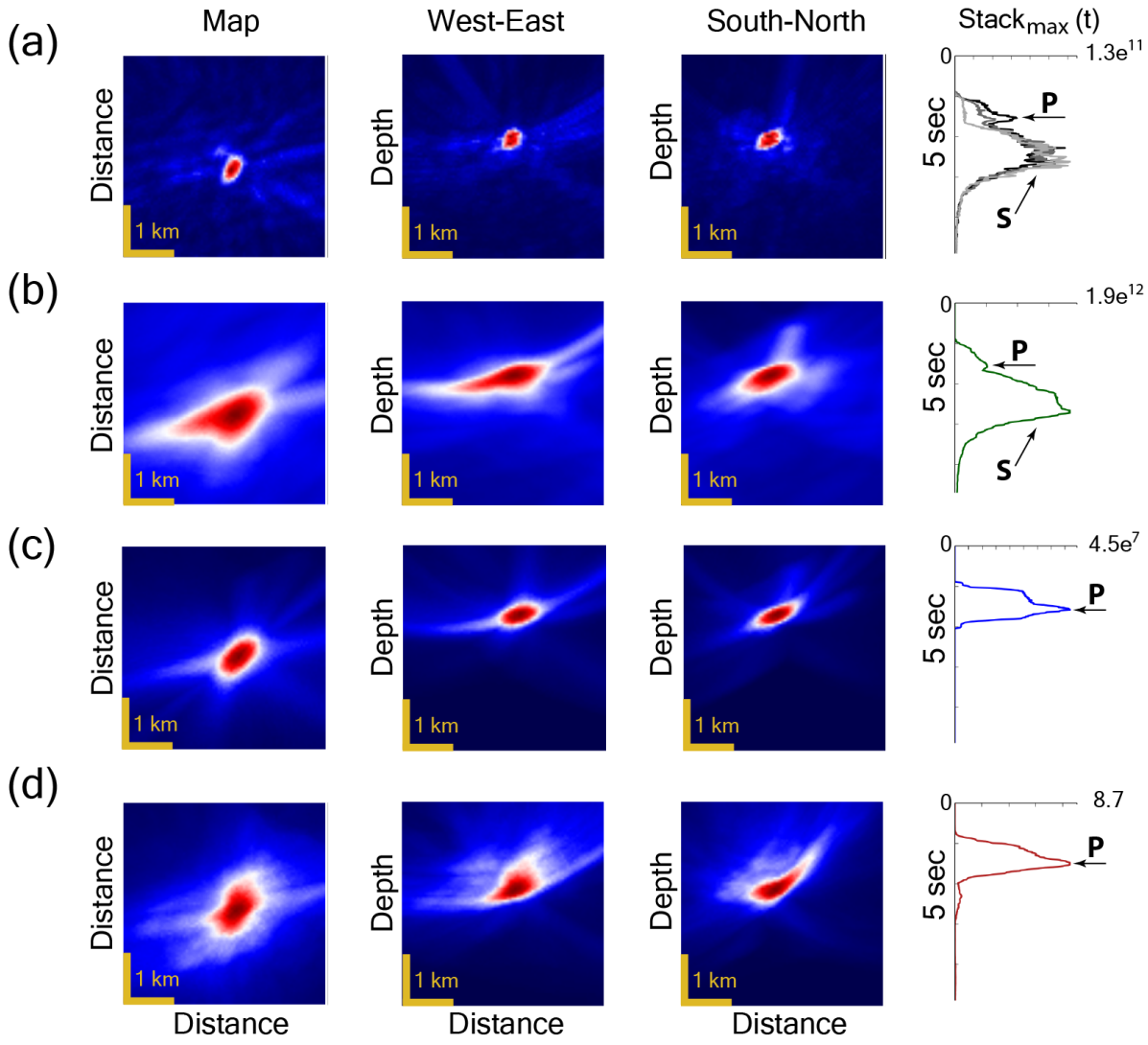

Figure 3.6: Back-projection imaging of the aftershock in Fig. 3.2 using a) raw seismograms, b) envelopes, c) STA/LTA and d) positive kurtosis gradient. The images are plotted at the best hypocenter time, projected onto each plane, plus a panel for the normalized maximum stack value as a function of time, all plotted the same as Fig. 3.4a. Figure (a) shows the maximum stack seismograms resulting from three different polarity distributions: consistent polarity (black), 30-70% mixed polarity (dark gray) and 50-50% (randomized) polarity (light gray).

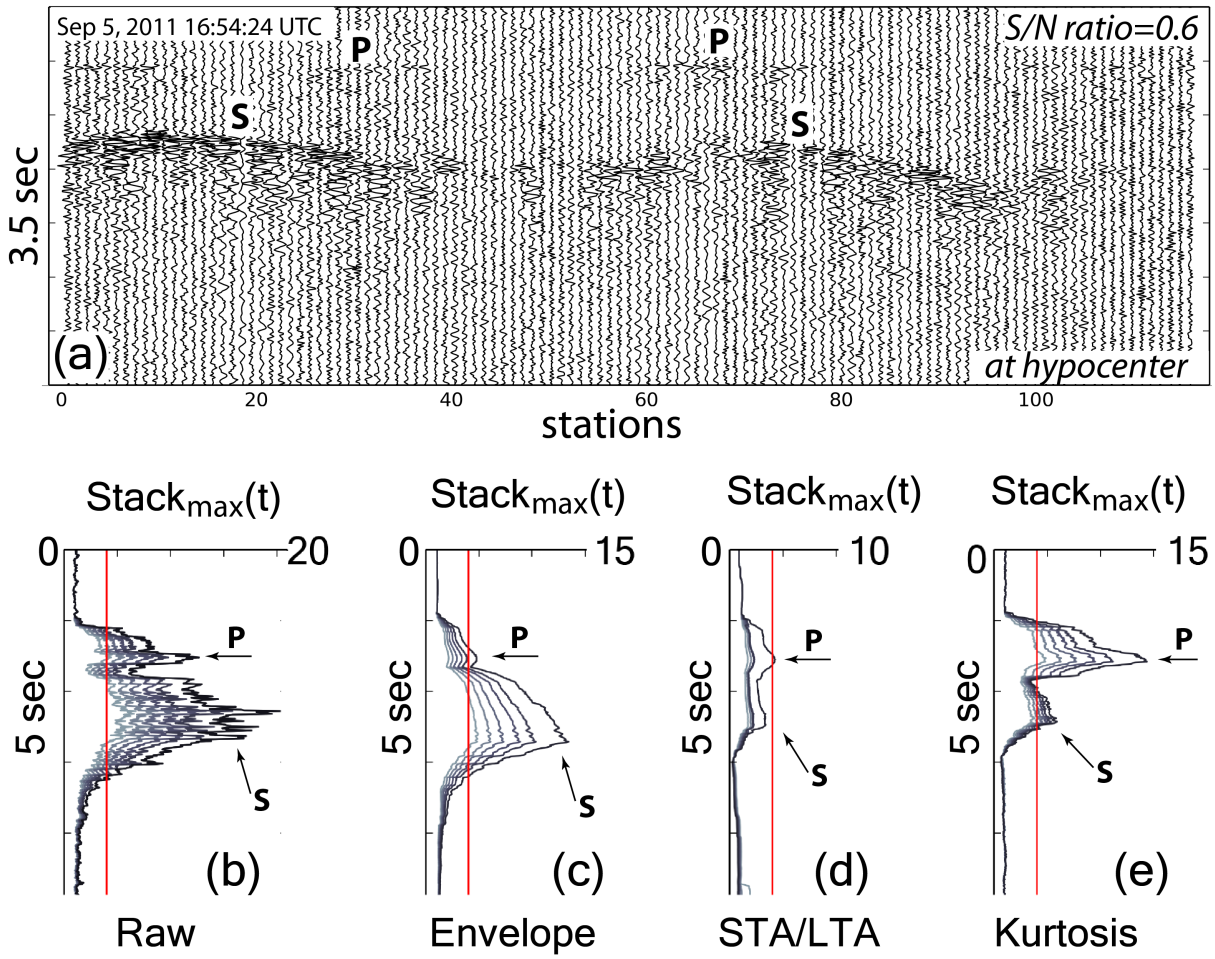

Figure 3.7: (a) Seismograms time corrected traces in Fig. 3.2b with S/N ratio of 0.6. Random noise extracted from the data were normalized and added to Fig. 3.2 at S/N of 0.6, 0.8, 1, 1.25, 1.5 and 2. The signal was corrected for spherical divergence after adding the noise. (b-e) BPI maximum energy seismograms for different signal-to-noise ratios. The traces are normalized by their noise. As noise increases, the ability to detect the P arrival deteriorates.

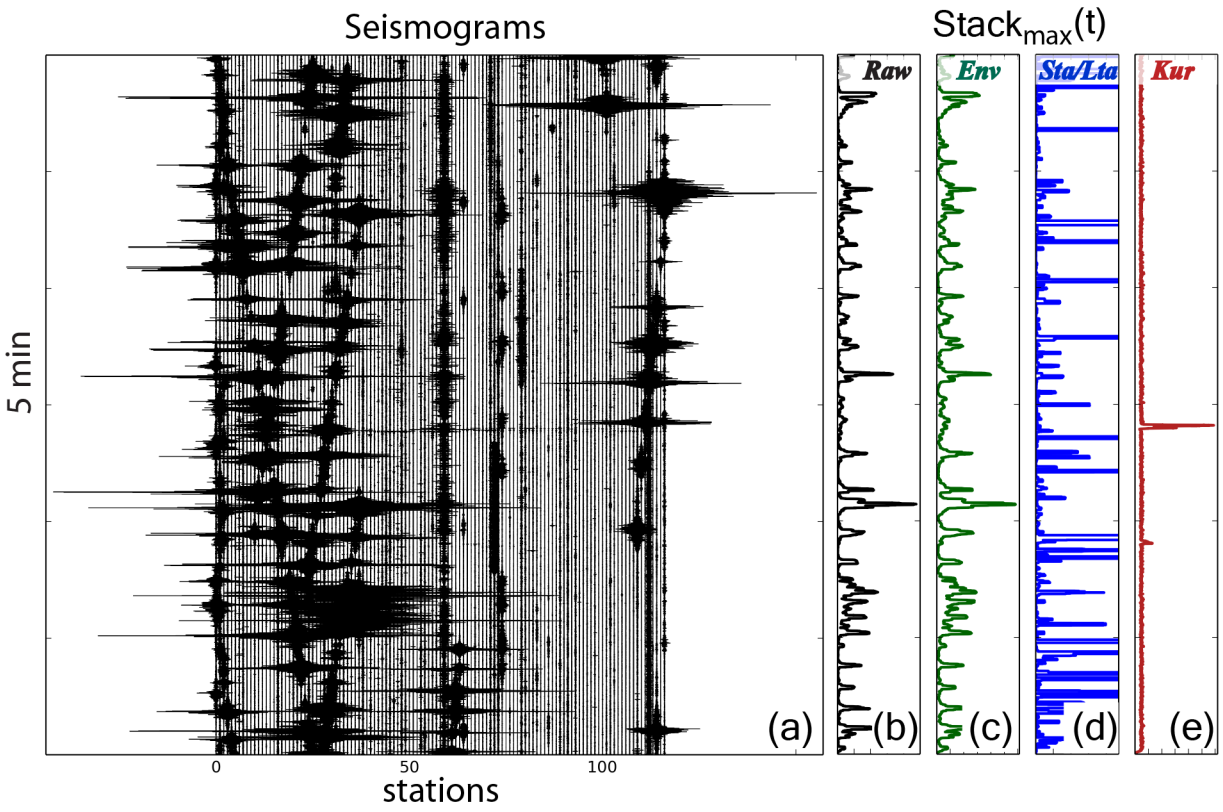

Figure 3.8: (a) AIDA data with large noise bursts and low S/N ratio. The BPI maximum stack energy seismograms using (b) raw seismograms, (c) envelopes, (d) STA/LTA and (e) kurtosis.

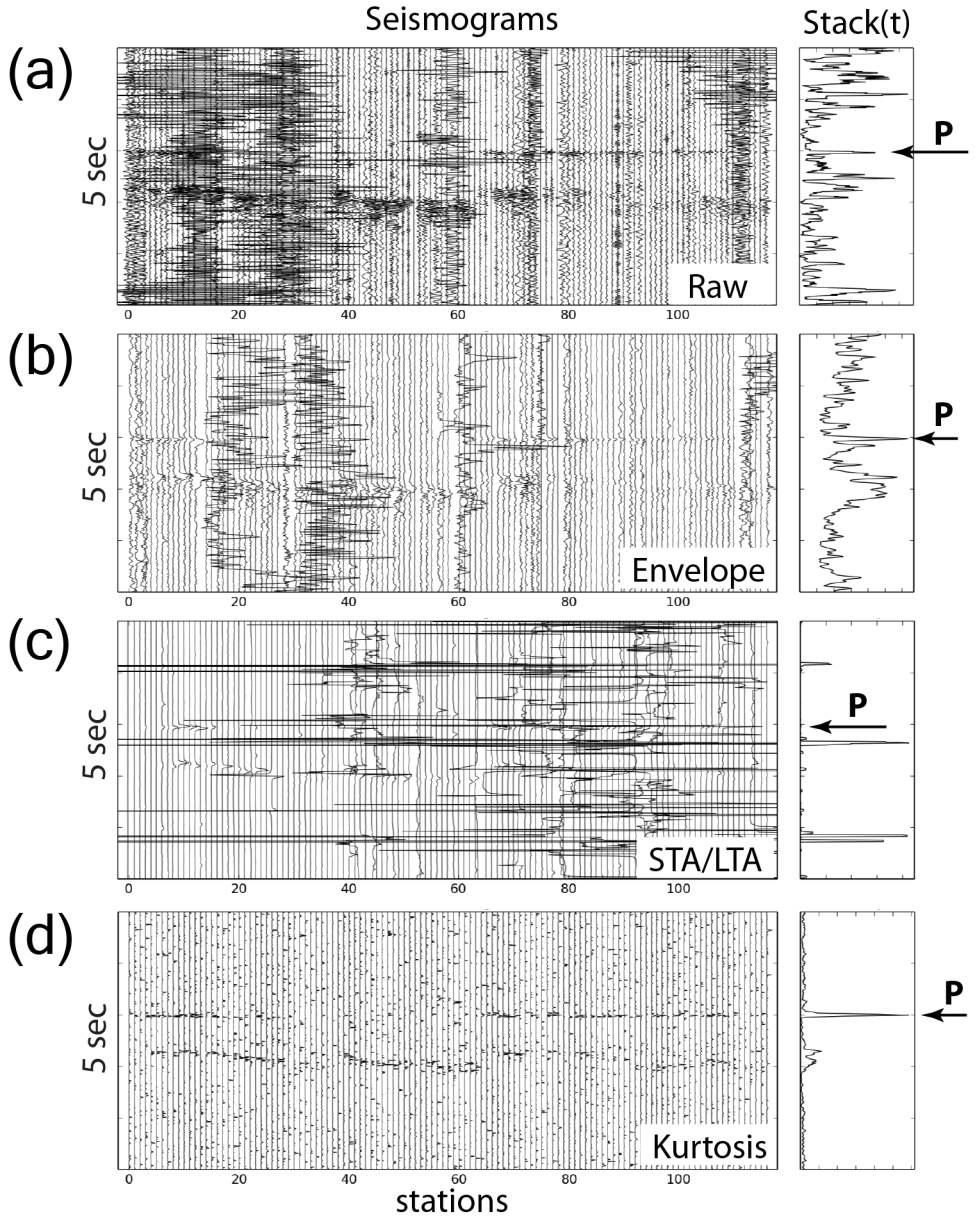

Figure 3.9: A closer look at the event detected by kurtosis BPI in Fig. 3.8, shifted in time corresponding to the hypocenter. (a) Raw seismograms, (b) envelopes, (c) STA/LTA and (d) kurtosis. Corresponding maximum stack energy traces are shown at right. Black arrows show the earthquake time.

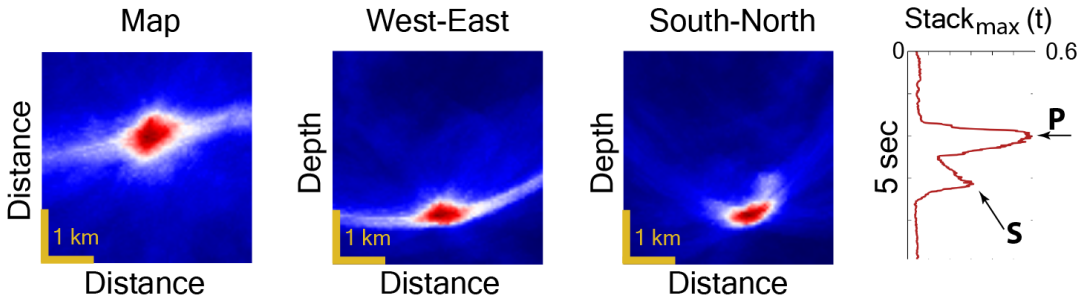

Figure 3.10: Back-projection of kurtosis for the small event of Figs. 3.8 and 3.9, plotted as for Fig. 3.6. Right-hand panel shows the normalized maximum stack value as a function of time.

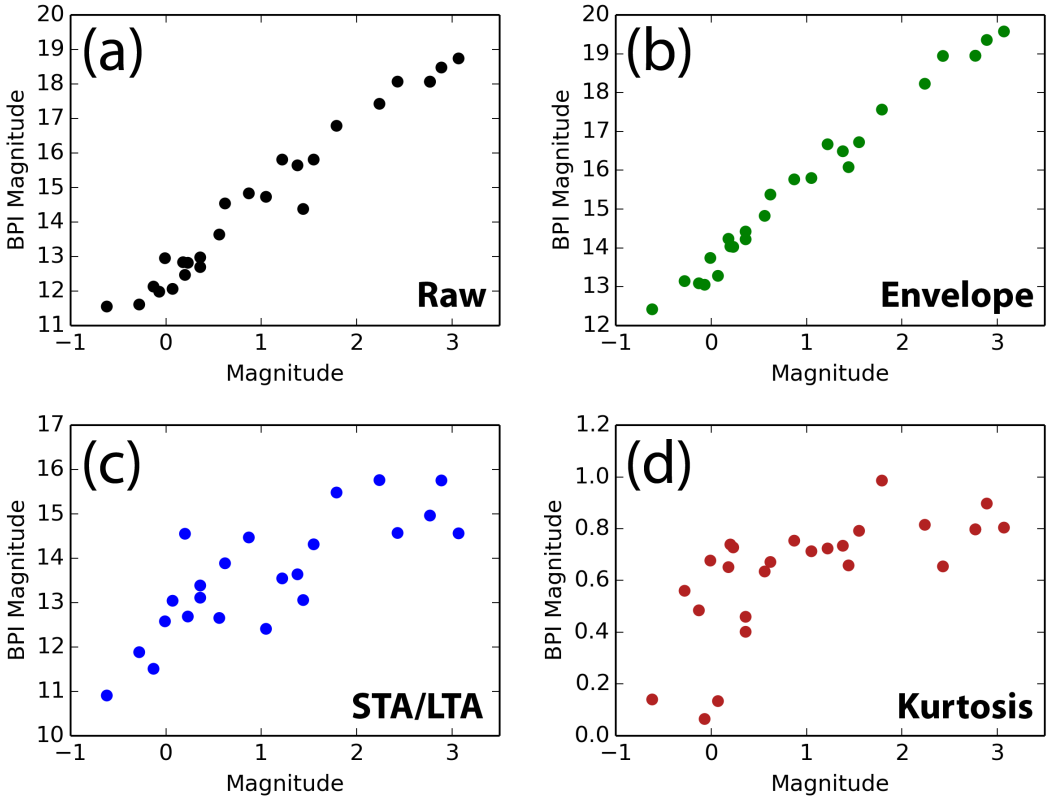

Figure 3.11: Base-10 logarithm of the peak energy in BPI (back-projection magnitude) plotted against magnitude from the catalog of Wu et al. (2015). a) raw seismogram, b) envelope, c) STA/LTA, d) kurtosis.

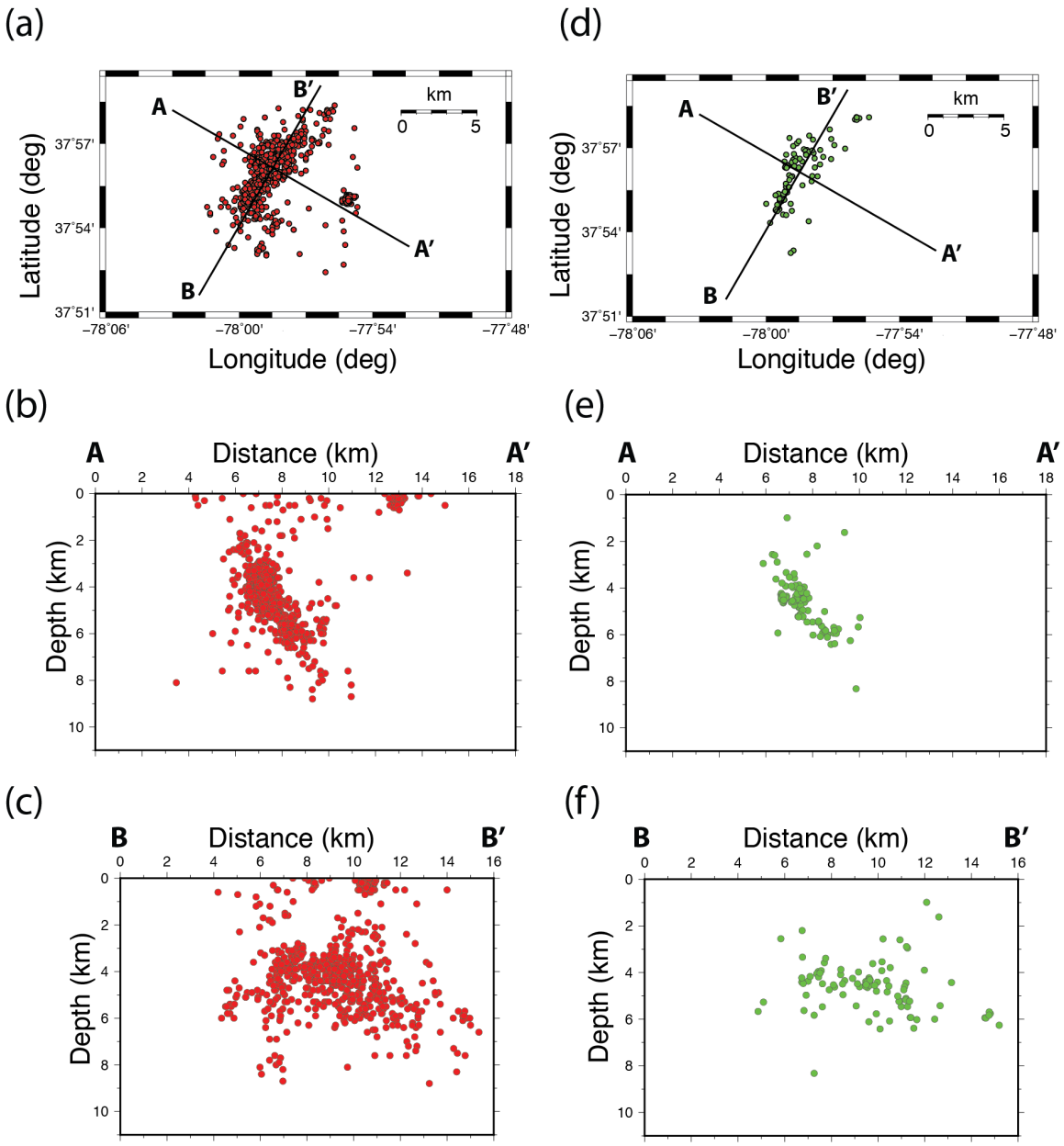

Figure 3.12: Earthquakes in a 48-hour period 4 days after the main shock. (a-c) hypocenters located by automated kurtosis-based back-projection of the AIDA dataset, (d-f) hypocenters from Wu et al. (2015) detected by STA/LTA from the sparser traditional aftershock network. a) and d) Map views, b) and e) depth slices across strike of the main shock and main aftershock zone (A-A'), c and f) depth slices along strike (B-B').

Chapter 4

Aftershock sequence of the 2011 Virginia earthquake derived from the dense AIDA array and back-projection

†**Citation:** Beskardes, G.D., Wu. Q, Hole J.A., Chapman M.C., Davenport K.K., Brown L.D. and Quiros D.A. (*in preparation*). Aftershock sequence of the 2011 Virginia earthquake derived from the dense AIDA array and back-projection.

Abstract

After the 23 August 2011 Mineral, Virginia earthquake, a temporary dense array (AIDA) consisting of ~200 stations was deployed at 200-400 m spacing near the epicenter for 12 days. Backprojection of the data was used to automatically detect and locate aftershocks. The co-deployment of a traditional aftershock network of 36 stations at ~2-10 km spacing enables a quantitative comparison. The AIDA backprojection aftershock catalog is complete to magnitude –1.0 and includes events as small as M–1.8. For comparison, the traditional network was complete to M–0.27 for the same time period. The AIDA backprojection catalog observes the same major patterns of seismicity in the epicentral region, but additional details are illuminated. The primary zone of seismicity has a subtle concave shape along strike and with depth, the zone of seismicity is thicker than a single fault, and a broader zone of new events is observed at shallow depth. In addition, a new separate, shallow cluster was located to the east of the main aftershock zone. Inclusion of the small events did not change the b-value or the temporal decay constant. However, both the b-value and temporal decay constant are different for 12 days than for 4 months and are different at < 3 km depth than at greater depth. The results indicate the benefits of dense arrays and auto-detection by backprojection for aftershock studies. The reduced detection threshold and higher spatial resolution enabled study of earthquake mechanisms and strain transfer at an unprecedented small scale.

4.1 Introduction

The M_w 5.7 Mineral, Virginia earthquake of 23 August 2011 was the largest and most damaging earthquake in the central and eastern United States for over a century (Chapman, 2013; McNamara et al., 2014; Horton et al., 2015a). It occurred at ~8 km depth on an unrecognized southeast dipping reverse fault and consisted of three sub-events with high stress drop (Chapman, 2013). The earthquake occurred in crystalline rock of the Appalachian Piedmont province within a previously recognized regional seismic zone (Chapman, 2013; Horton et al., 2015a). Aftershock studies delineate a north-east trending tabular zone of seismicity within 10 km of the main shock and also a cluster of shallow aftershocks ~10-20 km to the east and northeast of the main shock (McNamara et al., 2014; Wu et al., 2015; Horton et al., 2015b).

In comparison to plate-boundary earthquakes, intraplate earthquakes occur rarely due to low strain rates but represent a real hazard to society. The Virginia event and its aftershocks provide a rare opportunity to investigate intraplate seismicity, stress and strength, rupture processes, and local wave propagation (e.g., Horton et al., 2015a).

Aftershock sequences offer a rich understanding about earthquake sources, spatiotemporal evolution of stress and postseismic strain as well as future seismic hazards. Most aftershock studies such as the 2011 Virginia event, use local seismic networks consisted of a few dozen stations (e.g., Seeber et al., 2002; McLaren et al., 2008; Castro et al., 2011; Syracuse et al., 2013; McNamara et al., 2014; Brocher et al., 2015). Typical inter-station spacings are 5-30 km, resulting in spatially aliased data. Consequently, analyses of traditional earthquake net-

work data are limited to low absolute spatial resolution, typically kilometers, and aftershock detections are limited at smaller magnitudes. The gaps in catalogs due to the limitations in detection inherently impose gaps in the spatial distribution of aftershocks that is particularly important to delineate active fault zones and identify slip areas of main shocks (Fehler and Johnson, 1989).

Recording earthquake aftershock sequences at denser sampling lowers detection thresholds for low signal-to-noise events due to trace-to-trace correlation and enables array analysis methods such as back-projection and migration that provide higher spatial resolution. A more complete characterization of the aftershock volume has the potential to better illuminate earthquake source processes, detailed fault geometries, the evolving state of stress, dynamic and static stress triggering, and the geologic features that control stress and strength. Dense local arrays recently have been used in hydraulic fracturing studies (e.g., Gajewski and Tessmer, 2005; Chambers et al., 2010; Artman et al., 2010; Zhebel and Eisner, 2012, Vlček et al., 2015); in tectonic microseismicity studies (e.g., Hole et al., 2014, Inbal et al., 2015, Ben Zion et al., 2015); as well as in volcano seismicity studies (Hansen and Schmandt, 2015).

The backprojection imaging method migrates the energy released by an earthquake back to its source location through a known velocity structure(Kao and Shan, 2004; Ishii et al., 2005; Kiser et al., 2011; Kiser and Ishii, 2012). Back-projection involves stacking signal from many stations, so can improve the signal-to-noise ratio. Therefore event detection at all potential hypocenters after back-projection stacking has the capacity to detect and locate events that cannot be detected on single stations or traditional network (Chapter 3). Back-projection is

a simplified form of migration, and is therefore capable of achieving spatial resolution on the order of a wavelength. This resolution is comparable to double-difference methods (Chapter 3), as alignment and stacking at the correct hypocenter effectively perform the same function as cross-correlation and double-difference inversion.

Shortly after the main shock, an unusually large traditional aftershock network of 36 stations was deployed in the epicentral region (McNamara et al., 2014; Wu et al., 2015). To supplement this network and illustrate the merits of dense arrays, the 12-day Aftershock Imaging with Dense Arrays (AIDA) was deployed (Davenport et al., 2015; Quiros et al., in press). AIDA consisted of ~ 200 closely-spaced, single-component seismographs over the main shock and primary aftershock cluster. In this study, P-waves from the dense AIDA data were backprojected to automatically. The resulting catalog is interpreted and is compared with the catalog obtained from the traditional network.

4.2 The 2011 Mineral, Virginia Earthquake

The Mw 5.7 Mineral, Virginia earthquake of 23 August 2011 is the largest event within central Virginia seismic zone (CVSZ) since 1875 (e.g., Bollinger, 1969; Bollinger and Sibol, 1985). The CVSZ is a roughly elliptical area defined by persistent, generally low-level historical earthquake activity since at least 1774 (Bollinger and Sibol, 1985; Coruh et al., 1988). The past seismicity in this area includes both reverse and strike-slip motion with a southeast-northwest compression direction (Munsey and Bollinger, 1985; Kim and Chapman, 2005).

Seismicity within the CVSZ occurs at ~4-12 km depth within the overthrust sheets of the

crystalline Piedmont Province of central Appalachia (Hatcher, 1987; Coruh et al., 1988). Two major tectonic events formed the crustal structure of eastern Virginia: the Appalachian orogeny and the opening of the modern Atlantic Ocean (e.g., Hatcher, 1987). During the process of Appalachian orogeny, repeated collisions created a series of shallowly dipping (30° or less) reverse faults over a thin-skin detachment. During rifting that culminated in opening of the Atlantic Ocean, extensional fault systems were generated with steeper dips of 45-60°.

The past seismicity in this area present both reverse and strike-slip motion with a southeast-northwest compression direction (Munsey and Bollinger, 1985; Kim and Chapman, 2005). The August 2011 earthquake occured at a focal depth of 8 km on a southeast-dipping thrust fault (Chapman, 2013; McNamara et al., 2014). The complex rupture was composed of three subevents which propagated to the northeast and updip from the point of rupture initiation (Chapman, 2013). The primary aftershock zone continues this trend updip and to the northeast (McNamara et al., 2014; Wu et al., 2015; Davenport et al., 2015). The 2011 mainshock and the primary cluster of aftershocks strike ~N33°E with a dip of ~51°SE. This orientation does not correlate with the strike (Burton et al., 2015) or dip (Pratt et al.; 2015) of surface geology or seismically imaged subsurface features. The 2011 main shock and previous events had high 50-75 MPa stress drops with relatively slow rupture velocities of 1.3-1.7 km/s (Kim and Chapman, 2005; Chapman, 2013).

4.3 Aftershock Deployments

4.3.1 Large, Traditional Network

Following the 2011 Virginia earthquake, teams from the U.S. Geological Survey, Virginia Tech, University of Memphis, Lehigh University, and the Incorporated Research Institutions for Seismology (IRIS) deployed a temporary network of 36 stations near the epicenter (McNamara et al., 2014, Wu et al., 2015). Both broadband and strong motion sensors were installed at ~ 2-10 km spacing spread in an area of ~50 km x 50 km (Fig. 4.1). The stations recorded at 100-200 samples per second. Each station was deployed in about 1 day by a 2-person team and the entire deployment was completed within the first 5 days of the main shock.

This unusually large network deployment and low attenuation in crystalline rock resulted in a network catalog with a magnitude completeness of M_c–0.4 (Wu et al., 2015). In addition to the main cluster of seismicity coplanar with the main shock, an additional shallow cluster of seismicity occurred ~10-20 km to the east and northeast. Focal mechanisms indicate a mix of reverse and strike-slip faults suggesting that seismicity occurred on fault sets with different orientations(Wu et al., 2015). The maximum compressional direction is N100°E at $>$ 6 km depth, but indicates a 20° rotation (N80°E) at $<$ 4 km depth (Wu et al., 2015).

4.3.2 Dense AIDA Array

The AIDA deployment was the first attempt to use densely spaced stations to record the full wavefields of aftershocks of a major earthquake, rather than just their isolated waveforms. The goal was to demonstrate the feasibility of the application of seismic array processing methods on array-style aftershock recordings (Hole et al., 2011; 2014; Davenport et al., 2015; Quiros et al., in press).

Virginia Tech, Cornell University, and the U.S. Geological Survey deployed the AIDA array near the epicenter 4 days after the main shock. AIDA consisted of more than 200 single-component stations deployed along roads at 200-400 m spacing, spanning an aperture of ~12 km x 12 km (Fig. 4.1) (Davenport et al., 2015). Short-period 4.5 Hz, vertical-component, industry-style geophones were recorded at 100 samples per second. Utilizing stand-alone, small, industry seismographs enabled the entire array to be deployed in one afternoon by 6 people. However, the limitations of memory capacity and battery life of the 1990s vintage seismographs resulted in a low 100 samples per second sampling rate, visits every 3 days to maintain batteries and memory storage, and a deployment of only 12 days. The initial deployment was along two lines (Fig. 4.1) for six days. A second deployment re-occupied some of these sites, but added additional lines to the northeast (Fig. 4.1) to better center on then-new knowledge of the main epicenter and aftershock zone.

Fig. 4.2 shows examples of earthquakes recorded by AIDA. Clear P- and S-wave arrivals are not or weakly aliased along the roads. Close station spacing enables visible detection of weak events via trace-to-trace correlation. In comparison, the sparser traditional network

fails to detect small aftershocks easily detected by AIDA due to spatial aliasing (Fig. 4.2c). Additional arrivals are observed between the P- and S-waves and have been used to image crustal reflectors (Quiros et al., in press).

3D seismic P- and S-wave velocity models were derived by local earthquake tomography using P and S arrival times from more than 300 aftershocks in the AIDA dataset (Davenport et al., 2015). The tomography was capable of resolving structure with ¡1 km spatial resolution. The resulting velocity model indicates a medium that is homogeneous within resolution, with V_P = 6.2 km/s and V_S = 3.62 km/s. This constant velocity is consistent with the crystalline rocks of the Piedmont Province and very thin (~10 m) weathering layer above bedrock. The root-mean-square misfit of the constant-velocity 3D model is 17 ms (Davenport et al., 2015), less than half of the dominant period; therefore, it should be sufficient to stack in seismograms by backprojection.

4.4 Back-Projection Method

Backprojection imaging of P-wave arrivals was used to detect and locate aftershocks of the 2011 Virginia aftershock sequence recorded by the AIDA array. Backprojection is a simplification of reverse-time migration, which propagates the wavefield energy recorded by the seismic array backwards in time through a known velocity model to the energys source (McMechan, 1982). Backprojection ignores magnitudes, simply shifting observed seismograms by the time delay between the image point and the station, and stacking the time-shifted seismograms (Ishii et al., 2005; Chapter 3). The method is scalable in magnitude and has become a common approach to locate earthquake source energy for major earth-

quakes (e.g., Ishii et al., 2007; Xu et al., 2009; Walker and Shearer, 2009; Kiser and Ishii, 2012; Koper et al., 2012), industry hydraulic fracturing microseismicity (e.g., Chambers et al., 2010; Zhebel and Eisner, 2012, Vlcek et al., 2015), tectonic microseismicity (Inbal et al., 2015), and volcano seismicity (Haney et al., 2014; Langet et al., 2014; Hansen and Schmandt, 2015).

Back-projection is generally performed on events previously detected by other methods. These other methods depend on detection on single seismograms, and near-simultaneous detections on multiple stations. On the other hand, backprojection provides an important advantage over single-seismogram detection methods by improving the signal-to-noise ratio through stacking. This enables detection of events that cannot be detected on individual seismograms, including events smaller than the noise (Gajewski and Tessmer, 2005; Chapter 3).

The application of backprojection to real data is often challenging due to seismic noise, spatially-aliased secondary phases, polarity reversals caused by the focal mechanism, uncertainties in the velocity model, sparse station spacing, or small array aperture (Chapter 3). Most applications pre-process the data to produce broader and/or positive-only waveforms that stack in easier, at the expense of imaging with lower spatial resolution. Based on a comparative analysis of these methods (Chapter 3), a two-phase backprojection procedure was applied to the 12-day AIDA dataset.

First, the seismograms were pre-processed to compute their kurtosis. Kurtosis is the fourth central moment in statistics, describing the peakedness and tails of a distribution (Spanos, 1999). Kurtosis is robust detector of seismic arrivals (e.g., Saragiotis et al., 2002; Kuperkoch

et al., 2010; Nippress et al., 2010) and is similarly robust for backprojection (Langet et al., 2014; Chapter 3). A 500 ms moving time window was used to compute seismic traces of local kurtosis.

The kurtosis waveforms were then blindly backprojected to simultaneously detect and locate aftershocks without the need for noise removal or polarity corrections. Travel time between grid nodes was trivial to compute in the 3D velocity model that consisted of a constant velocity (Davenport et al., 2015). Back-projection was performed for the entire 12-day dataset at 10 ms sampling and at a 100 m grid spacing within a 12 x 12 x 9 km volume beneath the AIDA array (e.g., Fig. 4.3). Aftershocks were detected whenever peak energy of the stack exceeded a pre-determined threshold. Aftershocks at the edges of the volume were discarded since they probably represent sources outside the volume. This process resulted in an earthquake catalog consisting of earthquake locations and origin times.

Subsequently, for each hypocenter in this catalog, the original field seismograms were time-corrected for the hypocenter and cross-correlated with the stacked seismogram to determine and correct polarity. A spatial median filter using stations within 1.5 km was applied to station polarity to obtain the dominant polarity and allow sharp polarity boundaries. The seismic traces were multiplied by distance between the hypocenter and station to correct for spherical divergence. The polarity and amplitude-corrected seismograms were then back-projected using a small time and spatial window near the kurtosis hypocenter to obtain the backprojection peak amplitudes to estimate the magnitude correlation with the magnitudes from the traditional network catalog. This imaging was sampled at 10 ms and 50 m. Rather than a simple stack, a diversity stack (Embree, 1968) was applied to reduce the effect of

noisy traces.

The magnitudes of the aftershocks were determined using correlation between the backprojection image peak amplitudes and the corresponding magnitudes of the same earthquakes in the traditional network catalog of Wu et al. (2015). The aftershocks common to both catalogs demonstrate a linear relationship in log space (Fig. 4.4). A similar linear correlation was reported for backprojection of the 2011 Tohoku aftershock sequence (Kiser and Ishii, 2013). The least-squares linear relationship is $log_{10}(\text{Amplitude}_{BPI})$= 1.89(Magnitude) – 8.24. Based on this, backprojection magnitudes (M_{BPI}) were computed for all events in the backprojection catalog.

4.5 The Back-projection Catalog

Applying automated kurtosis-based P-wave backprojection to the entire AIDA dataset resulted in the detection and simultaneous location of 1673 aftershocks within the 12 day deployment, starting 4 days after the main shock (Appendix). To evaluate the completeness of the backprojection catalog in space, time, and magnitude, it was directly compared with the traditional network catalog of Wu et al. (2015). For fair comparison, we only consider aftershocks from the Wu et al. catalog that occurred within the recording period and the constrained search volume spanned by the AIDA backprojection. The backprojection catalog successfully recovered all 494 aftershocks located by the traditional network in that time and spatial range. Moreover, backprojection located an additional 1209 earthquakes, an increase in detection by a factor of ~3.5.

The smallest detected and located aftershock in the backprojection catalog has a magnitude of –1.8. The magnitude distribution of the backprojection catalog (Fig. 4.5a) exhibits a high concentration at smaller magnitudes compared to the traditional network catalog. Several hundred previously undetected aftershocks ranging from M 0 to M –1.8 were detected and located.

The location errors of the hypocenters in the network catalog were reported as ~ 0.66 km in horizontal and ~ 2.01 km in vertical direction after using double-difference method (Wu et al., 2015). AIDAs hypocenters have much better absolute accuracy, including velocity tradeoff, of < 100 m enabled by the high resolution velocity model obtained from the dense array (Davenport, et al., 2015). Within that velocity model, the median back-projection location accuracies are ~ 0.09 km in horizontal and ~ 0.2 km in vertical direction.

Fig. 4.7 shows map view and cross sections of the aftershocks of both catalogs. They present a consistent spatial distribution of aftershocks in the main shock region. However, the backprojection catalog provides a more detailed image of the seismicity. It reveals a noticeable abundance and distinct strikes of small shallow aftershocks as well as a new shallow cluster to the east.

4.6 Earthquake Statistics: Extension to smaller magnitudes

The AIDA backprojection aftershock catalog (Appendix, Fig. 4.7) has lower detection and location thresholds than previous work, which enables investigation of seismic processes at

smaller magnitudes.

The scaling between the frequency of occurrence and the magnitude of earthquakes is described by the Gutenberg-Richter relation (Ishimoto and Iida, 1939; Gutenberg and Richter, 1944):

$$log_{10}N = a - bM_{BPI}, \tag{4.1}$$

where N is the cumulative number of earthquakes having magnitudes equal or greater M_{BPI}, and a and b are empirical parameters derived by fitting observations to a straight line. The b value of the frequency-magnitude relationship varies between 0.6 and 1.4 (e.g., Wiemer and Wyss, 1997). The spatial variability of b-value as well as its variations with depth is often hypothesized as inversely proportional to stress and directly proportional to material heterogeneity (e.g., Mogi, 1962, Scholz, 1968; Urbancic et al., 1992; Mori and Abercrombie, 1997; Wiemer and Wyss, 1997, Stein and Wysession, 2003). Low b-values are thought to correspond to highly stressed asperities of active faults (Wiemer and Wyss, 1997) while high b-values correspond to the creeping section of faults (Amelung and King, 1997).

The frequency-magnitude distribution of the Virginia aftershock sequence (Fig. 4.5b) is well approximated by the Gutenberg-Richter relation. The magnitude completeness (M_c) of the AIDA backprojection catalog is M –1.0 using the maximum likelihood procedure described in Wiemer and Wyss (2000). The completeness (M_c) of the traditional network catalog of Wu et al. (2015) during the same 12 days and restricted to the AIDA backprojection volume is –0.27 (Fig. 4.5b, green). The dense AIDA array and backprojection detection have significantly improved the catalog completeness beneath the array. The traditional array spanned a wider area, and detected additional events outside the AIDA catalog. Backprojection using a larger

search volume detected most of these events, but could not improve the location accuracy for events far outside the AIDA array.

The b-value of the backprojection aftershock sequence is 0.713 ± 0.087 and the a-value is 2.60 (Fig. 4.5b, red). The b-value of the traditional network aftershocks of Wu et al. (2015) during the same 12 days and located within the AIDA backprojection volume is 0.705±0.071 (Fig. 4.5b, green). This good agreement indicates that the frequency-magnitude relation is consistent at smaller magnitudes. The b-value is a little larger when measured over a few months, where McNamara et al. (2014) observed 0.747±0.04 and Wu et al. (2015) observed 0.864±0.013 (Fig. 4.5b, gray). All of these values are relatively low and consistent with intraplate seismicity (0.865±0.226; Ebel, 2009).

In addition, the b-values of the aftershock sequence within different depth ranges indicate a decrease in depth (Fig. 4.5c). The b-value of the aftershocks shallower than 3 km depth is 0.893±0.053 (Fig. 4.5c, pink); on the other hand, the b-value of the aftershocks at > 3 km depth is estimated to be 0.679±0.092 (Fig.4.5c, yellow).

The decay rate of the aftershock activity with time (Fig. 4.6a) is approximated by the modified Omori's law (e.g., Utsu, 1995):

$$\frac{dN}{dt} = \frac{C_2}{(C_2 + t)^p}, \tag{4.2}$$

where N is the number of the earthquakes per day; t is the elapsed time since the main shock in days; p, C_1, and C_2 are parameters that are fit empirically. The empirical decay exponent p-value" defines the temporal decay rate of the aftershocks. Typical p-values are within the range of 0.6 and 1.8 for different aftershock sequences (Wiemer and Katsumata,

1999) and may differ spatially and sometimes temporarily (e.g., Utsu, 1995). Fig. 4.6a (red) shows that the aftershock sequence detected by backprojection decays with a low p-value of 0.564 ± 0.163. The other constants are estimated as $C_1 = 165.030 \pm 67.933$ and $C_2 = -3.733 \pm 1.110$. The aftershocks from the traditional network catalog of Wu et al. (2015) over the same 12 days and spatial volume result in a p-value of 0.578 ± 0.368 (Fig. 4.6a, green). The traditional catalog is very similar but has relatively high standard error. On the other hand, the seismicity decay obtained from the entire traditional network catalog through 129 days has a much higher p-value of 1.085 ± 0.058 (Wu et al., 2015). The temporal change from 12 days to 4 months may be related to systematic absence of detections at smaller magnitudes.

Further, the p-values of the aftershock sequence within different depth ranges indicate a significant change with depth (Fig. 4.6b). Aftershocks at > 3 km depth decay with a p-value of 0.721 ± 0.249 (pink), higher than the entire aftershock activity. On the other hand, aftershocks shallower than 3 km depth decay much slower, with a smaller p-value of 0.356 ± 0.287 (yellow).

4.7 Spatial-temporal Aftershock Patterns

The majority of the backprojection aftershocks align in a northeast-striking concentration similar in orientation to the main shock's focal plane (Fig. 4.7) (Chapman, 2013; McNamara et al., 2014; Wu et al., 2015; Horton et al., 2015b). The average strike and dip of this main cluster are consistent with previous observations. It does not coincide with the orientations of any pre-existing geologic structures, mapped faults, or seismic reflections in the region,

illuminating a previously unknown fault zone (Burton et al., 2015; Pratt et al.; 2015; Horton et al., 2015b). The fault zone is > 1 km thick (Fig. 4.7a), despite hypocenters that are accurate to < 100 m, as indicated by the AIDA tomography (Davenport et al., 2015). This indicates that the events did not occur on a single fault plane, but in a narrow zone. This is consistent with the mix of reverse and strike-slip focal mechanisms (Wu et al., 2015).

The along-strike distribution of aftershocks (Fig. 4.7a) shows that the deeper aftershocks occurred predominantly near the hypocenter of the main shock. The ~5 km along-strike and 2-3 km down-dip gap in seismicity above these events corresponds to the main shock rupture zone (Chapman, 2013). Most of the aftershocks in the main cluster are up-dip and to the northeast of the main shock (Fig. 4.7a). The three sub-events of the main shock propagated shallower and to the northeast (Chapman, 2013). The aftershock zone supports the inference that main-shock rupture directivity controls the asymmetric distribution of the aftershocks (Gomberg et. al, 2003; Wu et al., 2015).

The main cluster is not perfectly planar, but smoothly bends along strike and with depth (Fig. 4.7a), as suggested by some previous studies (Davenport et al., 2015; Horton et al., 2015b) but missed in others (McNamara et al., 2014; Wu et al., 2015). The high-resolution backprojection catalog validates an arcuate, concave upward pattern.

Above ~3 km depth in the across-strike section, the traditional network catalog indicates that the main fault zone extends linearly towards the surface (Fig. 4.7b). The backprojection catalog includes these events, but adds numerous small events that were not previously detected in a roughly triangular zone above the planar trend (Fig. 4.7a, section across strike). This suggests rupture on minor splay and/or conjugate faults as the main trend

approaches the surface.

A distinct, shallow cluster of aftershocks is observed to the east of the main cluster (Fig. 4.7a). This cluster has not been previously reported (Fig. 4.7b). The magnitudes in this cluster vary between M–1.4 to M1. Shallow (< 4 km depth) clusters further to the northeast were observed in the traditional network catalog, 10-20 km from the main shock (Fig. 4.7b). These events have a northeastern trend approximately parallel to the strike of mapped Paleozoic geologic structure, but have focal mechanisms that strike northwest and a maximum horizontal stress trending northeast (Wu et al., 2015). These shallow clusters are similar in depth and magnitude and roughly along strike with the new shallow cluster observed in Fig. 4.7a. The northeastern clusters were not included in the backprojection catalog since backprojection of these events far outside the AIDA array results in poorly-located hypocenters. Due to the sparse stations of the traditional network and the limited aperture of the AIDA array, neither catalog can clarify if there are similar small-magnitude clusters linking the shallow eastern cluster in the backprojection catalog with the clusters further northeast in the network catalog.

The temporal evolution of seismicity (Fig. 4.8) shows that most of the aftershock zones persist through the 12 day window. The one exception is that shallow aftershocks in and above the main fault-zone cluster mostly occur more than 8 days after the main shock. On the other hand, the eastern shallow cluster is active throughout the 12 days. Most of the seismicity during the early 12-day deployment of the AIDA array is spatially similar to that of the 129-day traditional network (Wu et al., 2015).

4.8 Discussion and Conclusions

The AIDA array significantly lowers the detection threshold by capturing the weak signals of tiny aftershocks at a sufficient number of closely spaced stations. Furthermore, the back-projection increased the signal-to-noise ratio of tiny events by stacking many seismograms and enabled detection and simultaneous location of events with signal so small they cannot be detected on single stations. The backprojection catalog detected a factor of ~3.5 more aftershocks than careful analysis of the unusually large, 36-station, traditional aftershock network (Wu et al., 2015). The backprojection catalog is complete to magnitude –1.0, a significant improvement from the already impressive magnitude –0.4 completeness of the traditional catalog.

The backprojection catalog adds additional smaller events to the traditional network catalog of Wu et al. (2015) (Fig. 4.5) for 12 days in a more limited volume that includes the entire main fault zone. These additional events do not change the Gutenburg-Richter b-value (Fig. 4.5) or Omori Law temporal decay constant p-value (Fig. 4.6) for the 12 days and the same volume. On the other hand, the 12-day b-value is slightly lower than that observed over 4 months by the traditional network and the 12-day p-value is much smaller than that for 4 months (Figs. 4.6). The low b value is consistent with the high stress drops observed for the main shock and larger aftershocks (Chapman, 2013; Wu et al., submitted) and previous studies that suggest low b values for high stress (e.g., Urbancic et al., 1992; Wiemer and Wyss, 1997). In addition, both b-value and p-value vary from < 3 to > 3 km depth. Shallow seismicity includes fewer large events (higher b-value) and the shallow aftershocks decay with a p-value half the decay rate of the deeper aftershocks (Figs. 4.5 and 4.6). These

temporal and spatial changes exist in the traditional catalog of Wu et al. (2015), but were not previously noticed. The low b-value of the aftershocks at > 3 km depth is consistent with the high stress at deeper parts of the fault zone. The decrease in b value with depth is consistent with previous interpretations, possibly due to increased applied stress (Mori and Abercrombie, 1997; Wiemer and Wyss, 1997; Wiemer and Katsumata, 1999).

The temporal distribution of the aftershocks shows that shallow aftershocks in the main cluster occur relatively later in the updip direction from the main shock hypocenter. The simultaneous occurrence of the east shallow aftershocks with the early aftershocks of the main cluster does not show a clear evidence for the effect of dynamic triggering. The seismicity that occurred within the 12 day time range presents a very similar spatial distribution to the ~4 month time range of the network catalog, suggesting that the distribution of aftershocks was strongly controlled by the static stress change caused by the main shock's rupture. The exception is the shallow aftershocks in the main cluster, which occur > 8 days after the main shock in the updip direction. This suggests dependence upon the static stress changes from the first week of aftershocks. The new, shallow, eastern cluster persists for the full 12 days, suggesting it also was controlled by the main shock static stress change.

The detailed seismicity obtained from backprojection of the dense AIDA array shows patterns consistent with the network catalog but also emphasizes the incompleteness of the network catalog at smaller magnitudes. The additional small-magnitude seismicity and high-resolution hypocenters delineate additional details. The spatial accuracy of the hypocenters is about an order of magnitude better than that of the traditional network, due to the dense recording, stacking during back-projection (similar to cross-correlation), improved 3D veloc-

ity model (Davenport et al., 2015), and back-projection imaging (similar to migration, which is a spatial inversion). New details delineated by AIDA include: the main tabular zone is too thick to be a single fault and has a concave-upwards shape, a broader zone of newly observed seismicity exists above the main zone at shallow depth, and a new shallow cluster exists ~5 km to the east.

The main tabular zone of seismicity is > 1 km thick, much thicker than the hypocentral errors, consistent with the results of Davenport et al. (2015). This indicates that the seismicity does not occur on a single fault. A primary fault is not detected within this main cluster. The cluster represents a tabular zone where static Coulomb stress change and main-shock rupture directivity caused abundant events on multiple faults updip and to the northeast of the main shock. This is consistent with Wu et al. (2015), who reported different focal mechanisms within the tabular zone. Consistent with Davenport et al. (2015) and Horton et al. (2015b), this tabular zone is concave upwards and curves along strike.

A shallow cluster located to the east of the main cluster, including magnitudes from M –1.4 to M 1, was not previously detected by the network catalog. Backprojection detected but could not accurately locate many additional hypocenters to the east and northeast, outside the AIDA array. Intriguing clusters of seismicity with properties different than the main fault zone exist in this direction (Wu et al., 2015). However, the lack of dense stations in that region does not enable correlation of the new cluster to the clusters further northeast. A new zone of seismicity was also observed immediately above the main tabular zone at shallow depth. This zone may consist of splay or antithetic faults, or may have rotated stress similar to that observed in the eastern clusters (Wu et al., 2015). These newly observed clusters

of seismicity suggest that other small-magnitude seismicity was missed beyond the AIDA array.

The AIDA array benefited from a dense, poorly or non-aliased inline station spacing. However, its spacing between lines may have been insufficient if the velocity structure had been more complex. We would advocate for more lines or a full dense grid to better record the next aftershock sequence. Similarly, the ~12-km aperture of the AIDA array was large enough to cover the main fault zone in Virginia, but only because the large stress drop of this event produced a relatively small zone of faulting. Additional lines or a grid of stations and a larger spatial aperture would both require many more stations. Thousands of stations with large aperture and high spatial and temporal sampling rates are commonly deployed by industry, including for hydraulic fracturing microseismicity studies (e.g. Zhebel and Eisner, 2012; Anikiev et al., 2014; Vlček et al., 2015). These industry studies show the capabilities of truly large arrays to be deployed and to lower the detection threshold.

The differences between the AIDA backprojection catalog and that produced from a traditional deployment with an unusually large number of stations highlights the importance of the completeness at low magnitude and the spatial resolution of earthquake catalogs. High-resolution catalogs that are more complete in magnitudes can delineate complex fault zones in more detail. This can enable a better understanding of the evolution of stress and strain in the epicentral region and can better correlate seismicity with existing geological and geomorphological structures. The latter is especially important for a fault zone that does not correlate with any previously mapped fault, such as the 2011 Virginia earthquake. Moreover, more complete and accurate catalogs may also help improve our understanding of

static and dynamic stress and the role of fluids in aftershock triggering. For these reasons, we advocate aftershock deployments with denser lines or grids and a larger spatial aperture, requiring many hundreds to a few thousand stations. Such deployments are practical and proven by industry.

References

Anikiev, D., Valenta, J., Stanek, F., & Eisner, L., 2014. Joint location and source mechanism inversion of microseismic events: benchmarking on seismicity induced by hydraulic fracturing. *Geophysical Journal International*, **198**, 1, 249–258.

Amelung, F., & King, G., 1997. Earthquake scaling laws for creeping and noncreeping faults. *Geophysical Research Letters*, **24**, 5, 507–510.

Artman, B., Podladtchikov, I., & Witten, B., 2010. Source location using time-reverse imaging. *Geophysical Prospecting*, **58**, 5, 861–873.

Ben-Zion, Y., Vernon, F. L., Ozakin, Y., Zigone, D., Ross, Z. E., Meng, H., & Barklage, M. (2015). Basic data features and results from a spatially dense seismic array on the San Jacinto fault zone. *Geophysical Journal International*, **202**, 1, 370–380.

Bollinger, G. A., 1969. Seismicity of the central Appalachian states of Virginia, West Virginia, and Maryland–1758 through 1968. *Bull. Seismol. Soc. Am.*, **59**, 2103–2111.

Bollinger, G.A., & Sibol, M.S., 1985, Seismicity, seismic reflection studies, gravity and geology of the central Virginia seismic zone: Part I. Seismicity. *Geological Society of America Bulletin*, **96**, 49–57.

Brocher, T. M., Baltay, A. S., Hardebeck, J. L., Pollitz, F. F., Murray, J. R., Llenos, A. L., Schwartz, D. P., Blair, J. L., Ponti, D. J., Lienkaemper, J. J., Langenheim, V. E., Dawson, T. E., Hudnut, K. W., Shelly, D. R., Dreger, D. S., Boatwright, J., Aagaard, B. T., Wald, D. J., Allen, R. M., Barnhart, W. D., Knudsen, K. L., Brooks, B. A., & Scharer, K. M., 2015. The Mw6.0 24 August 2014 South Napa Earthquake. *Seismol. Res. Lett.*, **86**, 309–326.

Burton, W. C., Harrison, R. W., Spears, D. B., Evans, N. H., & Mahan, S., 2015. Geologic framework and evidence for neotectonics in the epicentral area of the 2011 Mineral, Virginia, earthquake, in The 2011 Mineral, Virginia, Earthquake and Its Significance for Seismic Hazards in Eastern North America, J. W. Horton Jr., M. C. Chapman, & R. A. Green (Editors). *Geological Society of America Special Papers*, **509**, 345–376.

Castro, R. R., Acosta, J. G., Wong, V. M., Prez-Vertti, A., Mendoza, A., & Inzunza, L., 2011. Location of Aftershocks of the 4 April 2010 Mw 7.2 El Mayor–Cucapah Earthquake of Baja California, Mexico. *Bull. Seismol. Soc. Amer.*, **101**, 3072–3080.

Chambers, K., Kendall, J., BrandsbergDahl, S., & Rueda, J., 2010. Testing the ability of surface arrays to monitor microseismic activity. *Geophysical Prospecting*, **58**, 5, 821–830.

Chapman, M. C., 2013. On the rupture process of the 23 August 2011 Virginia earthquake. *Bull. Seismol. Soc. Am.*, **103**, 613–628.

Coruh, C., Bollinger, G.A., & Costain, J.K., 1988. Seismogenic structures in the central Virginia seismic zone. *Geology*, **16**, 748–751.

Davenport, K. K., Hole, J. A., Quiros, D. A., Brown, L. D., Chapman, M. C., Han, L., & Mooney, W. D., 2015. Aftershock imaging using a dense seismometer array (AIDA) after the 2011 Mineral, Virginia earthquake, in The 2011 Mineral, Virginia, Earthquake and Its Significance for Seismic Hazards in Eastern North America, J.W. Horton Jr.,M. C. Chapman, & R. A. Green (Editors). *Geological Society of America Special Papers*, **509**, 273–283.

Ebel, J. E., 2009. Analysis of aftershock and foreshock activity in stable continental regions: Implications for aftershock forecasting and the hazard of strong earthquakes. *Seismol. Res. Lett.*, **80**, 1062–1068.

Embree, P. 1968, Diversity seismic record stacking method and system. *U.S. Patent*, No.3, 398,396.

Fehler, M., & Johnson, P., 1989. Determination of fault planes at Coalinga, California, by analysis of patterns in aftershock locations. *Journal of Geophysical Research: Solid Earth*, **94**, B6, 7496–7506.

Gajewski, D., & Tessmer, E., 2005. Reverse modelling for seismic event characterization. *Geophysical Journal International*, **163**, 1, 276–284.

Gomberg, J., Bodin, P. & Reasonberg, P. A., 2003. Observing earthquakes triggered in the near field by dynamic deformations. *Bull. Seismol. Soc. Am.*, **93**, 118–138.

Gutenberg, R., & C. F. Richter, 1944. Frequency of earthquakes in California. *Bull. Seismol. Soc. Am.*, **34**, 185–188.

Haney, M. M., 2014. Backprojection of volcanic tremor. *Geophysical Research Letters*, **41**, 6, 1923–1928.

Hansen, S. M., & Schmandt, B., 2015. Automated detection and location of microseismicity at Mount St. Helens with a largeN geophone array. *Geophysical Research Letters*, **42**, 18, 7390–7397.

Hatcher, R.D., 1987. Tectonics of the southern and central Appalachian internides. *Annual Review of Earth and Planetary Sciences*, **15**, 337–362

Hole, J. A., Davenport, K. K., Han, L., Chapman, M. C., Quiros, D. A., Chen, C., Brown, L. D., Lohman, R. B., Ferguson, A. J.,. Fennig, N., & Mooney, W. D., 2011. Dense array recordings of the central Virginia earthquake aftershock sequence: a prototype for Flexi-

RAMP. *EOS Trans. Amer. Geophys. Union*, **92**, Fall Meeting Suppl., Abstract S11B-2236.

Hole, J. A., Wang, K., Davenport, K. K., Chapman, M. C., Beskardes, G. D., Quiros, D. A., Brown, L. D., & Mooney, W. D., 2014. Back-Projection Imaging of Aftershocks Recorded by the Dense AIDA Array After the 2011 Virginia Earthquake. *Seismol. Res. Lett.*, **85**, 2, 434.

Horton, J. W., Jr., Chapman, M. C., & Green, R. A., eds., 2015a. Aftershock imaging using a dense seismometer array (AIDA) after the 2011 Mineral, Virginia earthquake, in The 2011 Mineral, Virginia, Earthquake and Its Significance for Seismic Hazards in Eastern North America, J.W. Horton Jr.,M. C. Chapman, & R. A. Green (Editors). *Geological Society of America Special Papers*, **509**, 431 pp., doi:10.1130/9780813725093.

Horton, J. W., Shah, A. K., McNamara, D. E., Snyder, S. L. & Carter, A. M., 2015b. Aftershocks illuminate the 2011 Mineral, Virginia, earthquake causative fault zone and nearby active faults, in The 2011 Mineral, Virginia, Earthquake and Its Significance for Seismic Hazards in Eastern North America, J. W. Horton Jr., M. C. Chapman, & R. A. Green (Editors). *Geological Society of America Special Papers*, **509**, 253–272, doi: 10.1130/2015.2509(14).

Inbal, A., Clayton, R. W., & Ampuero, J. P., 2015. Imaging widespread seismicity at midlower crustal depths beneath Long Beach, CA, with a dense seismic array: Evidence for a depthdependent earthquake size distribution. *Geophysical Research Letters*, **42**, 15, 6314–6323.

Ishii, M., Shearer, P. M., Houston, H. & Vidale, J. E., 2005. Extent, duration and speed of the 2004 SumatraAndaman earthquake imaged by the Hi-Net array. *Nature*, **435**, 7044, 933–936.

Ishii, M., Shearer, P. M., Houston, H., & Vidale, J. E., 2007. Teleseismic P wave imaging of

the 26 December 2004 SumatraAndaman and 28 March 2005 Sumatra earthquake ruptures using the Hinet array. *Journal of Geophysical Research: Solid Earth*, **112**, B11.

Ishimoto, M., & Iida, K., 1939. Observations of earthquakes registered with the microseismograph constructed recently. *Bull. Earthq. Res. Inst.*, **17**, 443–478.

Kao, H., & Shan, S., 2004. The source-scanning algorithm: mapping the distribution of seismic sources in time and space. *Geophysical Journal International*, **157**, 589–594.

Kim, W., & Chapman, M., 2005. The 9 December 2003 central Virginia earthquake sequence: A compound earthquake in the central Virginia seismic zone. *Bull. Seismol. Soc. Am.*, **95**, 2428–2445.

Kiser, E., Ishii, M., Langmuir, C. H., Shearer, P. M., & Hirose, H., 2011. Insights into the mechanism of intermediate-depth earthquakes from source properties as imaged by back projection of multiple seismic phases. *Journal of Geophysical Research: Solid Earth*, **116**, B6.

Kiser, E., & Ishii, M., 2012. The March 11, 2011 Tohoku-oki earthquake and cascading failure of the plate interface. *Geophysical Research Letters*, **39**, 7.

Kiser, E., & Ishii, M., 2013. Hidden aftershocks of the 2011 Mw 9.0 Tohoku, Japan earthquake imaged with the backprojection method. *Journal of Geophysical Research: Solid Earth*, **118**, 10, 5564–5576.

Koper, K. D., Hutko, A. R., Lay, T., & Sufri, O., 2012. Imaging short-period seismic radiation from the 27 February 2010 Chile (Mw 8.8) earthquake by back-projection of P, PP, and PKIKP waves. *Journal of Geophysical Research: Solid Earth*, **117**, no.B2.

Kuperkoch, L., Meier, T., Lee, J., Friederich, W., & EGELADOS Working Group, 2010. Automated determination of P-phase arrival times at regional and local distances using higher order statistics. *Geophysical Journal International*, **181**, 1159–1170.

Langet, N., Maggi, A., Michelini, A., & Brenguier, F., 2014. Continuous Kurtosisbased migration for seismic event detection and location, with application to Piton de la Fournaise Volcano, La Réunion. *Bulletin of the Seismological Society of America*, **104**, 1, 229–246.

McLaren, M. K., Hardebeck, J. L , van der Elst, N., Unruh, J. R., Bawden, G. W., & Blair, J. L., 2008. Complex faulting associated with the 22 December 2003 M-w 6.5 San Simeon, California, earthquake, aftershocks, and postseismic surface deformation. *Bull., Seismol. Soc. Amer.*, **98**, 1659–1680, doi: 10.1785/0120070088.

McMechan, George A., 1982. Determination of source parameters by wavefield extrapolation. *Geophysical Journal International*, **71**, 3, 613–628.

McNamara, D. E., Benz, H. M., Herrmann, R. B., Bergman, E. A., Earle, P., Meltzer, A., Withers, M., & Chapman, M., 2014. The Mw 5.8 Mineral, Virginia, earthquake of August 2011 and aftershock sequence: Constraints on earthquake source parameters and fault geometry. *Bull. Seismol. Soc. Am.*, **104**, 40–54.

Mogi, K., 1962. Magnitude-frequency relation for elastic shocks accompanying fractures of various materials and some related problems in earthquakes. *Bull. Earthquake Res. Inst.*, Univ. Tokyo, **40**, 831–853.

Mori, J., & Abercrombie, R. E., 1997. Depth dependence of earthquake frequencymagnitude distributions in California: Implications for rupture initiation. *Journal of Geophysical Research: Solid Earth*, **102**, B7, 15081–15090.

Munsey, J.W., & Bollinger, G.A., 1985. Focal mechanism analyses for Virginia earthquakes (19781984). *Seismological Society of America Bulletin*, **75**, 1613–1636.

Nippress, S. E. J., Rietbrock, A., & Heath, A.E., 2010. Optimized automatic pickers: application to the ANCORP data set. *Geophysical Journal International*, **181**, 911–925.

Pratt, T. L., J. W. Horton Jr., D. B. Spears, A. K. Gilmer, & D. E. McNamara, 2015. The 2011 Virginia Mw 5.8 earthquake: Insights from seismic reflection imaging into the influence of older structures on eastern U.S. seismicity, in The 2011 Mineral, Virginia, Earthquake and its Significance for Seismic Hazards in Eastern North America, J. W. Horton Jr., M. C. Chapman, & R. A. Green (Editors). *Geological Society of America Special Papers*, **509**, 285–294, doi:10.1130/2014.2509(16).

Saragiotis, C., Hadjileontiadis, L. & Panas, S., 2002. PAI-S/K: a robust automatic seismic P phase arrival identification scheme. *IEEE Trans. Geosci. Remote Sens.*, **40**, 1395–1404.

Spanos, A., 1999. Probability theory and statistical inference: econometric modeling with observational data. *Cambridge University Press*, 117–124.

Quiros, D. A., Brown, L. D., Davenport, K. K., Hole, J. A., Cabolova, A., Chen, C., Han, L., Chapman, M. C., & Mooney, W. (in press). Reflection imaging with earthquake sources and dense arrays. *Journal of Geophysical Research: Solid Earth*. doi:10.1002/2016JB013677

Scholz, C. H., 1968. The frequency-magnitude relation of microfracturing in rock and its relation to earthquakes. *Bulletin of the Seismological Society of America*, **58**, 1, 399–415.

Seeber, L., Kim, W.Y., Armbruster, J. G., Du, W.X., Lerner-Lam, A., & Friberg, P., 2002. The 20 April 2002 Mw 5.0 Earthquake near Au Sable Forks, Adirondacks, New York: A First Glance at a New Sequence. *Seismological Research Letters*, **73**, 480–489.

Stein, S., & Wysession, M., 2003. An introduction to seismology, earthquakes, and earth structure. Malden, MA, Blackwell Pub.

Syracuse, E. M., Thurber, C. H., Rawles, C. J., Savage, M. K., & Bannister, S., 2013. High-resolution relocation of aftershocks of the Mw 7.1 Darfield, New Zealand, earthquake and implications for fault activity. *J. Geophys. Res.*, **118**, 4184–4195, doi:10.1002/jgrb.50301.

Urbancic, T. I., Trifu, C. I., Long, J. M., & Young, R. P., 1992. Space-time correlations of b values with stress release. *Pure and Applied Geophysics*, **139**, 3, 449–462.

Utsu, T., Ogata, Y., & Matsuura, R. S., 1995. The centenary of the Omori formula for a decay law of aftershock activity, *J. Phys. Earth*, **43**, 1–33.

Vlček, J., Fischer, T., & Vilhelm, J., 2015. Backprojection stacking of Pand Swaves to determine location and focal mechanism of microseismic events recorded by a surface array. *Geophysical Prospecting*, **64**, 6, 1428–1440.

Walker, K. T., & Shearer, P. M., 2009. Illuminating the nearsonic rupture velocities of the intracontinental Kokoxili Mw 7.8 and Denali fault Mw 7.9 strikeslip earthquakes with global P wave back projection imaging. *Journal of Geophysical Research: Solid Earth*, **114**, B2.

Wiemer, S., & Wyss, M., 1997. Mapping the frequency-magnitude distribution in asperities: An improved technique to calculate recurrence times. *Journal of Geophysical Research-All Series*, **102**, 15–115.

Wiemer, S. & Katsumata, K., 1999. Spatial variability of seismicity parameters in aftershock zones. *J. Geophys. Res.*, **104**, B6, 135–151.

Wiemer, S., & Wyss, M., 2000. Minimum magnitude of completeness in earthquake catalogs:

Examples from Alaska, the western United States, and Japan. *Bulletin of the Seismological Society of America*, **90**, 4, 859–869.

Wu, Q., Chapman, M. C. & Beale, J. N., 2015. The aftershock sequence of the 2011 Mineral, Virginia, earthquake: Temporal and spatial distribution, focal mechanisms, regional stress, and the role of Coulomb stress transfer. *Bulletin of the Seismological Society of America*, **105**, 5, 2521–2537

Xu, X., Wen, X., Yu, G., Chen, G., Klinger, Y., Hubbard, J., & Shaw, J., 2009. Coseismic reverse- and oblique-slip surface faulting generated by the 2008 Mw 7.9 Wenchuan earthquake, China. *Geology*, **37**, 6, 515–518.

Zhebel, O., & Eisner, L., 2012. Simultaneous microseismic event localization and source mechanism determination. *82nd SEG meeting*, Expanded Abstracts, 1–5.

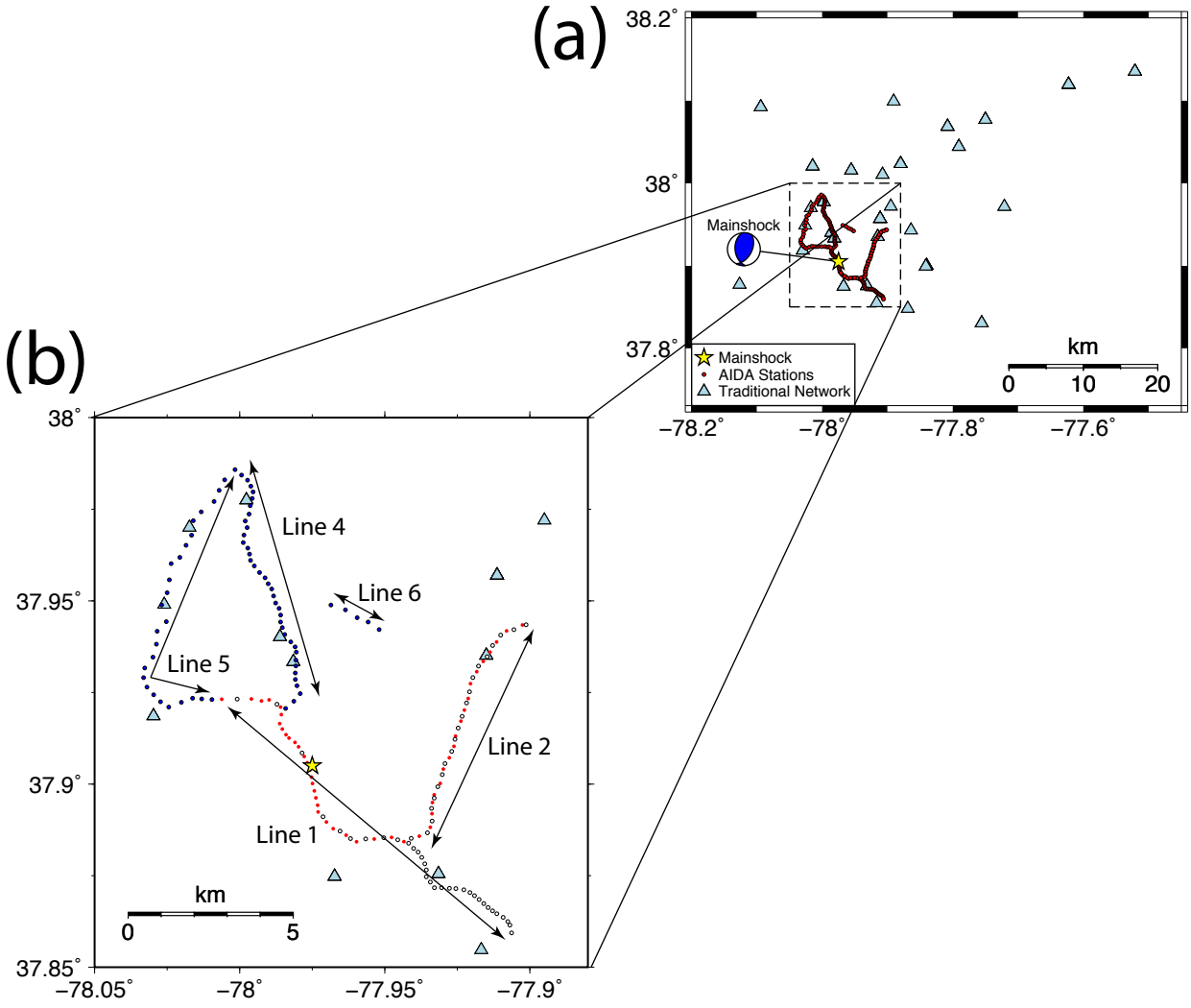

Figure 4.1: Maps of the 2011 Virginia earthquake and aftershock networks. (a) Map of traditional aftershock network (triangles), AIDA deployment (dots) and the 2011 Virginia earthquake epicenter (star). (b) Map of the AIDA deployment during the first 6 days (white), second 6 days (blue) and 12 days (red).

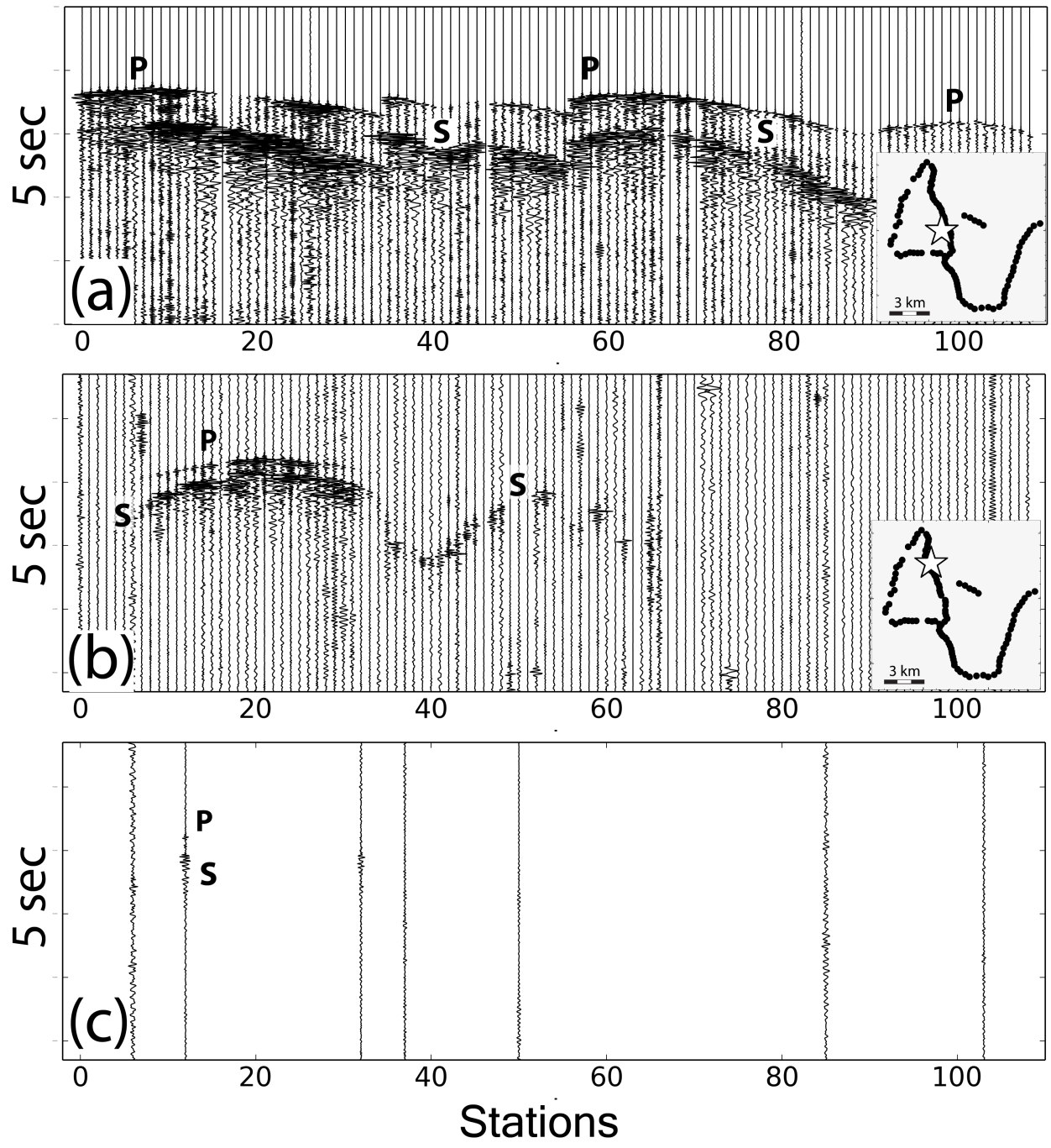

Figure 4.2: (a) AIDA data for a magnitude 1.7 aftershock recorded during the second week. Seismograms are sorted along the lines (Fig. 4.1). True relative amplitudes are shown after removal of the trace mean. Star indicates epicenter of the event at 4.2 km depth. (b) A magnitude –1.2 aftershock. Star indicates epicenter of the event at 1.5 km depth. (c) The aftershock of (b), plotting only stations near stations in the traditional aftershock network (triangles of Fig. 4.1).

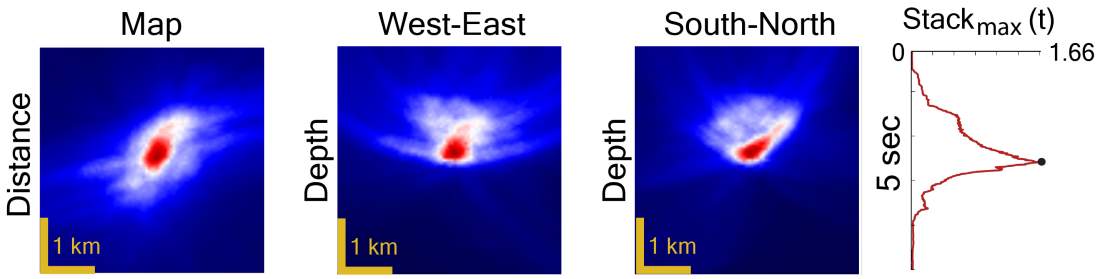

Figure 4.3: 4D backprojection images, plotted at the best hypocenter time and projected onto each 2D plane, plus a panel for the maximum stack value (black dot) as a function of time. Kurtosis backprojection for the large event of Fig. 4.2a.

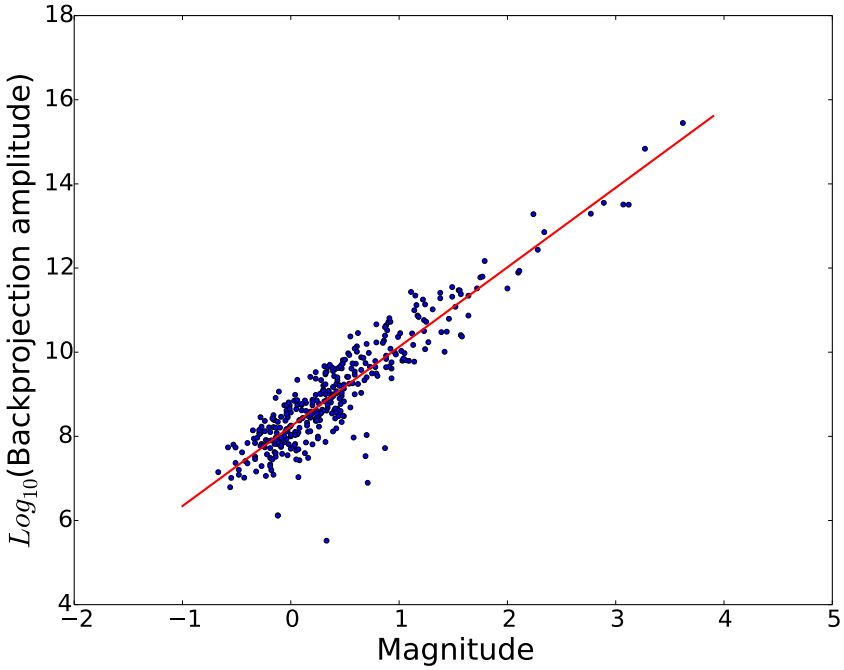

Figure 4.4: Base-10 logarithm of the backprojection image energy versus magnitude from the catalog of Wu et al. (2015).

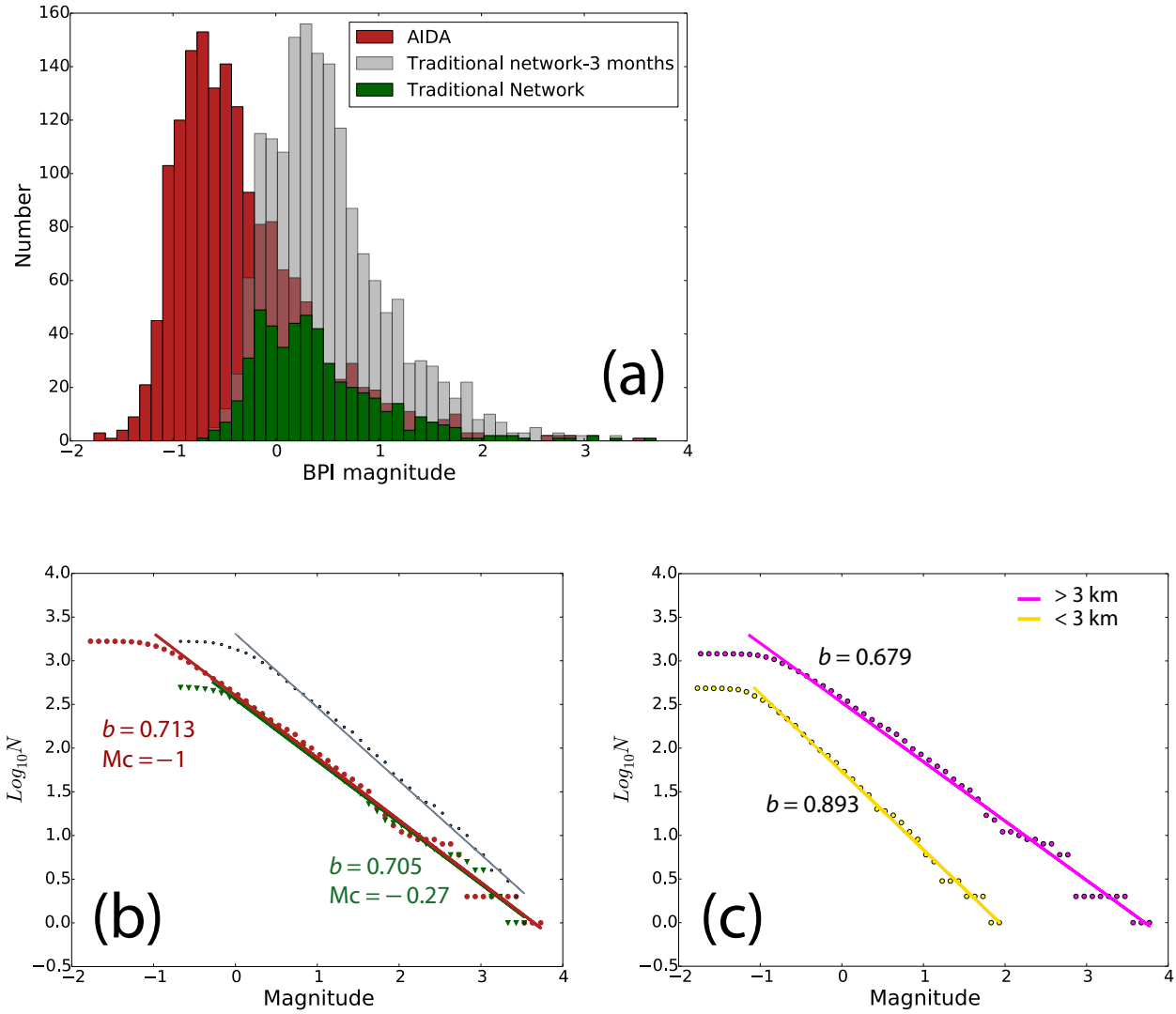

Figure 4.5: Number of earthquakes, N, versus magnitude. (a) Red is new backprojection catalog; green is traditional network catalog for the same 12 days from Wu et al. (2015); gray is the Wu et al. catalog for 4 months. (b) Gutenburg-Richter relationship. (c) Gutenburg-Richter relationship for backprojection catalog for events at depth < 3 km (yellow) and > 3 km (pink).

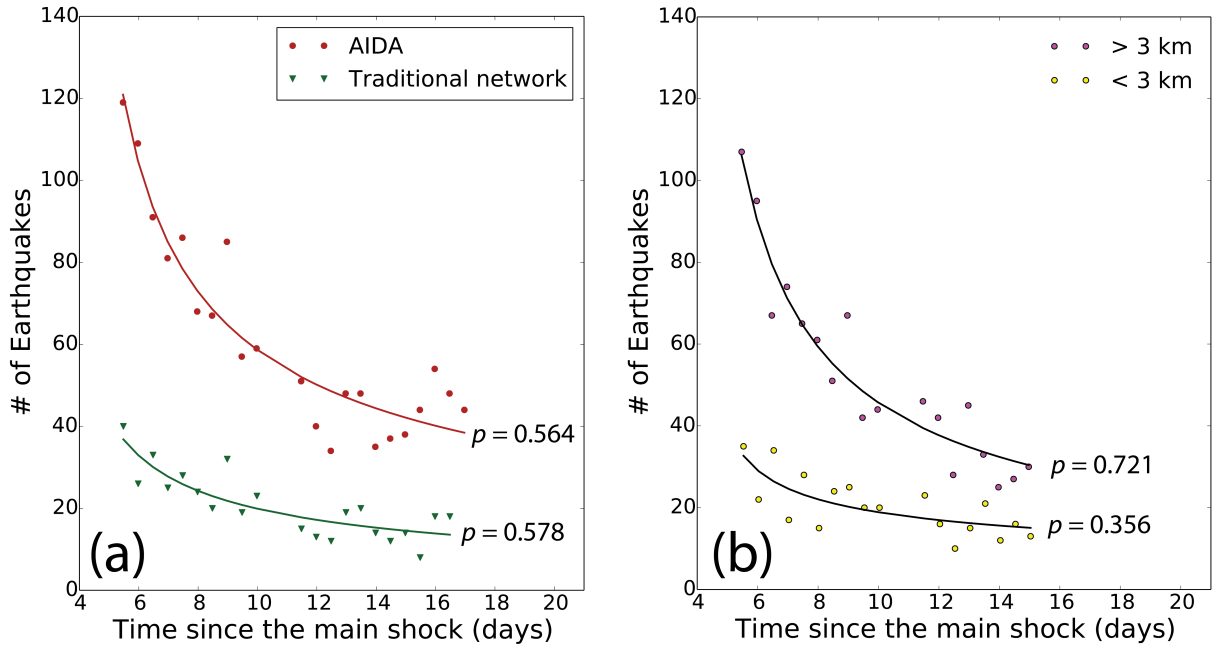

Figure 4.6: Number of aftershocks in each half-day window as a function of time, and best-fitting modified Omoris law decay curve and decay constant p". (a) Red is new back-projection catalog; green is traditional network catalog for the same 12 days from Wu et al. (2015). (b) Backprojection catalog for events at depth < 3 km (yellow) and > 3 km (pink).

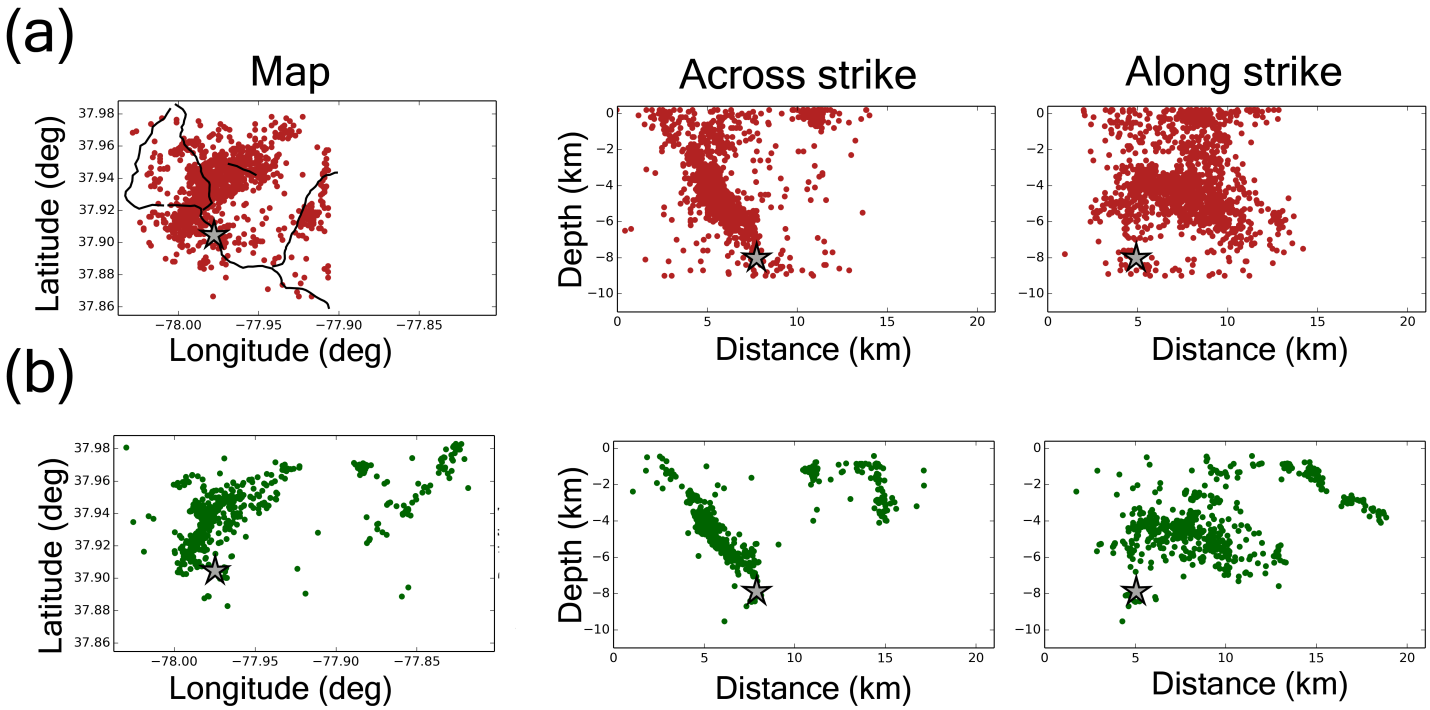

Figure 4.7: Map, across-strike section, and along-strike section for (a) backprojection catalog (red); (b) traditional network catalog (green) for the same 12 days from Wu et al. (2015). Strike is N33°E. Star indicates the main shock hypocenter. Stations (black) are shown on the map (a).

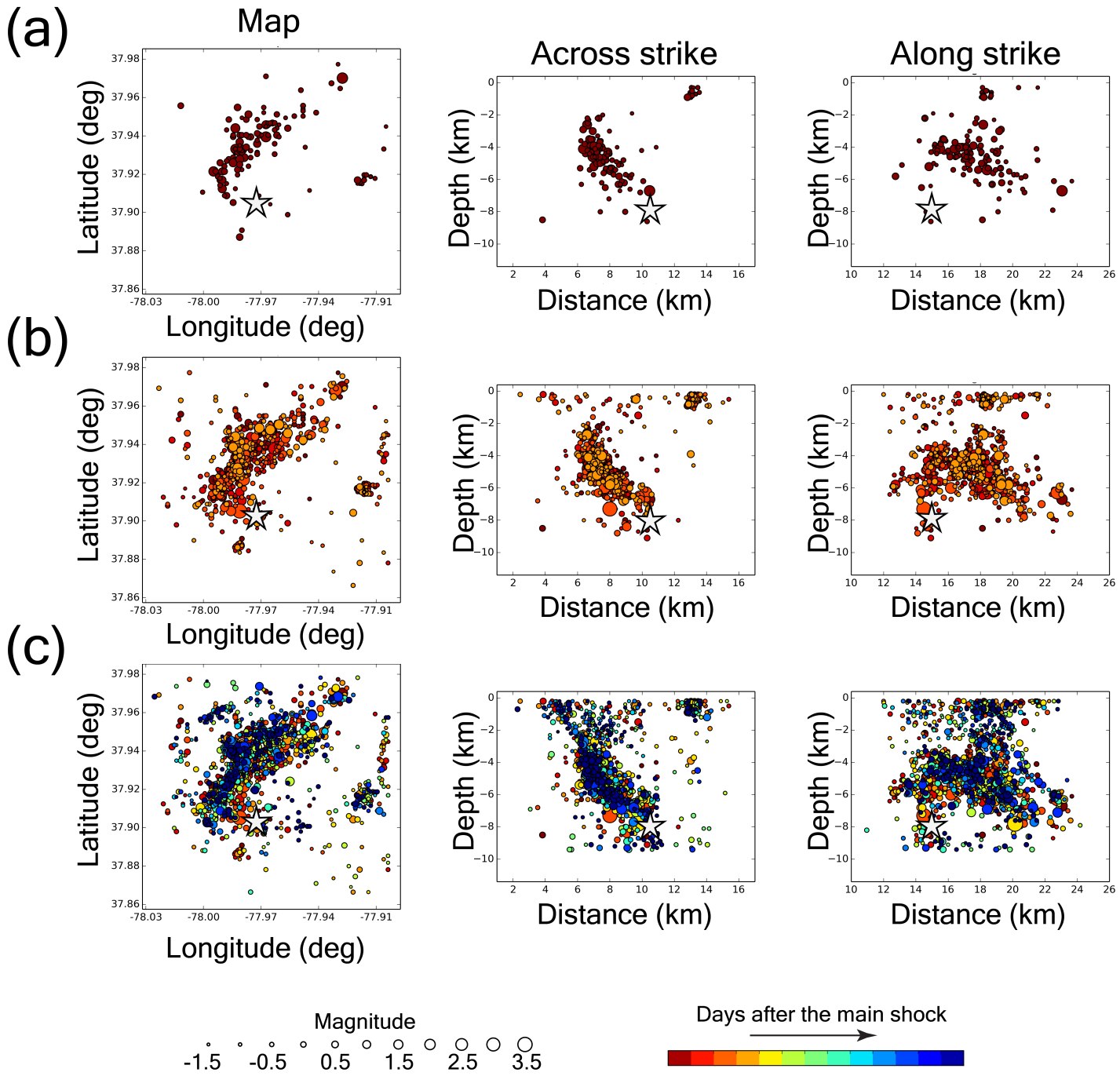

Figure 4.8: Map and cross-sections for the backprojection catalog, showing (a) day 5, (b) days 5-8, and (c) days 5-16 after the main shock. Red to blue colors show the event date. The hypocenters are scaled to magnitude. Star indicates the main shock hypocenter.

Appendix

The AIDA Backprojection Earthquake Catalog

Date (YYYY/MM/DD)	**Time (HH:MM:SS)**	**Latitude (°N)**	**Longitude (°E)**	**Depth (km)**	**Magnitude (M_{BPI})**
2011/08/27	19:20:35.60	37.917	-77.994	3.5	0.35
2011/08/27	19:23:02.15	37.920	-77.985	3.2	-0.38
2011/08/27	19:37:32.28	37.926	-77.984	3.5	0.05
2011/08/27	19:53:36.35	37.936	-77.975	5.0	0.83
2011/08/27	20:28:26.82	37.956	-77.951	5.4	-0.15
2011/08/27	21:20:52.80	37.936	-77.966	4.6	-0.26
2011/08/27	21:21:01.67	37.929	-77.982	3.6	1.10
2011/08/27	21:21:21.57	37.931	-77.985	4.2	-0.06
2011/08/27	21:27:33.05	37.928	-77.990	4.2	0.10
2011/08/27	21:29:34.36	37.931	-77.986	4.4	-0.27
2011/08/27	22:35:52.27	37.927	-77.991	5.0	-0.23
2011/08/27	22:38:27.57	37.891	-77.983	4.7	-0.25
2011/08/27	23:32:13.78	37.940	-77.965	5.9	0.47
2011/08/27	23:52:03.60	37.939	-77.970	5.0	1.89
2011/08/28	00:07:14.17	37.948	-77.990	4.9	0.12
2011/08/28	00:56:15.68	37.932	-77.978	3.7	-0.41
2011/08/28	00:56:58.13	37.946	-77.969	4.0	0.05
2011/08/28	00:58:12.47	37.951	-77.965	5.1	0.06
2011/08/28	01:03:26.54	37.926	-77.994	4.0	0.38
2011/08/28	01:07:54.74	37.934	-77.982	3.9	-0.50
2011/08/28	01:17:18.90	37.940	-77.984	3.1	0.11
2011/08/28	01:32:26.72	37.931	-77.975	4.0	-0.37
2011/08/28	01:48:08.02	37.929	-77.987	4.1	0.02
2011/08/28	02:18:22.84	37.912	-77.993	4.8	1.19
2011/08/28	02:40:36.89	37.920	-77.919	0.5	-0.37
2011/08/28	04:47:30.65	37.930	-77.975	2.6	-0.54
2011/08/28	05:15:58.10	37.932	-77.982	3.2	-0.36
2011/08/28	05:20:24.05	37.946	-77.970	3.9	1.14
2011/08/28	05:21:22.52	37.940	-77.974	4.4	0.32
2011/08/28	05:23:13.08	37.924	-77.980	4.2	-0.36
2011/08/28	05:23:14.13	37.922	-77.983	1.6	-0.60
2011/08/28	05:28:49.45	37.956	-78.015	8.1	0.24
2011/08/28	05:31:21.80	37.921	-77.992	3.9	-0.30
2011/08/28	05:42:49.93	37.944	-77.986	2.2	1.50
2011/08/28	05:50:58.01	37.948	-77.975	7.6	-0.38
2011/08/28	05:59:30.61	37.927	-77.986	3.8	0.79
2011/08/28	06:03:04.69	37.909	-77.991	1.8	0.44
2011/08/28	06:03:26.17	37.909	-77.992	1.8	-0.49
2011/08/28	06:04:42.45	37.933	-77.984	4.3	0.17
2011/08/28	06:05:52.51	37.933	-77.909	-0.1	-0.44

* z_0 = −0.4 km

The AIDA Backprojection Earthquake Catalog

Date (YYYY/MM/DD)	**Time (HH:MM:SS)**	**Latitude (°N)**	**Longitude (°E)**	**Depth (km)**	**Magnitude (M_{BPI})**
2011/08/28	06:52:27.55	37.939	-77.987	2.1	0.06
2011/08/28	07:27:08.38	37.911	-78.003	3.2	-0.46
2011/08/28	07:28:27.07	37.931	-77.986	5.3	-0.36
2011/08/28	07:30:59.37	37.941	-77.975	4.2	0.19
2011/08/28	08:01:14.64	37.915	-77.920	-0.1	-0.41
2011/08/28	08:01:26.10	37.915	-77.922	0.2	-0.70
2011/08/28	08:02:16.22	37.905	-77.987	6.1	0.30
2011/08/28	08:06:16.12	37.933	-77.983	4.6	0.72
2011/08/28	08:17:19.38	37.917	-77.993	3.8	0.92
2011/08/28	08:32:01.39	37.934	-77.981	4.4	0.52
2011/08/28	08:43:52.00	37.934	-77.950	3.8	-0.54
2011/08/28	08:48:17.23	37.922	-77.985	4.2	0.29
2011/08/28	09:04:53.99	37.947	-77.967	4.9	0.32
2011/08/28	09:05:11.67	37.929	-77.978	4.9	-0.28
2011/08/28	09:05:14.71	37.945	-77.974	5.2	0.03
2011/08/28	09:14:23.65	37.924	-77.992	3.8	-0.11
2011/08/28	09:15:21.49	37.944	-77.965	4.5	-0.43
2011/08/28	09:24:46.46	37.947	-77.966	5.3	-0.16
2011/08/28	09:25:34.27	37.938	-77.975	4.0	-0.43
2011/08/28	09:51:35.99	37.940	-77.973	4.1	-0.73
2011/08/28	09:59:32.31	37.899	-77.959	8.2	-0.33
2011/08/28	10:26:45.72	37.949	-77.983	1.9	-0.79
2011/08/28	10:45:05.29	37.916	-77.921	0.4	0.15
2011/08/28	10:50:00.77	37.946	-77.964	3.6	-0.79
2011/08/28	10:53:09.24	37.947	-77.969	6.8	-0.51
2011/08/28	11:06:51.60	37.919	-77.916	0.3	-0.59
2011/08/28	11:06:52.74	37.915	-77.923	0.5	-0.88
2011/08/28	11:09:22.39	37.918	-77.914	0.2	-0.54
2011/08/28	11:12:10.02	37.919	-77.916	0.3	-0.67
2011/08/28	11:12:18.96	37.919	-77.916	0.3	-0.91
2011/08/28	11:12:31.74	37.919	-77.916	0.3	-1.00
2011/08/28	11:21:58.59	37.921	-77.995	3.3	-0.66
2011/08/28	11:40:32.92	37.926	-77.987	3.7	1.17
2011/08/28	11:43:49.69	37.933	-77.986	4.2	1.59
2011/08/28	11:49:03.92	37.928	-77.984	3.6	1.09
2011/08/28	11:50:28.76	37.931	-77.985	4.1	0.15
2011/08/28	11:57:25.39	37.915	-77.991	3.4	-0.62
2011/08/28	11:58:06.87	37.932	-77.984	3.5	0.16
2011/08/28	12:01:57.60	37.977	-77.933	5.7	-0.73
2011/08/28	12:10:08.51	37.955	-77.985	2.5	0.56

* z_0 = −0.4 km

The AIDA Backprojection Earthquake Catalog

Date (YYYY/MM/DD)	**Time (HH:MM:SS)**	**Latitude (°N)**	**Longitude (°E)**	**Depth (km)**	**Magnitude (M_{BPI})**
2011/08/28	12:21:52.35	37.950	-77.956	5.3	-0.28
2011/08/28	12:24:42.70	37.920	-77.918	0.4	-0.30
2011/08/28	12:35:06.37	37.945	-77.970	3.9	-0.71
2011/08/28	12:39:10.07	37.943	-77.966	5.0	-0.26
2011/08/28	12:40:56.02	37.964	-77.952	4.4	-0.20
2011/08/28	12:50:23.36	37.931	-77.983	3.6	0.09
2011/08/28	12:51:34.91	37.940	-77.969	4.4	-0.28
2011/08/28	13:37:36.48	37.940	-77.983	3.7	-0.02
2011/08/28	13:39:13.99	37.912	-77.986	4.6	-0.57
2011/08/28	13:45:31.09	37.939	-77.978	4.6	0.41
2011/08/28	13:46:58.26	37.948	-77.981	3.1	0.21
2011/08/28	14:12:38.57	37.943	-77.991	5.9	-0.45
2011/08/28	14:14:02.94	37.930	-77.975	5.0	-0.14
2011/08/28	14:31:43.74	37.932	-77.983	2.9	-0.52
2011/08/28	14:31:54.29	37.965	-77.932	7.5	-0.34
2011/08/28	14:32:31.47	37.937	-77.984	3.5	0.89
2011/08/28	14:43:10.77	37.940	-77.987	1.8	-0.25
2011/08/28	14:43:22.82	37.921	-77.998	3.7	1.64
2011/08/28	15:10:08.66	37.921	-77.997	3.4	0.04
2011/08/28	15:27:46.31	37.912	-77.948	3.6	-0.72
2011/08/28	15:44:39.25	37.903	-77.974	7.6	-0.04
2011/08/28	16:15:34.69	37.887	-77.984	5.4	0.54
2011/08/28	16:24:36.46	37.933	-77.984	4.2	-0.03
2011/08/28	16:27:03.86	37.921	-77.993	3.1	0.79
2011/08/28	16:33:11.62	37.918	-77.919	0.1	-0.88
2011/08/28	16:34:33.25	37.967	-77.936	5.7	-0.12
2011/08/28	16:36:58.03	37.952	-77.944	6.4	-0.17
2011/08/28	16:43:35.27	37.919	-77.995	3.8	-0.11
2011/08/28	16:46:30.00	37.970	-77.931	6.3	2.08
2011/08/28	16:53:00.42	37.933	-77.986	4.2	-0.33
2011/08/28	17:07:23.92	37.954	-77.951	6.2	-0.49
2011/08/28	17:10:11.15	37.921	-77.992	3.1	0.34
2011/08/28	17:12:47.49	37.953	-77.951	5.5	-0.39
2011/08/28	17:14:36.48	37.945	-77.908	-0.1	-0.85
2011/08/28	17:24:18.42	37.951	-77.980	2.6	0.73
2011/08/28	17:37:00.72	37.917	-77.919	0.1	-0.14
2011/08/28	17:38:01.64	37.906	-77.976	6.0	-0.79
2011/08/28	17:38:03.13	37.904	-77.968	1.5	-0.89
2011/08/28	17:41:14.81	37.944	-77.959	5.8	0.43
2011/08/28	17:41:53.32	37.949	-77.960	6.3	-0.71

* z_0 = −0.4 km

The AIDA Backprojection Earthquake Catalog

Date (YYYY/MM/DD)	**Time (HH:MM:SS)**	**Latitude (°N)**	**Longitude (°E)**	**Depth (km)**	**Magnitude (M_{BPI})**
2011/08/28	17:56:06.30	37.925	-77.984	3.3	0.37
2011/08/28	17:56:17.05	37.909	-77.974	4.7	-0.95
2011/08/28	18:07:52.84	37.933	-77.986	3.9	-0.62
2011/08/28	18:12:09.87	37.939	-77.980	3.5	0.01
2011/08/28	18:18:08.86	37.940	-77.981	3.9	0.07
2011/08/28	18:23:17.63	37.947	-77.968	4.9	-0.36
2011/08/28	18:27:17.29	37.952	-77.972	4.5	-0.62
2011/08/28	18:29:11.55	37.955	-77.972	5.8	-0.38
2011/08/28	18:30:04.77	37.971	-77.970	3.7	-0.24
2011/08/28	18:35:03.82	37.935	-77.984	4.2	-0.74
2011/08/28	18:37:02.33	37.917	-77.923	0.5	0.56
2011/08/28	18:49:01.20	37.914	-77.994	3.9	-0.27
2011/08/28	18:50:42.30	37.918	-77.994	4.0	-0.47
2011/08/28	18:59:04.85	37.930	-77.966	5.7	-0.19
2011/08/28	19:11:27.71	37.939	-77.964	5.9	-0.46
2011/08/28	19:13:43.88	37.950	-77.951	5.3	-0.43
2011/08/28	19:26:25.75	37.939	-77.981	2.3	-0.73
2011/08/28	19:30:53.96	37.938	-77.962	5.7	0.28
2011/08/28	19:31:24.03	37.938	-77.966	5.9	-0.32
2011/08/28	19:32:21.23	37.914	-77.919	0.3	0.11
2011/08/28	19:41:35.88	37.938	-77.974	5.3	-0.01
2011/08/28	19:52:03.05	37.948	-77.945	7.0	-0.62
2011/08/28	20:18:05.53	37.938	-77.966	5.9	2.81
2011/08/28	20:21:42.94	37.953	-78.016	-0.2	-0.37
2011/08/28	20:38:36.14	37.933	-77.962	6.1	0.73
2011/08/28	20:41:01.83	37.931	-77.976	4.6	-0.06
2011/08/28	20:49:40.95	37.957	-77.953	5.9	-0.22
2011/08/28	21:03:50.38	37.942	-77.980	3.9	1.06
2011/08/28	21:07:02.23	37.933	-77.968	5.6	1.22
2011/08/28	21:09:32.49	37.930	-77.984	3.5	0.04
2011/08/28	21:09:46.15	37.911	-77.983	5.6	1.39
2011/08/28	21:10:38.87	37.911	-77.998	5.0	-0.56
2011/08/28	21:23:30.52	37.903	-77.970	7.7	-1.18
2011/08/28	21:36:19.77	37.949	-77.953	5.9	-0.53
2011/08/28	21:43:50.91	37.960	-77.951	5.3	-0.16
2011/08/28	21:49:53.22	37.916	-77.989	3.1	-0.91
2011/08/28	21:55:34.77	37.899	-77.959	8.7	0.17
2011/08/28	21:59:31.28	37.932	-77.982	4.4	-0.42
2011/08/28	22:06:01.16	37.947	-77.973	4.3	-0.07
2011/08/28	22:09:38.28	37.927	-77.995	3.7	-0.49

* z_0 = −0.4 km

The AIDA Backprojection Earthquake Catalog

Date (YYYY/MM/DD)	**Time (HH:MM:SS)**	**Latitude (°N)**	**Longitude (°E)**	**Depth (km)**	**Magnitude (M_{BPI})**
2011/08/28	22:57:53.45	37.945	-77.970	3.7	0.63
2011/08/28	23:08:21.24	37.918	-77.989	4.4	-0.56
2011/08/28	23:17:18.08	37.935	-77.983	4.1	-0.91
2011/08/28	23:19:20.26	37.913	-77.995	3.6	-0.91
2011/08/28	23:41:51.63	37.906	-77.997	5.1	-0.82
2011/08/28	23:45:38.06	37.946	-77.961	5.6	-1.09
2011/08/28	23:51:46.40	37.913	-77.992	3.8	-0.58
2011/08/28	23:53:25.69	37.946	-77.969	4.3	-0.38
2011/08/28	23:59:50.05	37.939	-77.987	3.4	0.14
2011/08/29	00:00:14.44	37.932	-77.982	3.1	-1.21
2011/08/29	00:05:19.82	37.959	-77.913	7.6	-0.71
2011/08/29	00:11:12.35	37.919	-77.917	0.5	-0.06
2011/08/29	00:12:39.27	37.933	-77.983	4.4	-0.96
2011/08/29	00:17:10.65	37.914	-77.994	3.9	-0.99
2011/08/29	00:20:10.16	37.919	-77.916	0.2	-1.09
2011/08/29	00:20:30.38	37.968	-77.934	6.1	0.26
2011/08/29	00:23:55.55	37.909	-77.990	5.9	0.73
2011/08/29	00:33:36.12	37.915	-77.989	3.6	-0.77
2011/08/29	00:41:17.00	37.898	-77.978	8.1	-0.93
2011/08/29	00:50:49.48	37.898	-78.017	0.6	-0.38
2011/08/29	00:58:15.13	37.927	-77.987	4.1	-0.50
2011/08/29	01:01:14.11	37.912	-77.999	4.2	-1.02
2011/08/29	01:02:44.92	37.926	-77.987	3.6	-0.96
2011/08/29	01:04:39.51	37.953	-77.945	1.1	0.67
2011/08/29	01:06:36.22	37.938	-77.985	3.9	2.67
2011/08/29	01:32:44.64	37.945	-77.907	0.0	-0.80
2011/08/29	01:42:58.14	37.908	-77.997	4.9	-0.87
2011/08/29	01:49:29.70	37.915	-77.995	3.8	-1.04
2011/08/29	01:50:51.93	37.939	-77.986	4.1	-0.08
2011/08/29	01:57:30.48	37.940	-77.985	2.8	0.11
2011/08/29	01:58:09.98	37.925	-77.989	3.7	-0.14
2011/08/29	02:01:04.05	37.912	-77.999	4.5	0.84
2011/08/29	02:07:39.59	37.943	-77.978	3.7	-1.01
2011/08/29	02:08:28.43	37.922	-77.995	3.4	-0.91
2011/08/29	02:08:34.49	37.942	-77.985	3.5	-0.78
2011/08/29	02:09:28.66	37.910	-78.005	4.8	-0.28
2011/08/29	02:11:33.42	37.941	-77.983	3.5	-1.22
2011/08/29	02:14:19.15	37.948	-77.969	4.6	-0.19
2011/08/29	02:14:52.03	37.923	-77.985	4.7	-0.98
2011/08/29	02:16:51.66	37.938	-77.984	3.9	0.78

* z_0 = −0.4 km

The AIDA Backprojection Earthquake Catalog

Date (YYYY/MM/DD)	**Time (HH:MM:SS)**	**Latitude (°N)**	**Longitude (°E)**	**Depth (km)**	**Magnitude (M_{BPI})**
2011/08/29	02:19:03.80	37.924	-77.984	3.8	-1.10
2011/08/29	02:30:49.65	37.916	-77.918	0.0	-0.49
2011/08/29	02:32:05.30	37.927	-77.975	5.3	0.06
2011/08/29	02:39:16.26	37.903	-78.001	4.9	-0.86
2011/08/29	02:45:57.43	37.945	-77.975	3.0	-0.57
2011/08/29	02:53:31.14	37.939	-78.011	0.3	0.27
2011/08/29	02:56:56.87	37.915	-77.918	-0.2	-1.42
2011/08/29	03:03:47.67	37.932	-77.984	3.8	-0.22
2011/08/29	03:05:10.61	37.940	-77.983	4.5	-0.91
2011/08/29	03:09:17.12	37.916	-77.917	0.2	-1.17
2011/08/29	03:09:29.63	37.886	-77.986	5.5	0.10
2011/08/29	03:11:47.65	37.921	-77.990	4.3	-0.04
2011/08/29	03:15:21.67	37.938	-77.985	4.0	2.81
2011/08/29	03:16:51.56	37.939	-77.987	4.4	2.79
2011/08/29	03:18:59.13	37.939	-77.986	4.0	0.92
2011/08/29	03:21:39.66	37.930	-77.967	5.7	0.17
2011/08/29	03:23:52.04	37.938	-77.986	4.0	0.67
2011/08/29	03:24:18.72	37.938	-77.985	4.0	0.99
2011/08/29	03:25:04.43	37.939	-77.985	4.2	1.05
2011/08/29	03:25:18.65	37.937	-77.984	4.0	-0.32
2011/08/29	03:26:00.97	37.938	-77.986	4.0	-0.40
2011/08/29	03:28:04.77	37.939	-77.987	4.0	-0.77
2011/08/29	03:37:21.93	37.937	-77.985	3.9	1.71
2011/08/29	03:38:15.79	37.887	-77.984	5.4	1.61
2011/08/29	03:39:49.40	37.926	-77.985	4.1	-0.08
2011/08/29	03:41:04.76	37.924	-77.985	3.7	0.44
2011/08/29	03:44:20.32	37.936	-77.976	5.0	-0.75
2011/08/29	03:52:12.65	37.917	-77.917	0.0	-0.42
2011/08/29	03:52:24.31	37.957	-77.957	6.3	-0.68
2011/08/29	03:52:26.19	37.933	-77.976	0.2	-0.96
2011/08/29	03:56:36.90	37.938	-77.986	4.0	-0.61
2011/08/29	03:57:18.13	37.912	-78.008	2.1	-1.20
2011/08/29	03:59:41.85	37.928	-77.986	4.3	-1.16
2011/08/29	04:00:49.15	37.878	-77.907	0.1	-0.64
2011/08/29	04:05:37.47	37.929	-77.989	5.3	-0.87
2011/08/29	04:05:38.75	37.924	-77.982	0.4	-0.89
2011/08/29	04:07:39.96	37.939	-77.970	4.6	-0.77
2011/08/29	04:19:26.45	37.938	-77.983	4.0	2.44
2011/08/29	04:22:25.30	37.942	-77.977	4.2	-0.42
2011/08/29	04:36:19.59	37.939	-77.987	4.0	0.12

* z_0 = −0.4 km

The AIDA Backprojection Earthquake Catalog

Date (YYYY/MM/DD)	**Time (HH:MM:SS)**	**Latitude (°N)**	**Longitude (°E)**	**Depth (km)**	**Magnitude (M_{BPI})**
2011/08/29	04:40:01.01	37.941	-77.965	5.5	-0.60
2011/08/29	04:47:44.06	37.918	-77.992	3.7	0.51
2011/08/29	04:52:49.42	37.887	-77.984	5.8	-1.07
2011/08/29	04:52:50.78	37.896	-77.975	1.1	-1.16
2011/08/29	04:55:25.56	37.920	-77.917	0.5	-1.10
2011/08/29	05:03:33.67	37.938	-77.986	4.3	0.70
2011/08/29	05:06:52.69	37.912	-78.014	3.6	-0.85
2011/08/29	05:09:09.36	37.951	-77.974	2.1	-1.08
2011/08/29	05:20:20.63	37.930	-77.983	4.3	1.27
2011/08/29	05:24:21.05	37.968	-77.940	8.3	-0.88
2011/08/29	05:34:53.70	37.917	-78.013	3.3	-1.08
2011/08/29	05:41:43.17	37.938	-77.985	4.3	1.34
2011/08/29	05:43:06.68	37.949	-77.952	5.4	-0.90
2011/08/29	05:53:08.91	37.926	-77.972	5.3	-0.38
2011/08/29	06:05:39.76	37.884	-77.986	6.0	-0.76
2011/08/29	06:08:40.57	37.925	-77.974	4.9	-0.87
2011/08/29	06:20:07.70	37.946	-77.973	4.3	-0.34
2011/08/29	06:20:14.45	37.943	-77.965	5.1	0.50
2011/08/29	06:40:00.22	37.939	-77.989	4.1	0.08
2011/08/29	06:53:04.95	37.915	-77.998	4.6	0.34
2011/08/29	06:55:38.36	37.906	-77.980	6.9	-0.77
2011/08/29	07:00:01.08	37.924	-77.992	2.9	-1.00
2011/08/29	07:04:37.02	37.931	-77.981	4.4	-0.91
2011/08/29	07:05:59.11	37.912	-77.980	5.7	-0.74
2011/08/29	07:13:30.29	37.939	-77.987	4.2	0.65
2011/08/29	07:35:01.80	37.945	-77.965	4.7	-0.05
2011/08/29	07:38:46.28	37.919	-77.994	4.1	1.46
2011/08/29	07:49:10.73	37.939	-77.976	3.3	-0.69
2011/08/29	07:52:08.97	37.918	-78.002	5.1	-0.62
2011/08/29	07:56:32.29	37.939	-77.959	4.7	-0.77
2011/08/29	08:04:11.54	37.947	-77.970	4.3	-0.95
2011/08/29	08:09:47.56	37.943	-77.953	6.1	0.27
2011/08/29	08:20:00.00	37.938	-77.980	5.0	-0.80
2011/08/29	08:27:45.28	37.933	-77.986	3.9	-0.48
2011/08/29	08:28:37.69	37.939	-77.989	4.1	0.40
2011/08/29	08:30:22.95	37.944	-77.977	4.6	-0.49
2011/08/29	08:37:56.25	37.915	-77.922	0.5	-1.16
2011/08/29	08:43:52.05	37.935	-77.962	5.7	0.00
2011/08/29	08:44:37.90	37.919	-77.918	-0.1	-1.33
2011/08/29	08:45:35.14	37.926	-77.984	4.4	0.30

* z_0 = −0.4 km

The AIDA Backprojection Earthquake Catalog

Date (YYYY/MM/DD)	**Time (HH:MM:SS)**	**Latitude (°N)**	**Longitude (°E)**	**Depth (km)**	**Magnitude (M_{BPI})**
2011/08/29	08:50:53.23	37.948	-77.984	4.2	-0.48
2011/08/29	08:56:33.38	37.935	-77.983	4.1	-0.62
2011/08/29	09:03:54.69	37.932	-77.985	4.2	-0.46
2011/08/29	09:05:33.39	37.951	-77.976	3.7	-0.45
2011/08/29	09:06:01.10	37.931	-77.983	3.7	-0.49
2011/08/29	09:07:25.10	37.948	-77.966	5.1	-0.66
2011/08/29	09:13:17.77	37.915	-77.998	4.3	-0.17
2011/08/29	09:16:58.50	37.923	-77.990	3.2	-0.91
2011/08/29	09:17:29.52	37.949	-77.933	4.5	-0.46
2011/08/29	09:17:39.02	37.950	-77.940	7.2	-0.43
2011/08/29	09:25:21.99	37.929	-77.972	4.5	-0.59
2011/08/29	09:27:06.36	37.914	-77.918	-0.1	-0.21
2011/08/29	09:38:41.81	37.946	-77.967	5.0	0.93
2011/08/29	09:41:45.93	37.910	-77.972	1.0	-0.86
2011/08/29	09:43:02.53	37.953	-77.962	5.2	-0.85
2011/08/29	09:49:10.69	37.941	-77.981	3.5	0.68
2011/08/29	10:05:08.21	37.949	-77.967	5.2	0.15
2011/08/29	10:16:04.55	37.887	-77.986	5.8	-0.83
2011/08/29	10:18:50.57	37.938	-77.985	3.8	0.07
2011/08/29	10:21:08.57	37.927	-77.978	5.5	-0.71
2011/08/29	10:22:37.00	37.922	-77.993	3.1	-0.17
2011/08/29	10:24:33.93	37.918	-77.989	4.1	0.59
2011/08/29	10:33:13.64	37.922	-77.994	3.0	-0.28
2011/08/29	10:52:00.45	37.936	-77.985	4.1	-0.07
2011/08/29	10:56:04.04	37.941	-77.982	3.6	0.11
2011/08/29	10:59:10.35	37.916	-77.920	0.2	1.04
2011/08/29	10:59:51.46	37.916	-77.920	-0.1	1.03
2011/08/29	11:00:04.24	37.915	-77.918	-0.2	0.02
2011/08/29	11:00:35.64	37.916	-77.923	0.2	-0.99
2011/08/29	11:00:42.83	37.915	-77.918	-0.1	0.26
2011/08/29	11:01:12.63	37.914	-77.916	-0.2	-0.07
2011/08/29	11:03:10.62	37.916	-77.920	-0.2	0.14
2011/08/29	11:07:13.52	37.915	-77.918	-0.1	-1.08
2011/08/29	11:15:51.09	37.970	-77.946	6.0	-0.53
2011/08/29	11:16:25.97	37.950	-77.961	5.2	-0.40
2011/08/29	11:17:52.89	37.917	-77.919	0.0	-0.53
2011/08/29	11:18:08.33	37.913	-77.994	3.7	-0.09
2011/08/29	11:18:57.65	37.932	-77.973	4.6	-0.37
2011/08/29	11:21:13.88	37.958	-77.986	0.2	-0.20
2011/08/29	11:24:57.99	37.884	-77.980	4.8	-0.61

* z_0 = −0.4 km

The AIDA Backprojection Earthquake Catalog

Date (YYYY/MM/DD)	**Time (HH:MM:SS)**	**Latitude (°N)**	**Longitude (°E)**	**Depth (km)**	**Magnitude (M_{BPI})**
2011/08/29	11:25:24.34	37.939	-77.986	4.7	-0.54
2011/08/29	11:32:34.28	37.940	-77.985	3.6	-0.67
2011/08/29	11:41:25.52	37.918	-77.920	-0.1	-0.01
2011/08/29	11:45:49.34	37.913	-77.986	5.3	-0.33
2011/08/29	11:47:53.51	37.914	-77.989	5.0	0.36
2011/08/29	12:00:55.82	37.914	-77.983	7.0	-0.51
2011/08/29	12:00:57.33	37.907	-77.985	1.9	-0.60
2011/08/29	12:02:58.00	37.941	-77.985	4.9	-0.55
2011/08/29	12:06:32.76	37.940	-77.981	4.2	-0.63
2011/08/29	12:21:44.77	37.916	-77.998	3.2	-0.04
2011/08/29	12:43:41.48	37.938	-77.985	4.1	-0.59
2011/08/29	12:50:15.46	37.915	-77.984	5.2	1.31
2011/08/29	12:55:09.49	37.931	-77.985	4.1	0.70
2011/08/29	13:04:19.86	37.942	-77.992	3.9	-0.22
2011/08/29	13:09:53.86	37.948	-77.982	2.3	-0.48
2011/08/29	13:17:21.96	37.919	-77.915	0.2	-0.33
2011/08/29	13:19:43.39	37.918	-77.993	4.2	-0.53
2011/08/29	13:32:33.53	37.919	-77.912	-0.1	-0.56
2011/08/29	13:36:11.74	37.952	-77.973	3.5	-0.53
2011/08/29	13:50:20.74	37.915	-77.997	3.1	-0.28
2011/08/29	13:53:08.22	37.925	-77.993	3.8	-0.38
2011/08/29	14:01:11.14	37.947	-77.973	4.9	-0.01
2011/08/29	14:01:20.96	37.937	-77.986	3.7	-0.35
2011/08/29	14:33:38.21	37.912	-78.024	-0.2	-0.52
2011/08/29	14:46:44.36	37.953	-77.984	2.4	-0.59
2011/08/29	14:47:43.08	37.931	-77.974	5.5	-0.22
2011/08/29	14:48:13.08	37.948	-77.978	3.9	-0.50
2011/08/29	15:08:50.73	37.922	-77.997	3.5	-0.31
2011/08/29	15:23:21.38	37.908	-78.022	4.4	-0.31
2011/08/29	15:32:42.54	37.917	-77.920	-0.1	0.10
2011/08/29	15:32:49.13	37.942	-78.019	-0.2	0.34
2011/08/29	15:38:00.60	37.939	-77.965	5.4	-0.15
2011/08/29	15:46:56.44	37.918	-77.987	4.4	-0.54
2011/08/29	15:48:20.30	37.930	-77.969	5.7	-0.28
2011/08/29	16:06:04.13	37.935	-77.908	-0.1	0.06
2011/08/29	16:16:17.55	37.955	-77.957	7.2	-0.03
2011/08/29	16:23:17.13	37.944	-77.978	4.7	1.38
2011/08/29	16:31:08.26	37.941	-77.974	3.4	-0.36
2011/08/29	16:35:17.68	37.948	-77.967	5.8	-0.05
2011/08/29	16:48:02.39	37.923	-78.005	5.3	-0.40

* z_0 = −0.4 km

The AIDA Backprojection Earthquake Catalog

Date (YYYY/MM/DD)	**Time (HH:MM:SS)**	**Latitude (°N)**	**Longitude (°E)**	**Depth (km)**	**Magnitude (M_{BPI})**
2011/08/29	16:52:35.28	37.931	-77.974	5.3	-0.35
2011/08/29	16:58:17.21	37.970	-77.934	6.0	-0.55
2011/08/29	16:59:40.79	37.916	-77.997	4.4	0.60
2011/08/29	17:12:43.23	37.916	-78.003	3.1	0.38
2011/08/29	17:22:15.57	37.931	-77.909	-0.1	0.27
2011/08/29	17:35:33.94	37.967	-77.956	5.0	-0.08
2011/08/29	17:49:33.42	37.936	-77.984	3.8	-0.21
2011/08/29	17:51:41.63	37.940	-77.982	3.5	0.12
2011/08/29	18:05:33.50	37.939	-77.986	4.0	0.73
2011/08/29	18:11:44.54	37.933	-77.969	4.8	-0.49
2011/08/29	18:20:49.15	37.912	-77.997	3.9	0.67
2011/08/29	18:40:15.53	37.936	-77.911	-0.2	-0.40
2011/08/29	18:45:46.89	37.894	-77.993	5.1	-0.61
2011/08/29	18:45:48.04	37.900	-77.986	0.1	-0.45
2011/08/29	18:50:28.54	37.942	-77.976	4.0	-0.19
2011/08/29	19:09:18.09	37.917	-77.920	0.1	-0.42
2011/08/29	19:10:52.80	37.937	-77.992	4.8	-0.62
2011/08/29	19:21:00.59	37.912	-77.998	4.4	0.48
2011/08/29	19:26:08.20	37.912	-77.998	4.3	-0.33
2011/08/29	19:28:35.07	37.950	-77.968	5.8	-0.36
2011/08/29	19:29:23.47	37.926	-77.984	5.0	-0.53
2011/08/29	19:31:46.39	37.934	-77.984	4.5	-0.78
2011/08/29	19:34:22.32	37.920	-77.977	6.3	-0.44
2011/08/29	19:34:23.84	37.918	-77.973	0.8	-0.55
2011/08/29	19:39:26.80	37.905	-77.997	1.2	-0.20
2011/08/29	19:40:54.81	37.924	-77.986	4.4	0.04
2011/08/29	19:58:29.22	37.933	-77.980	2.9	-0.77
2011/08/29	20:06:01.05	37.957	-77.953	5.7	-0.02
2011/08/29	20:10:41.60	37.904	-77.993	5.2	-0.33
2011/08/29	20:13:47.48	37.930	-77.980	4.8	-0.56
2011/08/29	20:14:28.55	37.935	-77.977	5.2	-0.42
2011/08/29	20:29:35.18	37.942	-77.981	3.8	-0.59
2011/08/29	20:32:26.17	37.938	-77.978	4.1	0.90
2011/08/29	20:41:32.31	37.930	-77.984	4.4	-0.56
2011/08/29	21:09:33.41	37.940	-77.960	6.5	-0.19
2011/08/29	21:31:02.00	37.940	-77.962	6.0	-0.03
2011/08/29	21:37:32.64	37.915	-77.917	0.3	-0.21
2011/08/29	21:42:34.98	37.914	-77.997	4.3	-0.60
2011/08/29	21:50:08.04	37.917	-77.982	6.2	0.01
2011/08/29	22:06:35.60	37.937	-77.965	6.0	-0.56

* z_0 = −0.4 km

The AIDA Backprojection Earthquake Catalog

Date (YYYY/MM/DD)	**Time (HH:MM:SS)**	**Latitude (°N)**	**Longitude (°E)**	**Depth (km)**	**Magnitude (M_{BPI})**
2011/08/29	22:13:02.08	37.950	-77.974	3.1	0.01
2011/08/29	22:20:18.67	37.977	-78.010	6.4	-0.49
2011/08/29	22:29:40.34	37.919	-77.993	3.8	0.69
2011/08/29	22:35:09.95	37.934	-77.982	3.1	-0.68
2011/08/29	23:02:20.24	37.938	-77.986	4.0	-0.10
2011/08/29	23:36:29.04	37.924	-77.990	5.0	0.03
2011/08/29	23:36:53.92	37.942	-77.983	3.7	0.62
2011/08/29	23:39:50.41	37.968	-77.934	5.9	2.67
2011/08/29	23:48:56.90	37.931	-77.983	3.9	-0.99
2011/08/30	00:21:27.54	37.943	-77.910	-0.2	-1.02
2011/08/30	00:26:26.03	37.930	-77.973	6.3	-0.78
2011/08/30	00:29:38.58	37.946	-78.011	0.0	0.30
2011/08/30	00:33:30.84	37.938	-77.983	3.8	-0.73
2011/08/30	00:33:52.31	37.889	-77.947	0.3	-1.12
2011/08/30	00:35:22.93	37.939	-77.964	5.6	-0.44
2011/08/30	00:42:49.21	37.942	-77.982	4.4	-0.51
2011/08/30	00:43:35.37	37.921	-77.992	3.3	0.10
2011/08/30	00:49:53.81	37.935	-77.985	3.9	0.12
2011/08/30	00:50:08.03	37.951	-77.940	6.3	0.28
2011/08/30	00:52:46.45	37.902	-77.999	5.1	-0.28
2011/08/30	00:53:00.28	37.902	-77.999	5.1	-0.09
2011/08/30	00:56:31.43	37.917	-77.997	4.7	-0.68
2011/08/30	01:02:18.80	37.936	-77.972	5.3	-0.54
2011/08/30	01:04:16.74	37.940	-77.990	2.5	-0.76
2011/08/30	01:05:16.96	37.935	-77.961	5.2	0.58
2011/08/30	01:07:00.65	37.945	-77.989	2.4	-0.12
2011/08/30	01:08:51.68	37.921	-77.994	3.1	0.68
2011/08/30	01:12:21.31	37.958	-77.986	2.8	-0.22
2011/08/30	01:30:38.20	37.918	-77.991	3.9	-0.61
2011/08/30	01:38:14.61	37.952	-77.956	6.4	-0.73
2011/08/30	01:43:05.54	37.906	-78.002	4.9	-0.28
2011/08/30	01:45:42.34	37.945	-77.948	6.1	1.87
2011/08/30	01:51:16.99	37.913	-77.994	4.1	0.32
2011/08/30	01:52:14.61	37.932	-77.970	6.1	-0.55
2011/08/30	01:58:50.14	37.934	-77.982	3.9	-0.51
2011/08/30	02:00:00.65	37.917	-77.993	3.6	-0.03
2011/08/30	02:01:56.70	37.937	-77.984	3.9	-0.01
2011/08/30	02:13:44.20	37.912	-77.983	6.6	-0.53
2011/08/30	02:14:41.53	37.935	-77.981	4.2	0.74
2011/08/30	02:34:15.02	37.920	-77.990	4.2	-0.02

* z_0 = −0.4 km

The AIDA Backprojection Earthquake Catalog

Date (YYYY/MM/DD)	**Time (HH:MM:SS)**	**Latitude (°N)**	**Longitude (°E)**	**Depth (km)**	**Magnitude (M_{BPI})**
2011/08/30	02:35:33.13	37.934	-77.962	5.0	-0.48
2011/08/30	02:44:36.93	37.919	-77.919	0.6	-1.08
2011/08/30	02:49:19.43	37.935	-77.984	5.4	-0.97
2011/08/30	02:57:23.75	37.950	-77.978	2.4	-0.91
2011/08/30	03:02:20.33	37.951	-77.999	5.9	-0.81
2011/08/30	03:02:20.89	37.937	-77.978	2.8	-0.97
2011/08/30	03:03:00.74	37.935	-77.977	5.2	-0.25
2011/08/30	03:04:16.40	37.940	-77.984	5.0	-0.37
2011/08/30	03:14:25.01	37.929	-77.967	5.9	-0.06
2011/08/30	03:43:22.05	37.918	-77.999	3.2	0.12
2011/08/30	03:48:28.81	37.905	-77.984	6.9	3.49
2011/08/30	03:56:52.81	37.921	-77.989	3.8	-0.59
2011/08/30	03:59:28.76	37.919	-77.915	0.2	-0.48
2011/08/30	04:03:00.30	37.954	-77.962	4.8	-0.50
2011/08/30	04:12:48.96	37.918	-77.997	2.9	-0.10
2011/08/30	04:13:42.69	37.914	-77.999	4.6	0.08
2011/08/30	04:23:35.31	37.915	-77.919	-0.1	-1.08
2011/08/30	04:29:51.14	37.905	-77.989	5.7	1.69
2011/08/30	05:02:59.98	37.969	-77.934	5.7	-0.07
2011/08/30	05:09:00.91	37.927	-77.990	4.1	-0.55
2011/08/30	05:18:04.94	37.938	-77.985	3.9	1.30
2011/08/30	05:31:32.18	37.947	-77.972	4.4	-0.94
2011/08/30	05:32:24.55	37.939	-77.986	3.9	0.18
2011/08/30	05:33:36.52	37.962	-77.942	6.6	0.76
2011/08/30	05:40:51.35	37.917	-77.918	0.3	-1.31
2011/08/30	05:48:14.31	37.932	-77.985	4.4	-0.63
2011/08/30	05:54:57.16	37.939	-77.972	5.9	-1.28
2011/08/30	05:55:42.96	37.942	-77.967	5.2	-0.21
2011/08/30	06:01:10.34	37.887	-77.941	-0.2	-0.88
2011/08/30	06:11:32.45	37.921	-77.991	3.2	-1.16
2011/08/30	06:20:45.76	37.948	-77.962	4.7	-1.04
2011/08/30	06:25:32.14	37.917	-77.993	3.9	0.20
2011/08/30	06:30:07.13	37.959	-77.946	7.2	-0.94
2011/08/30	06:31:09.80	37.931	-77.989	4.7	-0.86
2011/08/30	06:32:04.48	37.916	-77.917	0.4	-0.67
2011/08/30	06:36:58.09	37.955	-77.970	4.4	-0.31
2011/08/30	06:39:46.92	37.953	-77.959	5.1	-0.46
2011/08/30	06:51:20.14	37.909	-78.022	5.0	-0.61
2011/08/30	07:03:10.58	37.932	-77.973	4.7	-1.03
2011/08/30	07:03:30.72	37.944	-77.976	4.4	1.04

* z_0 = −0.4 km

The AIDA Backprojection Earthquake Catalog

Date (YYYY/MM/DD)	**Time (HH:MM:SS)**	**Latitude (°N)**	**Longitude (°E)**	**Depth (km)**	**Magnitude (M_{BPI})**
2011/08/30	07:10:49.00	37.900	-77.981	8.4	0.18
2011/08/30	07:11:33.06	37.919	-77.914	0.1	-1.07
2011/08/30	07:17:04.41	37.944	-77.949	6.0	-0.76
2011/08/30	07:17:40.68	37.929	-77.983	3.9	-0.53
2011/08/30	07:35:07.56	37.901	-77.975	7.8	0.05
2011/08/30	07:44:21.18	37.951	-77.968	3.6	-0.57
2011/08/30	07:52:53.26	37.937	-77.984	4.5	-0.79
2011/08/30	08:00:48.37	37.915	-77.964	0.2	-1.07
2011/08/30	08:16:58.77	37.912	-77.911	-0.2	-0.66
2011/08/30	08:21:45.77	37.927	-77.973	3.3	-1.15
2011/08/30	08:22:30.89	37.919	-77.918	0.6	-0.32
2011/08/30	08:24:26.66	37.917	-77.993	3.6	-0.23
2011/08/30	08:32:29.38	37.932	-77.982	3.5	-0.26
2011/08/30	08:40:31.91	37.932	-77.953	-0.1	-0.35
2011/08/30	08:50:15.62	37.903	-77.973	8.0	1.32
2011/08/30	08:52:24.82	37.948	-77.985	2.3	-0.26
2011/08/30	09:06:04.31	37.922	-77.991	3.2	-0.38
2011/08/30	09:07:04.14	37.945	-77.947	6.3	0.92
2011/08/30	09:13:42.38	37.932	-77.981	4.3	0.74
2011/08/30	09:23:40.08	37.940	-77.909	-0.2	-1.07
2011/08/30	09:25:27.12	37.939	-77.985	4.0	0.38
2011/08/30	09:28:21.88	37.912	-77.993	5.2	-0.07
2011/08/30	09:30:39.38	37.950	-77.968	5.5	0.14
2011/08/30	09:38:09.49	37.921	-77.989	5.3	-0.36
2011/08/30	09:38:10.61	37.918	-77.995	1.6	-0.76
2011/08/30	09:44:12.03	37.935	-77.985	4.1	1.70
2011/08/30	09:51:49.22	37.956	-77.953	5.6	-0.35
2011/08/30	10:22:53.53	37.943	-77.960	5.6	1.53
2011/08/30	10:34:21.89	37.926	-77.989	3.9	-0.41
2011/08/30	10:48:08.09	37.970	-77.952	0.5	-0.39
2011/08/30	10:48:57.61	37.911	-77.986	7.9	-0.44
2011/08/30	10:59:12.72	37.917	-77.921	0.4	1.00
2011/08/30	11:00:36.07	37.930	-77.970	5.6	-0.57
2011/08/30	11:04:15.09	37.947	-77.969	5.2	0.14
2011/08/30	11:12:49.12	37.952	-77.945	6.8	0.09
2011/08/30	11:12:58.18	37.915	-77.918	-0.1	-0.78
2011/08/30	11:16:54.57	37.915	-77.918	0.2	-0.14
2011/08/30	11:17:00.80	37.933	-77.981	3.2	-0.65
2011/08/30	11:21:23.62	37.928	-77.987	5.9	-0.28
2011/08/30	11:54:51.71	37.929	-77.987	4.2	0.03

* z_0 = −0.4 km

The AIDA Backprojection Earthquake Catalog

Date (YYYY/MM/DD)	**Time (HH:MM:SS)**	**Latitude (°N)**	**Longitude (°E)**	**Depth (km)**	**Magnitude (M_{BPI})**
2011/08/30	12:14:30.96	37.924	-78.001	0.0	-0.30
2011/08/30	12:15:52.91	37.913	-77.994	4.2	0.87
2011/08/30	12:17:05.95	37.937	-77.985	3.9	1.20
2011/08/30	12:18:14.06	37.938	-78.013	-0.1	-0.73
2011/08/30	12:30:21.59	37.934	-77.958	5.6	-0.72
2011/08/30	12:34:26.65	37.944	-77.909	-0.2	-0.30
2011/08/30	12:38:00.85	37.939	-77.980	2.9	-0.71
2011/08/30	12:40:50.58	37.938	-77.987	4.4	0.29
2011/08/30	12:40:59.73	37.939	-77.987	4.4	0.08
2011/08/30	13:12:06.72	37.973	-77.928	6.6	-0.48
2011/08/30	13:25:02.77	37.943	-77.970	4.1	-0.62
2011/08/30	13:26:50.87	37.921	-77.982	5.6	2.22
2011/08/30	13:37:44.11	37.946	-77.972	4.7	-0.38
2011/08/30	13:56:28.35	37.909	-77.912	0.1	-0.71
2011/08/30	14:02:40.31	37.950	-77.941	7.4	0.76
2011/08/30	14:19:38.68	37.923	-77.989	3.8	-0.59
2011/08/30	14:22:40.72	37.933	-77.985	4.0	0.22
2011/08/30	14:32:00.65	37.904	-77.973	5.7	-0.57
2011/08/30	14:32:02.07	37.903	-77.962	0.6	-0.85
2011/08/30	14:51:45.38	37.915	-77.919	0.2	-0.14
2011/08/30	15:05:50.33	37.916	-77.918	0.7	-0.79
2011/08/30	15:15:08.80	37.946	-77.908	-0.2	-0.78
2011/08/30	15:24:48.48	37.898	-77.999	0.7	-0.60
2011/08/30	15:25:02.24	37.921	-77.991	2.8	-0.39
2011/08/30	15:33:19.21	37.954	-77.956	5.6	-0.07
2011/08/30	15:33:24.83	37.950	-77.978	2.1	-0.61
2011/08/30	15:37:17.17	37.942	-77.990	3.5	-0.01
2011/08/30	15:58:06.63	37.955	-77.974	7.6	-0.41
2011/08/30	16:42:47.39	37.935	-77.985	3.9	0.31
2011/08/30	17:38:16.61	37.903	-77.972	0.5	-0.70
2011/08/30	17:43:55.30	37.927	-77.987	4.0	-0.55
2011/08/30	17:59:45.05	37.908	-77.986	5.4	-0.63
2011/08/30	18:12:44.63	37.941	-77.981	3.7	0.13
2011/08/30	18:16:27.89	37.907	-77.992	5.9	1.13
2011/08/30	18:18:01.98	37.931	-77.984	4.0	1.75
2011/08/30	19:05:11.49	37.932	-77.986	4.2	-0.76
2011/08/30	19:10:27.32	37.933	-77.983	4.0	0.53
2011/08/30	19:20:36.54	37.947	-77.991	2.3	0.33
2011/08/30	19:24:45.28	37.928	-77.987	4.5	0.17
2011/08/30	19:27:53.70	37.916	-77.918	0.1	-0.83

* z_0 = −0.4 km

The AIDA Backprojection Earthquake Catalog

Date (YYYY/MM/DD)	**Time (HH:MM:SS)**	**Latitude (°N)**	**Longitude (°E)**	**Depth (km)**	**Magnitude (M_{BPI})**
2011/08/30	19:32:06.89	37.933	-77.983	4.2	0.17
2011/08/30	19:46:09.26	37.941	-77.984	4.9	1.44
2011/08/30	19:47:30.92	37.908	-78.007	3.5	0.44
2011/08/30	19:52:03.00	37.929	-77.987	4.1	-0.17
2011/08/30	19:53:08.39	37.946	-77.969	5.4	0.34
2011/08/30	19:56:56.76	37.939	-77.987	4.2	-0.65
2011/08/30	20:01:03.08	37.936	-77.958	5.6	0.10
2011/08/30	20:14:11.02	37.940	-77.978	3.7	0.06
2011/08/30	20:46:43.10	37.927	-77.987	4.0	-0.18
2011/08/30	20:48:28.96	37.971	-77.936	5.5	0.60
2011/08/30	20:54:15.81	37.972	-77.935	5.4	-0.61
2011/08/30	21:03:01.53	37.937	-77.984	4.2	0.17
2011/08/30	21:40:53.06	37.941	-77.951	6.3	0.30
2011/08/30	21:48:54.94	37.909	-78.000	-0.1	-0.54
2011/08/30	21:51:04.61	37.916	-77.920	0.4	0.03
2011/08/30	21:59:18.02	37.912	-77.977	5.8	0.18
2011/08/30	22:04:05.74	37.933	-77.998	6.0	-0.50
2011/08/30	22:06:48.68	37.931	-77.999	5.5	-0.59
2011/08/30	22:08:55.10	37.947	-77.990	2.4	-0.31
2011/08/30	22:09:41.29	37.935	-77.985	4.1	1.01
2011/08/30	22:25:14.61	37.925	-77.984	4.1	1.28
2011/08/30	22:29:26.44	37.950	-77.961	5.8	0.21
2011/08/30	22:35:47.86	37.914	-77.917	0.1	-0.20
2011/08/30	22:37:56.99	37.909	-78.001	3.1	-0.74
2011/08/30	22:41:25.41	37.938	-77.978	4.2	-0.08
2011/08/30	22:47:10.75	37.944	-77.969	4.3	-0.44
2011/08/30	22:52:14.13	37.930	-77.934	0.0	-0.78
2011/08/30	23:11:45.55	37.924	-77.989	3.8	-0.64
2011/08/30	23:28:43.44	37.914	-77.918	0.1	-0.68
2011/08/30	23:33:02.53	37.939	-77.986	4.3	-0.40
2011/08/30	23:41:16.18	37.935	-77.993	3.5	-0.70
2011/08/30	23:50:16.87	37.939	-77.910	4.2	-0.88
2011/08/30	23:56:46.75	37.935	-77.983	3.7	-0.66
2011/08/30	23:58:44.15	37.909	-78.006	3.6	0.08
2011/08/31	00:00:01.51	37.948	-77.942	6.6	-0.61
2011/08/31	00:00:03.14	37.942	-77.941	0.0	-0.70
2011/08/31	00:04:00.92	37.963	-77.997	5.6	-0.51
2011/08/31	00:29:57.47	37.926	-77.984	4.4	-1.32
2011/08/31	00:34:59.88	37.934	-77.985	4.3	-1.18
2011/08/31	00:41:57.43	37.965	-77.997	0.2	-0.68

* z_0 = −0.4 km

The AIDA Backprojection Earthquake Catalog

Date (YYYY/MM/DD)	**Time (HH:MM:SS)**	**Latitude (°N)**	**Longitude (°E)**	**Depth (km)**	**Magnitude (M_{BPI})**
2011/08/31	00:53:03.35	37.923	-77.992	3.4	-0.72
2011/08/31	00:59:18.93	37.965	-77.952	4.9	-0.37
2011/08/31	00:59:27.82	37.946	-77.959	6.4	1.53
2011/08/31	01:03:27.08	37.947	-77.975	3.2	-0.22
2011/08/31	01:23:19.43	37.923	-77.995	3.5	-0.16
2011/08/31	01:35:50.86	37.952	-77.972	3.9	-0.50
2011/08/31	01:45:13.24	37.887	-77.983	5.5	-0.78
2011/08/31	01:45:14.39	37.884	-77.984	2.1	-0.84
2011/08/31	02:17:21.26	37.947	-77.972	4.6	-0.51
2011/08/31	02:26:05.16	37.936	-77.958	5.6	0.34
2011/08/31	02:35:06.69	37.944	-77.966	4.8	-0.86
2011/08/31	02:36:36.89	37.890	-78.008	-0.2	-0.70
2011/08/31	02:42:13.95	37.969	-77.929	6.0	-0.10
2011/08/31	02:58:32.94	37.935	-77.976	4.3	-0.95
2011/08/31	03:09:56.72	37.935	-77.910	0.1	-0.55
2011/08/31	03:14:02.46	37.925	-77.910	-0.2	-0.45
2011/08/31	03:20:32.02	37.946	-77.970	3.7	-0.73
2011/08/31	03:22:48.60	37.945	-77.908	0.1	-0.86
2011/08/31	03:23:59.86	37.936	-77.986	4.2	-0.39
2011/08/31	03:26:06.27	37.922	-77.985	4.7	-0.75
2011/08/31	03:30:37.67	37.952	-77.908	-0.2	-0.97
2011/08/31	03:32:57.46	37.939	-77.983	3.7	1.08
2011/08/31	03:39:36.52	37.965	-77.935	7.3	0.53
2011/08/31	03:40:31.70	37.943	-77.968	5.0	-0.87
2011/08/31	03:46:15.79	37.890	-77.920	0.0	-0.87
2011/08/31	03:55:00.36	37.936	-77.984	3.9	-0.38
2011/08/31	03:56:50.90	37.939	-77.986	4.0	-0.31
2011/08/31	04:01:37.53	37.922	-77.983	4.3	-0.68
2011/08/31	04:09:30.34	37.966	-77.981	7.6	-0.98
2011/08/31	04:20:37.70	37.915	-77.997	3.5	-0.45
2011/08/31	04:20:39.23	37.904	-77.936	2.1	-0.98
2011/08/31	04:21:44.95	37.917	-77.994	3.4	-0.75
2011/08/31	04:41:28.46	37.917	-77.992	3.6	-0.75
2011/08/31	04:44:50.66	37.939	-77.983	4.4	-0.69
2011/08/31	04:48:18.16	37.929	-77.985	3.8	0.36
2011/08/31	04:49:55.95	37.942	-77.990	5.1	-0.93
2011/08/31	04:53:49.23	37.928	-77.985	4.8	1.68
2011/08/31	05:04:43.51	37.922	-77.921	0.0	-0.73
2011/08/31	05:05:15.28	37.926	-77.986	3.5	-0.21
2011/08/31	05:10:09.18	37.949	-77.969	5.5	-0.16

* z_0 = −0.4 km

The AIDA Backprojection Earthquake Catalog

Date (YYYY/MM/DD)	**Time (HH:MM:SS)**	**Latitude (°N)**	**Longitude (°E)**	**Depth (km)**	**Magnitude (M_{BPI})**
2011/08/31	05:35:14.41	37.889	-77.984	6.0	-1.05
2011/08/31	05:41:02.80	37.918	-77.994	4.0	0.47
2011/08/31	05:57:22.09	37.926	-77.984	4.5	0.48
2011/08/31	05:59:21.34	37.938	-77.977	2.6	-1.10
2011/08/31	06:04:30.68	37.933	-77.966	5.2	-0.79
2011/08/31	06:05:57.81	37.948	-77.967	4.9	-0.50
2011/08/31	06:06:52.11	37.920	-77.995	3.9	-0.32
2011/08/31	06:09:16.89	37.923	-77.981	4.8	-0.98
2011/08/31	06:42:07.70	37.874	-77.935	-0.1	-1.13
2011/08/31	06:50:41.68	37.886	-77.985	5.5	0.09
2011/08/31	06:53:56.95	37.939	-77.991	1.7	-0.80
2011/08/31	07:00:18.80	37.930	-77.982	4.2	-0.15
2011/08/31	07:05:30.70	37.930	-77.982	4.4	-0.14
2011/08/31	07:07:26.26	37.909	-77.991	5.3	-0.05
2011/08/31	07:07:31.54	37.912	-77.989	5.9	-0.75
2011/08/31	07:20:00.90	37.949	-77.978	2.5	-0.47
2011/08/31	07:29:19.67	37.930	-77.966	6.2	-0.90
2011/08/31	07:35:28.42	37.933	-77.986	3.8	-0.26
2011/08/31	07:54:01.50	37.921	-77.987	3.3	-0.73
2011/08/31	07:55:13.01	37.926	-77.980	4.4	-0.40
2011/08/31	08:03:21.57	37.899	-77.975	6.4	0.52
2011/08/31	08:05:20.31	37.918	-77.918	0.0	-1.02
2011/08/31	08:05:25.28	37.938	-77.987	4.0	-0.68
2011/08/31	08:11:13.54	37.947	-77.970	4.5	-0.80
2011/08/31	08:25:38.82	37.914	-77.993	4.1	-0.92
2011/08/31	08:33:15.65	37.939	-77.982	4.0	0.83
2011/08/31	08:35:06.24	37.931	-77.966	4.8	-1.04
2011/08/31	08:45:11.50	37.939	-77.985	4.2	-0.92
2011/08/31	08:45:47.66	37.949	-77.958	5.9	-1.00
2011/08/31	08:51:52.29	37.930	-77.983	3.7	-0.73
2011/08/31	09:01:28.03	37.947	-77.967	4.9	0.39
2011/08/31	09:11:14.51	37.915	-77.997	4.3	0.14
2011/08/31	09:23:07.22	37.878	-77.922	0.5	-0.04
2011/08/31	09:33:44.50	37.945	-77.983	2.2	-0.54
2011/08/31	09:38:09.60	37.949	-77.960	5.3	-0.46
2011/08/31	09:46:02.79	37.916	-77.995	4.0	-1.02
2011/08/31	09:50:41.11	37.916	-77.918	-0.2	-1.17
2011/08/31	09:54:06.38	37.948	-77.975	4.6	0.45
2011/08/31	10:11:15.15	37.917	-77.992	3.2	-0.48
2011/08/31	10:35:42.52	37.939	-77.981	3.3	0.40

* z_0 = −0.4 km

The AIDA Backprojection Earthquake Catalog

Date (YYYY/MM/DD)	**Time (HH:MM:SS)**	**Latitude (°N)**	**Longitude (°E)**	**Depth (km)**	**Magnitude (M_{BPI})**
2011/08/31	10:43:09.68	37.930	-77.990	5.0	-0.74
2011/08/31	10:43:49.14	37.936	-77.983	3.6	-0.72
2011/08/31	11:10:41.56	37.915	-77.919	0.1	-0.22
2011/08/31	11:31:22.26	37.943	-77.987	1.8	-0.61
2011/08/31	11:37:43.10	37.944	-77.948	6.4	-0.46
2011/08/31	11:39:50.46	37.946	-77.952	0.0	-0.85
2011/08/31	11:54:07.40	37.941	-77.983	4.4	0.11
2011/08/31	12:33:35.15	37.939	-77.987	3.7	1.47
2011/08/31	12:49:41.03	37.933	-77.972	5.1	-0.72
2011/08/31	12:55:16.11	37.955	-77.961	4.9	-0.25
2011/08/31	12:55:57.36	37.915	-77.920	0.4	0.08
2011/08/31	13:12:22.47	37.953	-77.939	7.0	-0.23
2011/08/31	13:31:04.83	37.958	-77.994	0.7	-0.49
2011/08/31	13:34:10.08	37.939	-77.954	6.1	0.15
2011/08/31	13:55:01.96	37.937	-77.984	4.0	0.25
2011/08/31	14:02:57.58	37.866	-77.925	1.5	-0.50
2011/08/31	14:10:10.74	37.919	-77.984	5.2	-0.28
2011/08/31	14:27:07.03	37.976	-77.931	7.2	-0.12
2011/08/31	14:30:22.72	37.934	-77.984	4.1	-0.11
2011/08/31	14:40:44.57	37.939	-77.977	4.4	-0.74
2011/08/31	14:41:05.02	37.940	-77.977	4.6	-0.74
2011/08/31	14:41:41.57	37.948	-77.984	5.9	-0.49
2011/08/31	14:49:07.58	37.930	-77.981	3.7	-0.58
2011/08/31	14:52:59.81	37.940	-77.973	5.1	-0.37
2011/08/31	15:01:54.91	37.948	-77.974	3.6	1.71
2011/08/31	15:03:37.69	37.963	-78.015	0.1	-0.22
2011/08/31	15:05:04.93	37.914	-77.918	-0.1	-0.70
2011/08/31	15:09:17.36	37.884	-77.909	0.3	-0.87
2011/08/31	15:11:06.44	37.904	-77.925	3.5	0.69
2011/08/31	15:11:34.89	37.918	-77.921	0.4	0.43
2011/08/31	15:50:33.59	37.942	-77.951	0.1	1.19
2011/08/31	15:52:54.45	37.969	-78.026	-0.2	-0.39
2011/08/31	16:22:13.52	37.903	-77.999	5.3	-0.11
2011/08/31	16:31:45.84	37.946	-77.972	4.3	-0.59
2011/08/31	16:39:02.17	37.950	-77.964	5.4	1.73
2011/08/31	17:06:49.58	37.915	-77.919	0.1	-0.63
2011/08/31	17:15:09.60	37.921	-77.907	0.5	-0.77
2011/08/31	17:20:14.04	37.933	-78.011	0.9	-0.40
2011/08/31	17:24:10.88	37.944	-77.986	2.3	1.74
2011/08/31	17:42:56.63	37.930	-77.975	4.9	-0.34

* z_0 = −0.4 km

The AIDA Backprojection Earthquake Catalog

Date (YYYY/MM/DD)	**Time (HH:MM:SS)**	**Latitude (°N)**	**Longitude (°E)**	**Depth (km)**	**Magnitude (M_{BPI})**
2011/08/31	17:49:07.17	37.931	-77.983	3.4	-0.33
2011/08/31	18:00:07.98	37.915	-77.919	-0.1	-1.75
2011/08/31	18:01:22.96	37.924	-77.975	5.6	-1.07
2011/08/31	18:06:28.52	37.895	-77.962	1.8	-1.05
2011/08/31	18:17:16.80	37.910	-77.978	5.2	0.34
2011/08/31	18:42:34.30	37.948	-77.940	6.9	0.46
2011/08/31	18:51:31.06	37.943	-77.989	2.5	-0.59
2011/08/31	19:00:42.73	37.936	-77.966	4.8	-1.73
2011/08/31	19:12:35.78	37.948	-77.968	5.1	1.63
2011/08/31	19:13:23.31	37.948	-77.967	5.2	0.19
2011/08/31	19:18:43.33	37.948	-77.968	5.4	1.75
2011/08/31	19:20:14.92	37.945	-77.909	-0.2	-0.28
2011/08/31	19:25:02.85	37.939	-77.947	5.4	-0.29
2011/08/31	19:35:27.47	37.914	-77.997	4.7	0.27
2011/08/31	19:53:33.93	37.921	-77.985	3.8	-0.06
2011/08/31	20:06:05.74	37.920	-77.925	0.1	-1.12
2011/08/31	20:21:03.91	37.918	-77.990	5.5	0.19
2011/08/31	20:22:19.57	37.929	-77.975	4.4	-0.30
2011/08/31	20:54:02.13	37.940	-77.954	4.4	-0.20
2011/08/31	21:08:39.73	37.906	-77.993	4.1	-1.08
2011/08/31	21:14:25.77	37.916	-77.919	0.3	-0.28
2011/08/31	21:19:43.64	37.932	-77.977	4.2	-0.48
2011/08/31	21:26:07.10	37.950	-77.960	4.3	0.17
2011/08/31	21:37:57.91	37.918	-77.919	0.0	-0.75
2011/08/31	21:52:04.55	37.913	-77.918	-0.1	0.01
2011/08/31	21:57:41.55	37.939	-77.967	5.7	0.22
2011/08/31	22:13:49.25	37.913	-77.974	6.9	-0.67
2011/08/31	22:20:54.94	37.942	-77.910	-0.2	-0.65
2011/08/31	22:23:35.89	37.901	-77.984	5.7	-0.45
2011/08/31	22:40:02.69	37.935	-77.984	4.2	1.67
2011/08/31	22:40:26.99	37.918	-77.994	3.9	-0.30
2011/08/31	22:43:44.65	37.973	-77.942	6.4	-0.16
2011/08/31	23:07:06.66	37.945	-77.956	4.3	0.13
2011/08/31	23:13:16.97	37.887	-77.984	5.4	-0.44
2011/08/31	23:22:30.89	37.921	-77.997	4.9	-0.68
2011/08/31	23:33:15.83	37.914	-77.918	0.4	-0.66
2011/08/31	23:37:35.78	37.924	-77.985	4.8	-0.11
2011/08/31	23:53:08.62	37.914	-77.919	0.2	-0.60
2011/08/31	23:57:47.86	37.878	-77.970	5.2	-0.51
2011/09/01	00:14:32.33	37.963	-77.967	2.8	-0.59

* z_0 = −0.4 km

The AIDA Backprojection Earthquake Catalog

Date (YYYY/MM/DD)	**Time (HH:MM:SS)**	**Latitude (°N)**	**Longitude (°E)**	**Depth (km)**	**Magnitude (M_{BPI})**
2011/09/01	00:15:45.37	37.920	-77.990	3.9	-0.82
2011/09/01	00:32:54.53	37.917	-77.995	4.9	-0.77
2011/09/01	00:32:55.64	37.912	-77.997	1.2	-0.78
2011/09/01	00:44:34.56	37.931	-77.982	3.9	-0.28
2011/09/01	00:46:31.96	37.936	-77.983	4.0	-0.41
2011/09/01	01:07:00.98	37.942	-77.909	-0.1	-1.01
2011/09/01	01:23:23.00	37.937	-77.982	3.8	-0.93
2011/09/01	01:27:49.28	37.968	-77.933	5.9	0.98
2011/09/01	01:33:07.43	37.906	-77.987	5.6	-0.38
2011/09/01	01:44:42.07	37.943	-77.980	1.5	-0.87
2011/09/01	01:48:53.48	37.904	-77.923	3.4	-1.01
2011/09/01	01:50:27.18	37.915	-77.993	3.7	0.32
2011/09/01	01:53:32.90	37.934	-77.983	3.9	-0.10
2011/09/01	02:07:17.90	37.939	-77.968	4.7	-0.06
2011/09/01	02:09:50.30	37.933	-77.991	3.3	-0.71
2011/09/01	02:15:08.48	37.938	-77.974	5.0	-0.75
2011/09/01	02:41:47.35	37.888	-78.003	-0.1	-0.70
2011/09/01	02:43:40.44	37.942	-77.964	5.8	-0.67
2011/09/01	02:48:12.98	37.935	-77.986	4.4	-0.65
2011/09/01	02:50:22.46	37.937	-77.972	5.2	0.27
2011/09/01	02:55:21.12	37.958	-77.966	2.4	0.42
2011/09/01	03:10:27.99	37.923	-77.978	5.6	-0.88
2011/09/01	03:25:19.34	37.926	-77.981	5.4	-0.47
2011/09/01	03:26:35.75	37.902	-77.935	0.2	-0.30
2011/09/01	03:45:41.18	37.936	-77.987	4.4	-0.31
2011/09/01	04:24:12.74	37.956	-77.984	1.1	-0.57
2011/09/01	04:26:04.91	37.888	-77.982	5.4	-0.40
2011/09/01	04:29:30.15	37.939	-77.985	4.2	-0.42
2011/09/01	04:41:21.66	37.907	-77.987	5.3	1.21
2011/09/01	04:43:50.50	37.939	-77.983	3.3	0.58
2011/09/01	04:57:44.71	37.921	-77.986	3.0	-0.66
2011/09/01	05:18:01.31	37.948	-77.967	5.3	-0.80
2011/09/01	05:23:14.87	37.918	-77.999	3.1	0.79
2011/09/01	05:28:29.94	37.915	-77.992	3.7	-0.00
2011/09/01	05:35:42.89	37.943	-77.977	5.2	0.27
2011/09/01	05:37:49.06	37.948	-77.967	4.9	-0.07
2011/09/01	05:39:26.12	37.939	-77.983	2.9	-0.85
2011/09/01	05:48:43.21	37.933	-77.981	4.2	-0.44
2011/09/01	05:49:20.47	37.897	-77.972	7.6	0.11
2011/09/01	05:57:22.25	37.903	-77.970	7.8	-0.38

* z_0 = −0.4 km

The AIDA Backprojection Earthquake Catalog

Date (YYYY/MM/DD)	**Time (HH:MM:SS)**	**Latitude (°N)**	**Longitude (°E)**	**Depth (km)**	**Magnitude (M_{BPI})**
2011/09/01	06:12:18.73	37.904	-77.923	3.3	0.05
2011/09/01	06:30:03.63	37.972	-77.972	0.6	-0.89
2011/09/01	06:44:01.35	37.920	-77.993	3.3	0.24
2011/09/01	06:44:37.97	37.925	-77.986	3.9	-0.65
2011/09/01	06:47:00.32	37.952	-77.959	4.9	-0.53
2011/09/01	06:50:07.03	37.939	-77.992	4.8	-0.95
2011/09/01	06:50:32.69	37.924	-77.981	4.5	-0.46
2011/09/01	06:54:55.95	37.921	-77.991	3.5	0.28
2011/09/01	06:57:13.14	37.921	-77.992	2.9	-0.53
2011/09/01	06:58:08.51	37.938	-77.985	3.7	-0.08
2011/09/01	06:59:34.98	37.915	-77.916	0.5	-1.05
2011/09/01	07:05:23.74	37.921	-77.921	3.8	-1.10
2011/09/01	07:11:22.17	37.924	-77.985	4.9	0.38
2011/09/01	07:11:55.22	37.909	-78.006	4.1	-0.46
2011/09/01	07:14:53.08	37.897	-77.972	7.6	-0.79
2011/09/01	07:14:54.86	37.900	-77.962	2.2	-0.95
2011/09/01	07:14:58.97	37.948	-77.960	5.3	-1.31
2011/09/01	07:18:54.89	37.943	-77.966	5.0	-0.77
2011/09/01	07:36:24.05	37.924	-78.013	1.1	-0.70
2011/09/01	07:53:04.79	37.939	-77.964	5.5	-1.07
2011/09/01	07:58:06.43	37.918	-77.917	0.5	-1.27
2011/09/01	07:59:39.60	37.920	-77.999	4.0	-0.73
2011/09/01	08:11:36.40	37.938	-77.987	1.3	-0.84
2011/09/01	08:25:30.49	37.967	-77.935	5.5	0.41
2011/09/01	08:27:29.17	37.946	-77.994	2.9	-0.92
2011/09/01	08:47:14.52	37.915	-77.997	4.1	-0.50
2011/09/01	08:48:54.90	37.866	-77.917	-0.2	-1.05
2011/09/01	08:55:58.48	37.929	-77.970	5.7	-0.35
2011/09/01	09:00:41.98	37.923	-77.910	0.8	-0.73
2011/09/01	09:09:37.65	37.948	-77.948	7.4	3.81
2011/09/01	09:14:51.28	37.946	-77.947	6.7	-0.22
2011/09/01	09:15:55.18	37.936	-77.973	5.4	-0.83
2011/09/01	09:16:25.44	37.942	-77.950	6.0	-0.57
2011/09/01	09:18:14.32	37.934	-77.984	4.5	-0.53
2011/09/01	09:33:48.86	37.932	-77.986	4.3	0.40
2011/09/01	09:36:55.92	37.933	-77.973	5.8	0.10
2011/09/01	09:46:17.92	37.943	-77.966	5.1	1.12
2011/09/01	09:55:51.39	37.943	-77.989	2.5	-0.14
2011/09/01	09:56:13.22	37.945	-77.950	6.2	-0.55
2011/09/01	09:56:14.70	37.943	-77.951	0.2	-0.60

* z_0 = −0.4 km

The AIDA Backprojection Earthquake Catalog

Date (YYYY/MM/DD)	**Time (HH:MM:SS)**	**Latitude (°N)**	**Longitude (°E)**	**Depth (km)**	**Magnitude (M_{BPI})**
2011/09/01	10:01:33.20	37.959	-77.942	6.7	-0.17
2011/09/01	10:02:53.77	37.973	-77.934	5.9	0.92
2011/09/01	10:03:13.32	37.933	-77.984	3.6	-0.34
2011/09/01	10:19:36.52	37.902	-77.920	-0.2	-1.07
2011/09/01	10:21:05.17	37.943	-77.949	6.4	-0.28
2011/09/01	10:26:38.36	37.938	-77.985	3.7	-0.18
2011/09/01	10:27:09.27	37.940	-77.980	4.1	-0.76
2011/09/01	10:35:12.07	37.911	-78.005	5.0	1.31
2011/09/01	10:35:42.93	37.909	-77.994	3.9	0.01
2011/09/01	10:38:02.74	37.919	-77.918	0.4	-0.56
2011/09/01	10:39:39.28	37.936	-77.982	3.4	-0.10
2011/09/01	11:18:59.56	37.916	-77.919	-0.1	-0.58
2011/09/01	11:41:00.35	37.919	-77.918	0.6	-0.76
2011/09/01	12:02:06.72	37.948	-77.961	4.9	0.49
2011/09/01	12:11:49.21	37.915	-77.994	3.8	0.01
2011/09/01	12:17:11.72	37.949	-77.970	5.4	-0.40
2011/09/01	12:22:06.91	37.942	-77.985	2.1	-0.57
2011/09/01	12:34:48.20	37.939	-77.976	3.1	-0.66
2011/09/01	12:35:32.30	37.945	-77.949	6.2	1.56
2011/09/01	12:56:34.52	37.935	-77.987	4.1	-0.22
2011/09/01	12:58:55.21	37.948	-77.950	8.0	-0.38
2011/09/01	13:00:26.58	37.904	-77.997	5.5	-0.24
2011/09/01	13:22:29.53	37.934	-77.984	3.7	-0.36
2011/09/01	13:35:22.22	37.899	-77.972	6.8	0.69
2011/09/01	13:48:48.87	37.941	-77.936	2.6	-0.79
2011/09/01	14:07:15.55	37.975	-77.940	7.7	-0.22
2011/09/01	14:18:47.16	37.919	-78.016	0.4	-0.16
2011/09/01	14:19:37.57	37.919	-77.917	0.5	-0.46
2011/09/01	14:27:32.74	37.913	-78.002	5.0	-0.01
2011/09/01	14:31:47.03	37.905	-77.986	6.4	0.86
2011/09/01	14:40:49.65	37.940	-77.950	5.9	0.44
2011/09/01	15:07:04.52	37.949	-77.960	4.6	0.00
2011/09/01	15:14:08.02	37.947	-77.966	4.9	-0.45
2011/09/01	15:20:26.24	37.932	-77.981	4.0	-0.15
2011/09/01	15:25:40.91	37.950	-78.011	3.3	-0.57
2011/09/01	15:25:56.61	37.939	-77.987	4.1	0.84
2011/09/01	15:31:58.89	37.908	-77.937	2.1	-0.42
2011/09/01	15:34:05.93	37.926	-77.985	4.0	-0.31
2011/09/01	15:49:02.13	37.939	-77.989	4.1	0.54
2011/09/01	15:55:10.76	37.942	-77.948	6.0	0.41

* z_0 = −0.4 km

The AIDA Backprojection Earthquake Catalog

Date (YYYY/MM/DD)	**Time (HH:MM:SS)**	**Latitude (°N)**	**Longitude (°E)**	**Depth (km)**	**Magnitude (M_{BPI})**
2011/09/01	16:05:42.60	37.937	-77.983	5.5	-0.05
2011/09/01	16:25:55.54	37.944	-77.969	3.4	-0.30
2011/09/01	16:47:07.65	37.932	-77.982	4.4	0.86
2011/09/01	17:10:16.72	37.909	-78.008	3.8	-0.11
2011/09/01	17:37:54.59	37.891	-77.937	2.9	-0.52
2011/09/01	17:40:34.37	37.939	-77.987	4.2	-0.63
2011/09/01	18:21:34.95	37.948	-77.980	2.3	1.15
2011/09/01	18:29:05.09	37.948	-77.908	-0.1	0.18
2011/09/01	18:29:07.22	37.906	-77.927	-0.2	-0.16
2011/09/01	18:29:40.68	37.930	-77.911	1.8	-0.82
2011/09/01	18:40:16.64	37.915	-77.918	-0.1	-0.51
2011/09/01	18:50:30.37	37.929	-77.987	3.4	-0.59
2011/09/01	18:58:20.22	37.940	-77.967	6.6	0.28
2011/09/01	19:01:55.08	37.937	-77.982	3.8	-0.45
2011/09/01	19:04:12.14	37.935	-77.981	3.5	0.06
2011/09/01	19:04:53.26	37.930	-78.007	0.8	-0.07
2011/09/01	19:41:52.10	37.946	-77.908	0.1	-0.72
2011/09/01	19:44:23.45	37.915	-77.922	0.4	0.09
2011/09/01	19:48:58.10	37.923	-77.918	4.8	-0.25
2011/09/01	20:15:01.03	37.939	-77.987	4.0	-0.19
2011/09/01	20:48:59.88	37.949	-77.961	5.1	0.20
2011/09/01	20:54:06.65	37.950	-77.970	4.7	0.36
2011/09/01	21:12:58.97	37.890	-77.972	0.5	-1.08
2011/09/01	21:24:27.03	37.951	-77.960	4.9	-0.54
2011/09/01	21:25:14.19	37.907	-77.997	5.1	-0.18
2011/09/01	21:52:35.59	37.890	-77.940	0.0	-1.28
2011/09/01	22:00:45.32	37.931	-77.999	6.2	-0.83
2011/09/01	22:11:31.75	37.897	-77.978	7.7	0.19
2011/09/01	22:23:56.14	37.920	-77.920	0.6	-0.53
2011/09/01	22:27:16.22	37.952	-77.950	5.4	-0.23
2011/09/01	22:50:36.03	37.948	-77.966	4.9	-0.10
2011/09/01	22:55:46.21	37.914	-77.990	4.2	-0.70
2011/09/01	22:58:25.42	37.939	-77.980	2.9	-0.81
2011/09/01	23:08:02.61	37.945	-77.966	5.4	0.24
2011/09/01	23:19:47.18	37.945	-77.957	0.8	-1.25
2011/09/01	23:25:38.03	37.942	-77.974	5.0	-0.28
2011/09/01	23:26:38.45	37.914	-77.985	5.4	-0.76
2011/09/01	23:31:33.68	37.918	-77.998	3.2	0.94
2011/09/01	23:35:07.62	37.908	-77.993	5.1	-0.59
2011/09/01	23:50:16.99	37.941	-77.985	3.0	0.41

* z_0 = −0.4 km

The AIDA Backprojection Earthquake Catalog

Date (YYYY/MM/DD)	**Time (HH:MM:SS)**	**Latitude (°N)**	**Longitude (°E)**	**Depth (km)**	**Magnitude (M_{BPI})**
2011/09/02	00:02:45.35	37.938	-77.978	6.0	-0.69
2011/09/02	00:17:35.98	37.904	-77.997	0.7	-0.49
2011/09/02	01:14:16.07	37.939	-77.975	3.6	0.65
2011/09/02	01:16:43.45	37.916	-77.919	0.4	-0.05
2011/09/02	01:18:57.54	37.924	-77.958	6.7	1.36
2011/09/02	01:26:43.70	37.915	-77.918	0.4	-0.83
2011/09/02	01:26:58.91	37.959	-77.957	3.8	0.19
2011/09/02	01:52:05.77	37.940	-77.980	3.9	-0.18
2011/09/02	01:53:53.21	37.916	-77.919	0.4	-0.61
2011/09/02	02:23:44.09	37.944	-77.949	6.0	-0.66
2011/09/02	02:23:45.49	37.945	-77.950	1.5	-0.66
2011/09/02	02:30:46.88	37.947	-77.968	5.0	0.42
2011/09/02	02:37:01.43	37.924	-77.991	3.8	-0.48
2011/09/02	02:57:17.53	37.940	-77.994	2.2	0.33
2011/09/02	03:00:46.47	37.978	-77.923	7.5	-0.72
2011/09/02	03:17:32.61	37.946	-77.954	5.5	-0.56
2011/09/02	03:22:18.92	37.945	-77.945	6.2	-0.82
2011/09/02	03:32:43.22	37.944	-77.964	4.9	-0.82
2011/09/02	04:09:08.64	37.956	-77.909	-0.2	-0.74
2011/09/02	04:30:03.84	37.923	-77.993	3.1	-0.51
2011/09/02	04:34:50.44	37.919	-77.990	4.3	1.25
2011/09/02	04:38:23.82	37.916	-77.929	0.2	-0.99
2011/09/02	04:53:13.92	37.941	-77.976	4.8	0.30
2011/09/02	04:56:48.32	37.952	-77.945	5.9	-0.71
2011/09/02	05:18:44.91	37.941	-77.965	5.2	-0.49
2011/09/02	05:44:22.04	37.938	-77.989	3.6	-0.81
2011/09/02	05:57:26.94	37.882	-77.907	-0.2	-1.07
2011/09/02	06:03:33.39	37.931	-77.984	4.1	-0.50
2011/09/02	06:07:23.27	37.933	-77.960	5.3	-0.80
2011/09/02	06:09:11.54	37.916	-77.917	0.3	0.35
2011/09/02	06:31:55.77	37.940	-77.981	4.6	-0.80
2011/09/02	06:32:54.39	37.939	-77.964	5.7	0.15
2011/09/02	06:38:18.63	37.915	-77.917	-0.1	-0.77
2011/09/02	06:39:04.93	37.933	-77.976	4.2	-0.85
2011/09/02	06:47:28.54	37.932	-77.982	4.4	0.46
2011/09/02	06:55:30.04	37.921	-77.989	3.9	0.15
2011/09/02	07:13:49.60	37.950	-77.981	2.7	-0.21
2011/09/02	07:16:46.98	37.946	-77.987	2.2	-0.06
2011/09/02	07:22:32.61	37.943	-77.961	5.2	-0.35
2011/09/02	07:31:31.67	37.955	-77.998	0.0	-0.65

* z_0 = −0.4 km

The AIDA Backprojection Earthquake Catalog

Date (YYYY/MM/DD)	**Time (HH:MM:SS)**	**Latitude (°N)**	**Longitude (°E)**	**Depth (km)**	**Magnitude (M_{BPI})**
2011/09/02	07:34:00.62	37.962	-77.990	0.6	0.42
2011/09/02	08:18:12.97	37.923	-77.991	3.3	-0.05
2011/09/02	08:19:59.82	37.927	-77.989	4.0	-1.44
2011/09/02	08:38:39.70	37.915	-77.919	0.1	-1.09
2011/09/02	08:45:51.50	37.948	-77.980	2.9	-0.33
2011/09/02	09:02:03.68	37.957	-77.946	6.0	-0.04
2011/09/02	09:08:28.92	37.949	-77.953	5.5	-0.76
2011/09/02	09:10:53.57	37.926	-77.986	3.6	0.77
2011/09/02	09:17:32.58	37.933	-77.968	5.2	0.62
2011/09/02	09:20:03.93	37.933	-77.983	4.1	-0.85
2011/09/02	09:20:04.84	37.931	-77.997	1.3	-1.00
2011/09/02	09:21:02.55	37.935	-77.983	4.6	-0.61
2011/09/02	09:56:16.03	37.960	-77.985	2.1	-0.61
2011/09/02	10:01:59.63	37.950	-77.950	5.4	-0.63
2011/09/02	10:07:22.74	37.948	-77.960	5.2	-0.37
2011/09/02	10:16:27.84	37.905	-77.998	1.3	-0.75
2011/09/02	10:20:48.77	37.933	-77.967	5.5	-0.26
2011/09/02	10:24:43.72	37.930	-77.972	5.5	-0.71
2011/09/02	10:24:58.29	37.933	-77.987	3.6	-1.06
2011/09/02	10:25:47.12	37.921	-77.984	4.7	0.33
2011/09/02	10:33:39.14	37.924	-77.986	4.2	-0.41
2011/09/02	10:33:40.19	37.927	-77.989	1.1	-0.55
2011/09/02	10:53:05.45	37.920	-77.919	0.4	-0.86
2011/09/02	11:06:07.64	37.909	-78.002	4.5	-0.30
2011/09/02	11:12:43.27	37.913	-77.998	3.9	0.75
2011/09/02	11:38:35.70	37.947	-77.967	4.6	-0.14
2011/09/02	12:22:21.34	37.931	-77.985	3.9	0.33
2011/09/02	12:37:56.25	37.939	-77.983	4.2	0.79
2011/09/02	12:58:08.52	37.911	-78.000	3.0	-0.59
2011/09/02	13:07:48.18	37.931	-77.965	5.3	-0.35
2011/09/02	13:07:49.49	37.930	-77.970	0.8	-0.58
2011/09/02	13:38:49.58	37.940	-77.992	1.8	-0.03
2011/09/02	13:52:45.74	37.939	-77.973	5.3	-0.38
2011/09/02	14:05:34.40	37.944	-77.985	2.3	-0.61
2011/09/02	14:16:54.45	37.940	-77.983	3.4	-0.06
2011/09/02	14:20:07.78	37.946	-77.972	5.0	-0.08
2011/09/02	14:27:00.08	37.912	-77.992	4.2	-0.08
2011/09/02	14:32:07.22	37.943	-77.947	5.8	0.11
2011/09/02	14:45:49.16	37.938	-77.982	4.1	-0.64
2011/09/02	15:21:52.20	37.900	-78.018	2.6	-0.76

* z_0 = −0.4 km

The AIDA Backprojection Earthquake Catalog

Date (YYYY/MM/DD)	**Time (HH:MM:SS)**	**Latitude (°N)**	**Longitude (°E)**	**Depth (km)**	**Magnitude (M_{BPI})**
2011/09/02	15:46:57.49	37.925	-77.986	3.8	-0.67
2011/09/02	15:50:25.51	37.922	-77.990	3.3	0.20
2011/09/02	16:00:56.25	37.895	-77.991	4.7	-0.40
2011/09/02	16:14:11.68	37.923	-77.910	0.8	-0.76
2011/09/02	16:22:24.33	37.968	-77.931	6.2	-0.44
2011/09/02	16:31:36.09	37.944	-77.970	4.9	-0.45
2011/09/02	16:52:57.56	37.919	-77.918	0.5	-0.94
2011/09/02	17:01:02.71	37.915	-77.993	3.8	0.39
2011/09/02	17:13:45.55	37.948	-77.967	5.2	0.62
2011/09/02	17:24:21.29	37.927	-77.981	3.6	-0.76
2011/09/02	17:27:22.12	37.949	-77.967	5.5	-0.70
2011/09/02	17:32:32.62	37.948	-77.967	5.1	-0.32
2011/09/02	17:41:42.94	37.933	-77.980	4.2	0.86
2011/09/02	17:58:00.09	37.869	-77.926	2.3	-1.40
2011/09/02	18:06:36.52	37.885	-77.907	5.5	-0.80
2011/09/02	18:20:39.86	37.875	-77.924	8.7	-0.35
2011/09/02	18:30:16.90	37.891	-77.929	8.4	0.01
2011/09/02	18:36:55.84	37.948	-77.956	5.2	0.06
2011/09/02	18:37:54.65	37.871	-77.944	7.1	-0.66
2011/09/02	18:40:25.57	37.880	-77.927	8.6	-0.87
2011/09/02	18:57:09.10	37.950	-77.962	5.8	-0.60
2011/09/02	19:07:50.53	37.950	-77.957	6.2	-1.02
2011/09/02	19:07:51.95	37.948	-77.956	0.4	-1.25
2011/09/02	19:08:09.45	37.953	-77.957	7.1	-1.25
2011/09/02	19:08:10.96	37.951	-77.956	0.0	-1.12
2011/09/02	19:40:14.99	37.917	-77.907	7.7	-0.78
2011/09/02	19:48:23.95	37.912	-77.916	8.4	-0.91
2011/09/02	19:49:16.84	37.963	-77.991	9.0	-0.16
2011/09/02	20:33:00.59	37.925	-77.994	8.7	-0.97
2011/09/02	20:33:02.45	37.938	-78.014	5.2	-0.91
2011/09/02	21:24:23.77	37.924	-77.917	8.9	-0.71
2011/09/02	21:45:06.43	37.920	-77.948	9.0	-0.82
2011/09/02	21:52:08.05	37.914	-77.919	6.9	-0.35
2011/09/02	21:55:16.81	37.909	-77.934	8.7	-0.57
2011/09/02	22:28:34.01	37.892	-77.969	3.0	-1.58
2011/09/02	22:41:16.74	37.935	-77.939	5.2	-0.66
2011/09/03	17:05:45.11	37.942	-77.923	4.2	-0.96
2011/09/03	17:11:59.06	37.909	-77.969	2.6	-1.17
2011/09/03	17:15:51.70	37.939	-77.967	2.4	-0.97
2011/09/03	17:21:21.77	37.974	-78.017	6.5	-0.71

* z_0 = −0.4 km

The AIDA Backprojection Earthquake Catalog

Date (YYYY/MM/DD)	**Time (HH:MM:SS)**	**Latitude (°N)**	**Longitude (°E)**	**Depth (km)**	**Magnitude (M_{BPI})**
2011/09/03	17:26:21.74	37.975	-78.001	3.1	0.23
2011/09/03	17:46:18.32	37.976	-77.987	9.0	-0.21
2011/09/03	17:50:51.81	37.926	-77.911	0.6	-0.78
2011/09/03	17:56:22.14	37.967	-77.980	4.2	-0.67
2011/09/03	18:00:36.90	37.965	-77.989	1.6	-0.68
2011/09/03	18:18:42.82	37.973	-77.986	8.2	-0.02
2011/09/03	18:29:47.97	37.928	-77.984	4.7	-0.82
2011/09/03	18:33:37.48	37.922	-77.918	0.1	-1.08
2011/09/03	18:36:14.29	37.929	-77.981	1.9	-1.08
2011/09/03	18:43:38.95	37.958	-77.945	1.6	-1.23
2011/09/03	18:45:26.56	37.921	-77.909	7.7	-0.89
2011/09/03	18:53:56.79	37.921	-77.993	0.7	-1.13
2011/09/03	18:56:52.07	37.915	-77.980	0.8	-1.31
2011/09/03	19:02:59.00	37.939	-77.962	2.0	-1.02
2011/09/03	19:05:49.10	37.939	-77.978	4.6	-0.12
2011/09/03	19:08:15.27	37.939	-77.986	4.2	-0.56
2011/09/03	19:13:31.47	37.960	-77.990	1.2	-1.03
2011/09/03	19:26:10.48	37.943	-77.990	2.5	0.17
2011/09/03	19:30:48.90	37.924	-77.985	5.1	0.16
2011/09/03	19:42:44.22	37.937	-78.015	0.5	-1.18
2011/09/03	19:46:23.44	37.935	-78.015	1.1	-0.15
2011/09/03	20:01:11.66	37.935	-78.017	1.9	-1.14
2011/09/03	20:05:41.19	37.959	-77.978	1.3	-1.21
2011/09/03	20:11:54.71	37.947	-77.974	4.9	0.51
2011/09/03	20:24:48.42	37.940	-77.989	2.1	-1.46
2011/09/03	20:25:43.62	37.942	-77.986	3.7	-0.75
2011/09/03	20:28:44.14	37.915	-77.992	1.6	-0.77
2011/09/03	20:37:15.68	37.967	-77.929	6.0	0.22
2011/09/03	20:50:31.61	37.918	-77.916	0.5	-0.80
2011/09/03	20:51:19.54	37.942	-77.986	3.3	-0.16
2011/09/03	21:10:53.27	37.948	-77.969	5.9	1.73
2011/09/03	21:25:22.74	37.954	-77.949	6.1	0.22
2011/09/03	21:55:29.49	37.949	-77.964	5.1	-0.89
2011/09/03	22:02:21.10	37.917	-77.994	3.9	0.54
2011/09/03	22:04:40.56	37.938	-77.977	5.4	-0.56
2011/09/03	22:12:59.18	37.949	-77.973	4.7	1.17
2011/09/03	22:14:49.53	37.919	-77.992	4.4	-0.96
2011/09/03	22:23:12.01	37.941	-77.993	1.9	-1.15
2011/09/03	22:38:07.75	37.916	-77.989	4.9	0.24
2011/09/03	22:41:22.07	37.929	-77.981	5.1	-0.90

* z_0 = −0.4 km

The AIDA Backprojection Earthquake Catalog

Date (YYYY/MM/DD)	**Time (HH:MM:SS)**	**Latitude (°N)**	**Longitude (°E)**	**Depth (km)**	**Magnitude (M_{BPI})**
2011/09/03	22:41:23.27	37.930	-77.983	0.9	-0.89
2011/09/03	22:42:05.83	37.925	-77.983	0.2	-1.09
2011/09/03	22:42:19.76	37.932	-77.976	2.0	-0.93
2011/09/03	22:50:37.82	37.939	-77.986	4.5	-0.22
2011/09/03	23:34:09.48	37.915	-77.995	3.8	0.79
2011/09/03	23:56:28.90	37.950	-77.973	4.5	-0.79
2011/09/03	23:56:29.98	37.946	-77.975	0.6	-0.98
2011/09/03	23:59:24.18	37.932	-77.984	4.2	-0.90
2011/09/03	23:59:25.17	37.933	-77.990	1.1	-0.95
2011/09/04	00:36:35.79	37.928	-77.985	4.3	-0.11
2011/09/04	01:28:50.26	37.956	-78.005	-0.2	-1.07
2011/09/04	01:46:08.09	37.933	-77.982	4.5	-0.64
2011/09/04	01:54:48.83	37.901	-77.974	7.6	-0.07
2011/09/04	01:57:21.78	37.943	-77.991	2.6	-1.25
2011/09/04	01:58:03.31	37.911	-77.993	5.6	0.94
2011/09/04	02:26:31.84	37.921	-77.992	3.8	-0.78
2011/09/04	02:26:32.65	37.923	-77.993	1.7	-1.10
2011/09/04	02:29:37.73	37.944	-77.961	6.0	-0.92
2011/09/04	02:29:39.07	37.941	-77.966	1.7	-1.07
2011/09/04	02:35:38.96	37.921	-77.997	3.8	-1.06
2011/09/04	02:49:11.69	37.907	-77.989	6.0	0.08
2011/09/04	03:08:40.70	37.921	-77.975	6.2	0.53
2011/09/04	03:11:38.72	37.958	-78.001	0.6	-0.80
2011/09/04	03:14:27.68	37.903	-78.002	0.4	-1.03
2011/09/04	03:19:37.07	37.965	-77.946	5.4	-0.92
2011/09/04	03:20:07.28	37.957	-77.973	2.8	-1.22
2011/09/04	03:42:22.11	37.888	-78.002	0.1	-0.34
2011/09/04	03:44:09.80	37.922	-77.997	3.4	-0.16
2011/09/04	04:03:07.90	37.958	-77.995	1.5	-1.00
2011/09/04	04:37:15.09	37.937	-77.978	1.6	-0.98
2011/09/04	04:52:51.41	37.941	-77.981	4.6	-0.45
2011/09/04	04:57:37.77	37.955	-77.984	2.8	-1.20
2011/09/04	04:59:40.97	37.948	-77.966	5.7	-0.94
2011/09/04	04:59:42.24	37.943	-77.968	1.6	-0.98
2011/09/04	05:41:08.74	37.912	-77.928	-0.1	-0.49
2011/09/04	06:43:34.97	37.906	-78.003	4.4	-0.64
2011/09/04	06:45:25.03	37.938	-77.986	4.3	-0.94
2011/09/04	06:45:26.11	37.937	-77.993	0.3	-1.22
2011/09/04	07:00:01.13	37.901	-77.976	7.9	0.21
2011/09/04	07:21:35.38	37.912	-77.917	0.0	-0.96

* z_0 = −0.4 km

The AIDA Backprojection Earthquake Catalog

Date (YYYY/MM/DD)	**Time (HH:MM:SS)**	**Latitude (°N)**	**Longitude (°E)**	**Depth (km)**	**Magnitude (M_{BPI})**
2011/09/04	07:22:35.57	37.941	-77.968	5.8	-0.26
2011/09/04	07:24:52.16	37.926	-77.987	3.9	1.03
2011/09/04	07:33:59.50	37.923	-77.993	3.7	-0.53
2011/09/04	07:46:12.18	37.967	-77.935	5.5	-0.41
2011/09/04	07:47:05.13	37.920	-77.994	3.4	-0.76
2011/09/04	07:51:32.84	37.943	-77.986	3.7	-0.55
2011/09/04	07:56:19.53	37.908	-78.005	3.6	-1.39
2011/09/04	07:59:56.08	37.934	-77.984	4.2	0.75
2011/09/04	08:35:32.41	37.934	-77.967	5.5	-0.96
2011/09/04	08:35:33.70	37.934	-77.967	1.3	-1.22
2011/09/04	08:47:18.63	37.950	-77.975	4.2	-0.92
2011/09/04	08:50:14.03	37.967	-77.935	5.8	-0.52
2011/09/04	08:56:13.86	37.912	-77.923	0.1	-0.85
2011/09/04	09:06:25.42	37.942	-77.968	5.9	-1.08
2011/09/04	09:06:26.77	37.943	-77.969	1.4	-1.14
2011/09/04	09:11:30.20	37.939	-77.989	4.1	-1.26
2011/09/04	09:15:45.49	37.951	-77.951	6.4	-0.62
2011/09/04	09:27:23.30	37.933	-77.986	1.0	-1.00
2011/09/04	09:43:07.95	37.930	-77.969	6.3	-0.85
2011/09/04	09:43:09.33	37.928	-77.975	1.6	-0.95
2011/09/04	10:14:44.72	37.866	-77.978	7.8	-0.41
2011/09/04	10:21:17.97	37.912	-77.924	-0.1	-0.78
2011/09/04	10:25:43.50	37.903	-78.001	4.9	-1.05
2011/09/04	10:27:21.28	37.930	-77.982	4.9	-0.18
2011/09/04	10:30:24.73	37.918	-77.994	3.8	-0.70
2011/09/04	10:43:13.87	37.926	-77.990	6.8	-0.93
2011/09/04	10:43:15.24	37.925	-77.991	1.9	-0.95
2011/09/04	11:01:18.17	37.939	-77.984	4.4	0.07
2011/09/04	11:19:26.52	37.950	-77.976	3.7	-0.88
2011/09/04	12:27:35.15	37.948	-77.980	3.3	-1.00
2011/09/04	12:58:54.27	37.964	-77.975	3.4	-0.90
2011/09/04	13:04:32.43	37.911	-77.968	9.0	0.32
2011/09/04	13:04:43.28	37.911	-77.969	8.5	0.75
2011/09/04	13:09:17.07	37.909	-78.005	3.4	-0.70
2011/09/04	13:37:02.74	37.910	-77.997	5.1	0.40
2011/09/04	13:57:41.94	37.945	-77.965	5.9	0.10
2011/09/04	14:22:50.13	37.939	-77.989	4.7	0.20
2011/09/04	14:28:20.88	37.968	-77.932	5.5	-0.77
2011/09/04	14:34:25.33	37.939	-77.992	1.9	-1.35
2011/09/04	14:42:56.81	37.903	-78.001	4.7	-0.65

* z_0 = −0.4 km

The AIDA Backprojection Earthquake Catalog

Date (YYYY/MM/DD)	**Time (HH:MM:SS)**	**Latitude (°N)**	**Longitude (°E)**	**Depth (km)**	**Magnitude (M_{BPI})**
2011/09/04	15:15:05.60	37.930	-77.982	5.1	-0.99
2011/09/04	15:15:30.50	37.942	-77.993	1.9	-1.16
2011/09/04	15:32:58.11	37.923	-77.987	4.7	-0.80
2011/09/04	16:06:04.80	37.910	-77.924	0.2	-0.90
2011/09/04	16:08:35.03	37.934	-77.983	4.6	0.17
2011/09/04	16:18:52.97	37.941	-77.993	2.0	-1.15
2011/09/04	16:25:41.30	37.912	-77.998	4.1	-0.06
2011/09/04	17:17:46.10	37.939	-77.986	4.4	-0.88
2011/09/04	17:26:51.32	37.939	-77.986	4.5	1.20
2011/09/04	17:36:25.76	37.941	-77.966	5.8	-0.37
2011/09/04	17:37:56.48	37.940	-77.982	3.8	0.62
2011/09/04	17:48:19.45	37.935	-77.985	4.2	-0.72
2011/09/04	17:49:41.58	37.951	-77.972	4.1	0.40
2011/09/04	17:51:35.76	37.942	-77.984	4.1	0.01
2011/09/04	18:04:11.01	37.957	-77.960	4.9	-0.53
2011/09/04	18:10:18.69	37.933	-77.985	4.4	-0.94
2011/09/04	18:10:19.71	37.931	-77.990	1.3	-0.79
2011/09/04	18:44:30.54	37.950	-77.951	6.5	0.58
2011/09/04	19:09:07.72	37.903	-77.999	5.1	0.11
2011/09/04	19:51:25.47	37.943	-77.957	6.4	-0.41
2011/09/04	20:05:19.49	37.943	-77.991	2.4	0.96
2011/09/04	20:07:12.41	37.958	-77.964	3.9	-0.80
2011/09/04	21:08:35.82	37.930	-77.984	3.5	-1.05
2011/09/04	21:22:45.25	37.966	-77.937	7.0	-0.61
2011/09/04	21:35:36.60	37.912	-78.014	0.4	-0.90
2011/09/04	22:06:09.66	37.949	-77.909	0.2	-0.36
2011/09/04	22:09:41.58	37.906	-77.999	5.0	-0.53
2011/09/04	22:40:35.95	37.912	-77.998	4.1	-0.35
2011/09/04	22:49:25.18	37.954	-77.976	1.5	-1.10
2011/09/04	22:52:33.12	37.950	-77.970	5.5	-0.74
2011/09/04	23:12:26.88	37.921	-77.993	3.2	-0.38
2011/09/04	23:14:08.66	37.950	-77.975	3.8	-1.00
2011/09/04	23:27:47.50	37.953	-77.962	5.4	-0.39
2011/09/05	00:13:19.16	37.922	-77.992	4.0	0.09
2011/09/05	00:44:44.81	37.922	-77.990	4.5	1.35
2011/09/05	00:47:21.82	37.911	-77.984	6.3	-0.24
2011/09/05	00:55:23.85	37.940	-77.986	4.3	-0.18
2011/09/05	01:55:23.09	37.940	-77.982	4.0	-0.93
2011/09/05	02:14:38.69	37.952	-77.950	0.5	-0.33
2011/09/05	02:46:00.61	37.933	-77.985	4.1	-0.44

* z_0 = −0.4 km

The AIDA Backprojection Earthquake Catalog

Date (YYYY/MM/DD)	**Time (HH:MM:SS)**	**Latitude (°N)**	**Longitude (°E)**	**Depth (km)**	**Magnitude (M_{BPI})**
2011/09/05	03:13:40.12	37.943	-78.017	0.3	-1.06
2011/09/05	03:29:55.77	37.948	-77.982	2.9	-1.31
2011/09/05	03:44:04.75	37.961	-77.991	1.3	-0.91
2011/09/05	04:03:49.28	37.917	-77.914	0.4	-1.17
2011/09/05	04:19:11.56	37.932	-77.983	4.7	0.35
2011/09/05	04:22:06.87	37.948	-77.970	5.7	-0.81
2011/09/05	04:40:53.21	37.946	-78.009	-0.2	-1.37
2011/09/05	04:45:22.28	37.932	-77.981	4.7	-0.02
2011/09/05	05:04:18.06	37.946	-77.986	2.4	-1.21
2011/09/05	06:12:42.37	37.940	-77.984	4.6	0.45
2011/09/05	06:18:21.73	37.917	-77.990	2.1	-1.19
2011/09/05	06:22:13.11	37.923	-77.997	3.3	-0.76
2011/09/05	06:41:16.95	37.948	-77.984	2.7	-0.53
2011/09/05	06:41:43.85	37.925	-77.987	4.3	0.28
2011/09/05	06:43:16.88	37.931	-77.984	4.7	-0.78
2011/09/05	06:56:07.83	37.950	-77.940	6.9	0.50
2011/09/05	07:06:44.15	37.946	-77.989	1.9	-1.18
2011/09/05	07:15:34.96	37.949	-77.965	6.1	-0.20
2011/09/05	07:20:53.92	37.937	-77.974	5.6	-1.01
2011/09/05	07:21:46.94	37.945	-77.973	2.5	-1.14
2011/09/05	07:35:22.71	37.933	-77.984	4.6	-0.56
2011/09/05	07:45:58.37	37.941	-77.983	4.6	-0.38
2011/09/05	07:59:27.80	37.966	-77.940	5.3	-0.82
2011/09/05	07:59:29.14	37.962	-77.949	-0.2	-1.06
2011/09/05	08:17:13.64	37.917	-78.010	-0.1	-1.11
2011/09/05	08:18:02.64	37.939	-77.982	4.1	0.51
2011/09/05	08:22:10.09	37.944	-77.983	3.8	-0.82
2011/09/05	08:28:57.43	37.939	-77.991	3.7	-0.22
2011/09/05	08:41:30.94	37.938	-77.970	5.6	-0.64
2011/09/05	08:52:10.23	37.929	-77.990	4.2	0.62
2011/09/05	09:43:17.45	37.939	-77.966	6.2	0.53
2011/09/05	10:34:15.37	37.945	-77.989	2.4	-1.10
2011/09/05	10:57:31.14	37.940	-77.947	3.2	-1.09
2011/09/05	11:25:58.97	37.919	-77.993	4.1	-1.07
2011/09/05	11:32:51.54	37.941	-77.965	5.5	-0.62
2011/09/05	11:35:59.90	37.961	-77.998	0.9	-0.50
2011/09/05	11:47:08.64	37.941	-77.991	0.8	-1.44
2011/09/05	11:51:18.85	37.934	-77.985	4.3	-0.82
2011/09/05	12:05:11.23	37.940	-77.985	4.6	-0.84
2011/09/05	12:35:54.03	37.959	-77.999	0.7	-0.84

* z_0 = −0.4 km

The AIDA Backprojection Earthquake Catalog

Date (YYYY/MM/DD)	**Time (HH:MM:SS)**	**Latitude (°N)**	**Longitude (°E)**	**Depth (km)**	**Magnitude (M_{BPI})**
2011/09/05	12:38:13.10	37.958	-77.965	3.2	-0.85
2011/09/05	12:41:33.91	37.934	-77.983	4.0	-0.22
2011/09/05	13:00:53.73	37.913	-77.999	4.3	-0.57
2011/09/05	13:00:54.78	37.913	-78.000	0.8	-0.84
2011/09/05	13:31:50.14	37.932	-77.985	3.9	1.31
2011/09/05	14:12:47.86	37.932	-77.985	3.8	-0.12
2011/09/05	14:24:13.38	37.893	-78.001	0.2	-0.75
2011/09/05	14:26:13.42	37.912	-77.994	4.9	-0.87
2011/09/05	14:26:14.59	37.914	-77.995	0.5	-0.58
2011/09/05	14:39:39.33	37.948	-77.973	4.5	-0.48
2011/09/05	14:40:48.97	37.940	-77.985	3.7	-0.44
2011/09/05	14:52:32.83	37.922	-77.980	5.3	-0.06
2011/09/05	14:58:22.34	37.957	-77.960	4.7	0.24
2011/09/05	15:03:46.35	37.970	-77.975	4.7	-0.66
2011/09/05	15:07:48.72	37.923	-77.989	4.2	-0.65
2011/09/05	15:26:59.64	37.935	-78.017	2.1	-0.92
2011/09/05	15:39:12.74	37.948	-77.980	3.2	-1.09
2011/09/05	15:54:20.32	37.957	-78.001	0.4	-0.34
2011/09/05	16:00:30.70	37.922	-77.989	4.0	-0.49
2011/09/05	16:04:20.09	37.941	-77.986	3.3	-0.38
2011/09/05	16:18:21.57	37.953	-77.985	2.7	0.20
2011/09/05	16:38:22.33	37.916	-78.018	0.5	-0.55
2011/09/05	16:54:24.51	37.948	-77.969	5.5	2.79
2011/09/05	16:56:32.90	37.948	-77.968	5.3	-0.62
2011/09/05	16:57:27.76	37.966	-77.931	5.9	-0.75
2011/09/05	17:00:01.27	37.948	-77.969	5.9	0.50
2011/09/05	17:01:29.03	37.948	-77.968	5.5	-0.80
2011/09/05	17:06:11.88	37.948	-77.970	5.6	1.13
2011/09/05	17:26:14.17	37.921	-77.990	4.7	0.81
2011/09/05	17:31:07.91	37.935	-77.986	4.1	-0.58
2011/09/05	17:39:05.51	37.949	-77.968	5.5	-0.66
2011/09/05	17:43:24.49	37.898	-77.972	8.4	-0.34
2011/09/05	17:47:52.95	37.936	-77.983	3.7	-0.67
2011/09/05	18:21:45.27	37.923	-77.993	3.6	0.08
2011/09/05	18:53:34.75	37.933	-77.983	4.6	-0.51
2011/09/05	19:42:42.22	37.939	-77.989	4.3	1.64
2011/09/05	20:15:00.78	37.939	-77.966	5.3	-0.95
2011/09/05	20:18:50.75	37.943	-78.018	0.7	-0.54
2011/09/05	20:46:49.78	37.959	-77.957	4.4	-0.99
2011/09/05	20:47:08.62	37.948	-77.969	5.4	-0.45

* z_0 = −0.4 km

The AIDA Backprojection Earthquake Catalog

Date (YYYY/MM/DD)	**Time (HH:MM:SS)**	**Latitude (°N)**	**Longitude (°E)**	**Depth (km)**	**Magnitude (M_{BPI})**
2011/09/05	20:52:26.85	37.912	-77.997	4.3	-0.23
2011/09/05	21:33:59.12	37.961	-77.962	3.6	-0.92
2011/09/05	21:42:50.76	37.969	-77.925	5.9	-0.76
2011/09/05	21:56:49.97	37.886	-77.970	8.3	-0.64
2011/09/05	21:56:51.87	37.887	-77.973	-0.2	-0.68
2011/09/05	22:01:14.24	37.948	-77.968	5.6	-0.29
2011/09/05	22:13:10.15	37.949	-77.968	5.7	-0.02
2011/09/05	22:17:15.33	37.932	-77.985	3.9	0.33
2011/09/05	22:27:30.30	37.948	-77.970	5.9	-0.77
2011/09/05	22:27:31.51	37.947	-77.966	1.2	-0.94
2011/09/05	22:51:31.30	37.929	-77.989	4.2	0.31
2011/09/05	22:54:58.98	37.948	-77.973	4.4	-1.41
2011/09/05	22:55:00.05	37.945	-77.976	1.0	-1.07
2011/09/05	23:10:06.30	37.928	-77.986	4.3	-0.61
2011/09/05	23:40:39.18	37.948	-77.958	6.1	-0.71
2011/09/05	23:41:04.04	37.948	-77.969	5.8	0.81
2011/09/06	00:17:38.96	37.933	-77.972	5.9	-0.69
2011/09/06	00:17:40.24	37.930	-77.975	1.9	-0.89
2011/09/06	00:26:56.59	37.946	-77.989	2.1	-1.03
2011/09/06	00:30:05.33	37.903	-78.001	5.1	0.76
2011/09/06	00:33:03.54	37.959	-77.948	6.1	-0.53
2011/09/06	00:40:06.70	37.954	-77.977	2.6	-0.91
2011/09/06	00:56:14.08	37.933	-77.984	4.0	1.31
2011/09/06	01:08:47.27	37.948	-77.968	5.4	0.40
2011/09/06	01:14:35.83	37.939	-77.987	4.0	-0.22
2011/09/06	02:05:24.19	37.957	-77.965	4.2	0.20
2011/09/06	02:13:44.13	37.929	-77.970	6.0	0.20
2011/09/06	02:16:29.51	37.951	-77.962	6.0	-0.64
2011/09/06	02:30:47.41	37.948	-77.969	5.4	0.82
2011/09/06	02:33:53.09	37.914	-78.009	0.6	-1.12
2011/09/06	02:48:27.60	37.912	-77.922	0.4	-0.33
2011/09/06	02:49:23.17	37.912	-78.009	2.9	-1.06
2011/09/06	03:08:38.74	37.918	-78.007	-0.2	-0.97
2011/09/06	03:10:20.85	37.943	-77.975	5.2	-0.77
2011/09/06	03:24:49.15	37.958	-78.000	0.4	-0.75
2011/09/06	03:28:07.14	37.921	-77.995	3.3	-0.52
2011/09/06	03:29:08.02	37.910	-78.000	4.0	-0.97
2011/09/06	03:29:08.99	37.911	-78.001	0.8	-0.99
2011/09/06	03:37:03.10	37.941	-77.987	3.7	0.18
2011/09/06	04:22:26.18	37.948	-77.956	6.9	-0.32

* z_0 = −0.4 km

The AIDA Backprojection Earthquake Catalog

Date (YYYY/MM/DD)	**Time (HH:MM:SS)**	**Latitude (°N)**	**Longitude (°E)**	**Depth (km)**	**Magnitude (M_{BPI})**
2011/09/06	04:46:33.18	37.903	-78.006	5.6	-0.49
2011/09/06	04:46:34.43	37.903	-78.002	1.1	-0.45
2011/09/06	04:53:50.28	37.959	-77.946	7.3	1.39
2011/09/06	05:41:06.21	37.940	-77.992	1.9	0.06
2011/09/06	06:10:29.67	37.963	-77.993	1.5	-0.91
2011/09/06	06:16:36.20	37.909	-77.992	2.0	-0.95
2011/09/06	06:23:47.52	37.954	-77.974	3.0	-0.51
2011/09/06	06:36:41.52	37.949	-77.974	4.9	-0.46
2011/09/06	07:31:45.36	37.951	-77.966	5.3	0.82
2011/09/06	07:57:52.25	37.932	-77.989	0.6	-1.10
2011/09/06	08:07:53.12	37.921	-77.990	4.4	-0.95
2011/09/06	09:00:43.26	37.919	-77.992	4.2	0.83
2011/09/06	09:05:23.23	37.942	-77.952	6.5	-0.48
2011/09/06	09:05:24.74	37.942	-77.950	0.2	-0.72
2011/09/06	09:32:44.50	37.924	-77.987	5.0	-0.33
2011/09/06	09:48:24.55	37.953	-77.960	5.5	-0.73
2011/09/06	09:48:25.86	37.948	-77.967	1.4	-0.86
2011/09/06	09:53:03.53	37.942	-77.983	3.7	-0.59
2011/09/06	10:25:03.52	37.946	-77.986	2.8	-0.66
2011/09/06	10:43:04.37	37.934	-77.981	4.9	1.47
2011/09/06	10:52:12.71	37.952	-78.011	0.1	-0.85
2011/09/06	11:00:23.86	37.958	-77.999	0.4	-0.43
2011/09/06	11:36:24.29	37.931	-77.981	5.0	0.63
2011/09/06	11:56:35.37	37.926	-77.989	3.7	0.01
2011/09/06	12:44:47.70	37.956	-77.991	1.7	-0.67
2011/09/06	12:46:34.84	37.966	-77.935	5.6	1.06
2011/09/06	12:52:26.57	37.966	-77.974	3.6	-0.51
2011/09/06	13:15:12.06	37.932	-77.985	3.6	-0.07
2011/09/06	13:21:53.26	37.935	-77.984	3.7	0.80
2011/09/06	14:42:09.59	37.898	-77.994	8.9	0.09
2011/09/06	14:42:53.90	37.907	-77.909	0.4	-0.56
2011/09/06	14:46:33.34	37.960	-77.952	4.4	-0.58
2011/09/06	15:06:22.15	37.899	-77.998	3.0	-1.01
2011/09/06	15:24:08.96	37.963	-77.987	1.4	-0.47
2011/09/06	15:25:47.22	37.944	-77.975	2.1	-0.70
2011/09/06	15:43:23.59	37.909	-77.911	0.8	0.75
2011/09/06	15:50:44.00	37.912	-77.980	6.3	-0.02
2011/09/06	16:23:26.89	37.966	-77.935	5.6	0.18
2011/09/06	16:27:40.10	37.928	-78.001	1.7	0.35
2011/09/06	17:06:38.48	37.945	-77.989	2.3	1.98

* z_0 = −0.4 km

The AIDA Backprojection Earthquake Catalog

Date (YYYY/MM/DD)	**Time (HH:MM:SS)**	**Latitude (°N)**	**Longitude (°E)**	**Depth (km)**	**Magnitude (M_{BPI})**
2011/09/06	17:18:33.06	37.932	-77.984	4.2	0.67
2011/09/06	17:19:56.77	37.936	-77.987	3.9	-0.84
2011/09/06	17:25:21.70	37.902	-77.998	5.5	0.81
2011/09/06	17:39:41.34	37.939	-77.965	6.2	0.75
2011/09/06	17:55:36.49	37.952	-77.944	6.8	-0.20
2011/09/06	17:55:38.07	37.945	-77.947	1.4	-0.54
2011/09/06	17:55:40.85	37.967	-77.936	5.5	-0.35
2011/09/06	17:58:44.56	37.948	-77.969	5.7	-0.06
2011/09/06	18:00:21.27	37.931	-77.984	4.6	0.16
2011/09/06	18:02:17.86	37.948	-77.968	5.7	-0.48
2011/09/06	18:46:23.91	37.949	-77.974	4.9	-0.60
2011/09/06	18:51:23.16	37.946	-77.989	2.5	0.90
2011/09/06	19:05:13.44	37.949	-77.965	6.1	-0.14
2011/09/06	19:16:36.16	37.939	-78.015	-0.1	-0.73
2011/09/06	19:30:03.77	37.921	-77.993	3.3	-0.04
2011/09/06	19:40:24.55	37.919	-78.015	0.2	-0.51
2011/09/06	19:41:27.48	37.948	-77.976	4.3	-0.73
2011/09/06	19:42:05.87	37.938	-77.964	4.8	-0.77
2011/09/06	20:07:18.36	37.978	-77.942	4.7	-0.84
2011/09/06	21:08:56.05	37.922	-77.917	9.0	-0.09
2011/09/06	21:17:53.62	37.937	-77.964	6.5	1.93
2011/09/06	22:38:08.69	37.954	-77.977	2.5	-0.77
2011/09/06	22:42:23.29	37.939	-77.980	4.9	-0.73
2011/09/06	22:43:16.59	37.949	-77.967	5.6	-0.76
2011/09/06	23:14:09.29	37.935	-77.986	4.0	-0.36
2011/09/07	00:06:01.67	37.925	-77.987	4.2	0.35
2011/09/07	00:08:45.40	37.946	-77.981	3.4	-0.76
2011/09/07	00:21:04.15	37.930	-77.982	3.6	-1.26
2011/09/07	00:23:12.25	37.918	-77.994	1.3	-1.17
2011/09/07	01:08:35.67	37.958	-78.002	0.3	-0.00
2011/09/07	01:46:00.93	37.933	-77.989	0.9	-0.79
2011/09/07	01:46:23.31	37.935	-77.986	3.8	-0.55
2011/09/07	02:04:49.35	37.914	-77.995	4.0	-0.77
2011/09/07	02:07:05.55	37.914	-77.923	0.5	-0.48
2011/09/07	02:34:05.50	37.968	-77.933	6.7	1.78
2011/09/07	02:42:33.92	37.948	-77.968	5.8	1.18
2011/09/07	02:47:31.07	37.927	-77.985	3.4	0.06
2011/09/07	03:19:23.03	37.956	-77.999	0.2	-1.25
2011/09/07	03:49:25.10	37.931	-77.973	1.3	-0.87
2011/09/07	03:53:10.87	37.967	-77.978	3.6	-0.80

* z_0 = −0.4 km

The AIDA Backprojection Earthquake Catalog

Date (YYYY/MM/DD)	**Time (HH:MM:SS)**	**Latitude (°N)**	**Longitude (°E)**	**Depth (km)**	**Magnitude (M_{BPI})**
2011/09/07	05:08:16.53	37.930	-77.985	4.3	-0.84
2011/09/07	05:12:33.10	37.919	-77.919	0.6	-1.00
2011/09/07	05:22:04.99	37.957	-77.983	2.8	-1.05
2011/09/07	05:45:00.26	37.902	-77.973	8.9	0.59
2011/09/07	05:56:43.64	37.958	-77.946	6.4	1.96
2011/09/07	06:10:49.71	37.944	-77.969	5.4	-0.77
2011/09/07	06:10:50.99	37.941	-77.970	1.0	-0.85
2011/09/07	07:30:28.09	37.949	-77.978	3.2	-0.85
2011/09/07	08:06:10.37	37.948	-77.965	5.7	-0.28
2011/09/07	08:30:42.45	37.955	-78.001	0.3	-1.11
2011/09/07	09:54:18.99	37.921	-77.997	3.1	-0.44
2011/09/07	10:14:10.90	37.936	-77.961	5.9	-0.96
2011/09/07	10:14:12.16	37.934	-77.965	2.3	-0.90
2011/09/07	10:27:58.90	37.944	-77.991	2.2	-0.14
2011/09/07	10:34:17.40	37.950	-77.965	5.7	-0.19
2011/09/07	10:36:47.11	37.938	-77.952	6.6	-0.41
2011/09/07	10:49:44.44	37.909	-77.994	5.0	1.17
2011/09/07	11:13:24.38	37.952	-77.966	1.2	-0.81
2011/09/07	11:19:42.09	37.939	-77.973	2.2	-0.81
2011/09/07	11:24:54.89	37.944	-77.976	4.7	-0.86
2011/09/07	11:24:55.90	37.943	-77.978	1.8	-0.94
2011/09/07	11:28:14.88	37.943	-77.980	3.6	-0.27
2011/09/07	11:42:57.56	37.921	-77.991	4.1	0.11
2011/09/07	11:56:05.02	37.965	-77.946	5.0	0.47
2011/09/07	12:02:30.62	37.974	-77.974	4.8	1.05
2011/09/07	12:04:02.56	37.926	-77.992	3.8	-0.96
2011/09/07	12:32:27.45	37.935	-77.983	4.1	-0.24
2011/09/07	12:54:27.82	37.957	-77.964	3.7	-0.21
2011/09/07	13:13:08.09	37.909	-77.917	4.8	-0.91
2011/09/07	13:35:20.81	37.930	-77.981	5.1	-0.13
2011/09/07	13:49:39.34	37.944	-77.991	2.2	-0.35
2011/09/07	13:50:05.85	37.958	-77.954	5.3	-0.08
2011/09/07	14:38:04.09	37.949	-77.974	4.7	-0.58
2011/09/07	15:20:37.55	37.915	-77.995	3.9	-0.53
2011/09/07	15:28:24.23	37.952	-77.960	6.1	1.02
2011/09/07	15:28:41.94	37.951	-77.960	6.2	-0.27
2011/09/07	15:34:44.87	37.942	-77.982	3.5	1.88
2011/09/07	16:17:09.00	37.934	-77.982	4.4	-0.32
2011/09/07	16:28:38.37	37.926	-77.990	4.0	-0.87
2011/09/07	16:46:45.40	37.949	-77.972	4.6	-0.76

* z_0 = −0.4 km

The AIDA Backprojection Earthquake Catalog

Date (YYYY/MM/DD)	**Time (HH:MM:SS)**	**Latitude (°N)**	**Longitude (°E)**	**Depth (km)**	**Magnitude (M_{BPI})**
2011/09/07	17:03:01.92	37.943	-77.939	8.2	-0.36
2011/09/07	17:18:16.71	37.933	-77.989	4.0	-0.97
2011/09/07	17:18:18.78	37.911	-77.924	0.4	-0.45
2011/09/07	17:19:33.26	37.930	-77.986	4.1	-0.78
2011/09/07	17:27:42.05	37.921	-77.990	4.5	-0.69
2011/09/07	17:29:38.00	37.944	-77.977	1.2	-1.20
2011/09/07	17:55:21.59	37.962	-77.993	1.2	-1.11
2011/09/07	17:55:44.58	37.930	-77.910	4.1	0.17
2011/09/07	18:33:14.35	37.930	-77.986	4.1	-0.51
2011/09/07	18:35:17.50	37.898	-77.987	0.5	-0.94
2011/09/07	18:41:52.67	37.957	-77.967	3.1	0.85
2011/09/07	18:45:56.07	37.963	-77.992	1.4	-0.83
2011/09/07	18:55:24.92	37.912	-77.923	0.1	-0.65
2011/09/07	19:29:38.23	37.916	-77.920	0.3	-0.11
2011/09/07	19:30:07.78	37.919	-77.914	-0.2	-0.67
2011/09/07	19:33:43.17	37.915	-77.922	0.2	-0.38
2011/09/07	19:38:49.63	37.919	-77.916	0.3	-0.96
2011/09/07	20:08:34.83	37.941	-77.985	3.1	-0.32
2011/09/07	20:13:57.88	37.920	-77.917	0.7	-0.88
2011/09/07	20:19:32.85	37.947	-77.944	6.6	-0.73
2011/09/07	20:19:34.39	37.946	-77.944	0.4	-0.81
2011/09/07	20:38:42.13	37.939	-77.975	4.8	-0.49
2011/09/07	20:38:43.27	37.941	-77.975	1.4	-0.78
2011/09/07	21:23:17.96	37.953	-77.960	5.2	-0.56
2011/09/07	21:23:19.17	37.948	-77.967	1.8	-0.80
2011/09/07	21:47:53.38	37.957	-77.908	0.3	-0.82
2011/09/07	22:04:06.42	37.921	-77.990	4.6	0.37
2011/09/07	22:19:40.64	37.957	-77.907	-0.2	-0.70
2011/09/07	22:28:27.35	37.900	-77.965	4.5	-0.94
2011/09/07	22:28:28.32	37.900	-77.970	2.6	-0.82
2011/09/07	22:31:36.67	37.948	-77.941	7.2	-0.86
2011/09/07	23:42:01.34	37.905	-77.989	6.7	-0.69
2011/09/08	00:19:28.59	37.939	-77.989	4.2	1.66
2011/09/08	00:43:17.27	37.914	-77.957	9.0	-0.75
2011/09/08	00:43:19.06	37.916	-77.959	4.5	-0.89
2011/09/08	01:25:34.82	37.942	-77.968	5.8	-0.69
2011/09/08	01:25:36.12	37.941	-77.970	1.9	-1.03
2011/09/08	01:29:13.22	37.926	-77.991	3.9	-0.78
2011/09/08	01:41:21.23	37.933	-77.985	4.1	-1.09
2011/09/08	02:15:51.85	37.948	-77.975	4.5	-0.06

* z_0 = −0.4 km

The AIDA Backprojection Earthquake Catalog

Date (YYYY/MM/DD)	**Time (HH:MM:SS)**	**Latitude (°N)**	**Longitude (°E)**	**Depth (km)**	**Magnitude (M_{BPI})**
2011/09/08	02:25:10.80	37.948	-77.968	5.8	-0.40
2011/09/08	02:53:20.08	37.939	-77.972	5.6	-0.97
2011/09/08	02:53:21.34	37.938	-77.974	1.6	-1.10
2011/09/08	03:02:18.32	37.952	-77.977	2.8	-1.17
2011/09/08	03:03:52.97	37.958	-78.000	0.5	-0.46
2011/09/08	03:12:09.00	37.952	-77.974	4.0	-0.75
2011/09/08	03:18:36.34	37.936	-77.976	5.2	-0.84
2011/09/08	03:19:49.89	37.950	-77.970	5.4	-0.97
2011/09/08	03:19:54.72	37.946	-78.007	0.4	-1.09
2011/09/08	03:21:16.36	37.938	-77.981	4.5	-0.99
2011/09/08	03:33:52.82	37.954	-77.973	3.3	-0.64
2011/09/08	03:54:38.68	37.925	-77.990	3.5	-1.18
2011/09/08	03:58:28.60	37.948	-77.976	4.1	-1.09
2011/09/08	04:03:51.80	37.958	-77.999	0.4	-0.61
2011/09/08	04:32:17.17	37.922	-77.989	4.5	0.65
2011/09/08	04:44:10.01	37.948	-77.973	0.8	-1.01
2011/09/08	05:21:24.31	37.927	-77.987	4.0	-0.24
2011/09/08	05:27:30.57	37.921	-77.992	3.4	0.41
2011/09/08	05:54:12.22	37.958	-77.994	0.3	-0.27
2011/09/08	06:23:47.93	37.942	-77.957	5.9	-0.82
2011/09/08	06:34:23.30	37.934	-77.985	3.7	-0.66
2011/09/08	06:42:00.02	37.939	-77.981	3.5	0.12
2011/09/08	06:43:12.00	37.906	-77.992	6.0	-0.31
2011/09/08	06:57:40.15	37.924	-77.987	4.7	-0.85
2011/09/08	07:14:10.36	37.916	-77.921	0.2	-0.97
2011/09/08	07:19:07.38	37.938	-77.964	6.0	0.23
2011/09/08	07:27:55.03	37.958	-77.993	1.8	-0.85
2011/09/08	07:47:04.42	37.948	-77.959	1.9	-0.88
2011/09/08	07:51:27.68	37.941	-77.989	3.7	0.85
2011/09/08	08:20:47.95	37.940	-77.984	4.6	0.71
2011/09/08	08:42:33.68	37.955	-77.977	2.6	-0.94
2011/09/08	08:49:41.90	37.935	-77.985	4.2	-0.54
2011/09/08	09:01:07.99	37.935	-77.986	3.6	-1.08
2011/09/08	09:35:59.03	37.943	-77.991	2.5	-0.04
2011/09/08	09:43:42.92	37.929	-77.990	4.0	-1.13
2011/09/08	09:48:03.19	37.957	-78.001	0.0	-1.06
2011/09/08	09:49:00.69	37.927	-77.982	1.5	-1.17
2011/09/08	10:11:17.00	37.923	-77.990	4.1	-0.72
2011/09/08	10:33:04.81	37.897	-77.998	5.3	-0.74
2011/09/08	10:34:48.54	37.912	-77.992	1.3	-1.16

* z_0 = –0.4 km

The AIDA Backprojection Earthquake Catalog

Date (YYYY/MM/DD)	**Time (HH:MM:SS)**	**Latitude (°N)**	**Longitude (°E)**	**Depth (km)**	**Magnitude (M_{BPI})**
2011/09/08	10:55:43.41	37.948	-77.977	3.4	-1.06
2011/09/08	10:57:16.72	37.917	-78.000	3.4	0.16
2011/09/08	11:03:36.94	37.951	-77.949	6.5	-0.58
2011/09/08	11:06:29.92	37.918	-77.998	3.0	0.07
2011/09/08	11:15:44.76	37.921	-77.997	3.1	-0.41
2011/09/08	11:19:55.99	37.947	-78.017	0.2	-0.64
2011/09/08	11:38:17.71	37.941	-77.982	3.3	-0.18
2011/09/08	11:40:02.69	37.926	-77.989	3.9	0.95
2011/09/08	11:56:17.93	37.945	-77.993	0.2	-1.42
2011/09/08	12:02:29.47	37.948	-77.976	4.4	-0.32
2011/09/08	12:38:36.28	37.951	-77.972	5.6	-0.65
2011/09/08	12:41:34.78	37.955	-77.966	4.8	0.15
2011/09/08	13:01:19.53	37.940	-77.973	5.7	-0.90
2011/09/08	13:01:20.80	37.939	-77.974	1.3	-0.96
2011/09/08	13:20:52.32	37.955	-78.002	0.1	-0.99
2011/09/08	13:36:39.34	37.967	-77.936	5.6	0.13
2011/09/08	13:39:49.08	37.966	-77.927	5.7	0.20
2011/09/08	13:45:45.37	37.933	-77.985	4.0	-0.87
2011/09/08	13:54:38.38	37.944	-77.976	2.4	-0.96
2011/09/08	13:59:00.75	37.936	-77.986	4.3	-0.28
2011/09/08	14:27:12.42	37.946	-77.943	7.2	-0.66
2011/09/08	14:27:14.13	37.945	-77.948	0.0	-0.78
2011/09/08	15:00:41.23	37.962	-77.993	-0.1	-0.09
2011/09/08	15:16:57.90	37.912	-77.916	-0.2	-0.70
2011/09/08	15:19:17.91	37.939	-77.986	4.7	0.30
2011/09/08	15:30:54.00	37.916	-77.994	4.3	-0.11
2011/09/08	15:33:26.45	37.943	-77.950	6.0	-0.15
2011/09/08	15:44:44.07	37.948	-77.966	5.4	-0.79
2011/09/08	15:46:43.03	37.944	-77.965	5.6	-0.66
2011/09/08	15:46:44.23	37.946	-77.965	2.2	-0.63
2011/09/08	16:17:54.22	37.940	-77.944	7.2	-0.80
2011/09/08	16:17:55.93	37.939	-77.949	1.3	-0.94
2011/09/08	16:26:22.63	37.939	-77.959	6.1	-0.29
2011/09/08	16:27:27.75	37.948	-77.969	5.7	-0.27
2011/09/08	16:27:33.50	37.914	-77.995	4.1	0.74
2011/09/08	16:34:31.10	37.968	-78.028	0.3	-0.18
2011/09/08	16:55:59.02	37.930	-77.975	5.2	-0.70
2011/09/08	17:05:50.52	37.912	-77.925	-0.1	-0.79
2011/09/08	17:31:57.49	37.911	-77.919	1.0	-0.69
2011/09/08	18:04:24.56	37.912	-77.924	0.5	0.15

* z_0 = −0.4 km

The AIDA Backprojection Earthquake Catalog

Date (YYYY/MM/DD)	**Time (HH:MM:SS)**	**Latitude (°N)**	**Longitude (°E)**	**Depth (km)**	**Magnitude (M_{BPI})**
2011/09/08	18:10:18.89	37.942	-77.986	3.5	-0.60
2011/09/08	18:12:20.42	37.948	-77.981	3.1	-0.45
2011/09/08	18:17:46.49	37.945	-77.976	4.6	-1.05
2011/09/08	18:17:47.42	37.946	-77.969	1.7	-1.01
2011/09/08	18:24:22.43	37.939	-77.986	4.2	-0.89
2011/09/08	18:24:23.35	37.937	-77.987	1.6	-0.95
2011/09/08	18:29:10.85	37.939	-77.987	4.3	0.95
2011/09/08	18:33:54.81	37.955	-77.937	6.9	-0.31
2011/09/08	18:34:03.50	37.939	-77.987	4.6	-0.52
2011/09/08	18:40:43.95	37.948	-77.968	5.3	0.24
2011/09/08	19:00:10.37	37.963	-77.993	1.5	-1.16
2011/09/08	19:19:18.64	37.954	-78.011	0.8	-0.88
2011/09/08	19:22:05.33	37.957	-78.005	0.0	-0.45
2011/09/08	19:32:35.44	37.957	-77.961	4.0	-0.73
2011/09/08	19:32:36.41	37.958	-77.965	-0.1	-0.82
2011/09/08	19:46:15.08	37.941	-77.981	3.9	-0.78
2011/09/08	19:48:47.06	37.903	-78.001	4.9	1.17
2011/09/08	19:49:14.58	37.903	-78.001	5.0	0.97
2011/09/08	20:14:47.47	37.903	-78.001	-0.2	-0.82
2011/09/08	20:21:20.22	37.943	-77.985	3.5	0.16
2011/09/08	20:49:38.45	37.934	-77.982	4.8	0.27
2011/09/08	21:11:17.95	37.960	-77.997	0.8	-0.51
2011/09/08	21:47:17.35	37.923	-77.990	4.4	-0.39
2011/09/08	21:56:17.96	37.959	-77.960	4.1	-0.19
2011/09/08	22:12:44.26	37.962	-77.995	1.1	-0.57
2011/09/08	22:19:42.24	37.923	-78.000	3.7	0.05
2011/09/08	22:23:40.90	37.923	-78.000	3.7	-0.24
2011/09/08	22:38:22.77	37.907	-77.990	5.4	-0.17
2011/09/08	22:39:08.13	37.925	-77.991	4.2	-0.72
2011/09/08	22:49:42.51	37.921	-77.994	3.3	-1.01
2011/09/08	22:58:12.48	37.930	-77.977	5.5	-0.86
2011/09/08	22:58:13.78	37.930	-77.977	0.3	-0.95
2011/09/08	23:02:09.62	37.922	-77.997	3.3	-0.66
2011/09/08	23:07:13.56	37.914	-77.995	3.9	-0.84
2011/09/08	23:07:14.48	37.913	-77.999	0.6	-0.90
2011/09/08	23:09:48.79	37.925	-77.987	3.7	-0.15
2011/09/08	23:14:04.45	37.926	-77.986	3.4	-0.96
2011/09/08	23:41:20.71	37.919	-77.912	0.0	-0.54
2011/09/08	23:46:27.60	37.920	-77.976	6.3	0.98
2011/09/08	23:50:44.22	37.939	-77.980	3.5	0.11

* z_0 = −0.4 km

The AIDA Backprojection Earthquake Catalog

Date (YYYY/MM/DD)	**Time (HH:MM:SS)**	**Latitude (°N)**	**Longitude (°E)**	**Depth (km)**	**Magnitude (M_{BPI})**
2011/09/09	00:29:09.77	37.936	-77.985	3.9	-0.07
2011/09/09	00:35:50.92	37.922	-77.991	3.5	0.45
2011/09/09	01:02:17.15	37.917	-77.923	0.2	-0.45
2011/09/09	01:43:28.27	37.958	-78.000	0.4	-1.07
2011/09/09	01:50:48.81	37.960	-77.995	0.9	-0.01
2011/09/09	01:59:09.62	37.949	-77.957	1.7	-1.02
2011/09/09	02:44:35.65	37.929	-77.967	5.7	-0.16
2011/09/09	02:47:33.29	37.929	-77.986	4.0	0.99
2011/09/09	03:45:29.92	37.916	-78.017	-0.2	-1.19
2011/09/09	04:23:18.35	37.943	-77.975	5.2	-0.41
2011/09/09	04:30:27.73	37.948	-77.967	5.2	-0.75
2011/09/09	04:32:46.84	37.927	-77.989	4.0	-1.09
2011/09/09	04:41:24.28	37.902	-78.000	5.5	-0.33
2011/09/09	04:58:42.82	37.908	-77.992	4.7	-0.68
2011/09/09	05:36:05.87	37.950	-77.964	5.8	1.54
2011/09/09	05:38:35.40	37.949	-77.964	5.6	0.94
2011/09/09	05:49:29.17	37.929	-77.986	4.4	-0.76
2011/09/09	05:52:26.67	37.909	-77.990	5.5	0.01
2011/09/09	06:27:50.82	37.937	-77.949	6.6	-0.97
2011/09/09	07:11:06.26	37.928	-77.990	3.9	-0.33
2011/09/09	07:47:04.84	37.938	-77.981	4.4	-0.26
2011/09/09	08:03:13.48	37.917	-77.992	4.2	0.07
2011/09/09	08:23:33.77	37.948	-77.974	4.8	0.53
2011/09/09	08:25:38.95	37.940	-77.992	1.9	-1.39
2011/09/09	08:55:06.32	37.921	-77.992	3.9	-0.51
2011/09/09	09:05:28.08	37.947	-78.007	1.7	-1.45
2011/09/09	09:16:24.90	37.954	-77.939	6.6	-0.91
2011/09/09	09:16:26.66	37.951	-77.956	0.2	-1.04
2011/09/09	09:24:07.55	37.921	-77.994	3.3	-1.15
2011/09/09	09:53:54.59	37.932	-77.976	5.5	-0.14
2011/09/09	10:32:04.19	37.962	-77.993	0.0	0.17
2011/09/09	10:37:49.26	37.927	-77.989	4.1	-0.56
2011/09/09	11:07:36.25	37.939	-77.987	4.0	-0.77
2011/09/09	11:51:46.85	37.950	-77.965	5.5	-0.89
2011/09/09	11:53:33.47	37.946	-77.990	2.1	-0.29
2011/09/09	12:16:10.09	37.902	-77.999	0.9	-0.99
2011/09/09	12:23:55.31	37.947	-77.974	4.3	-0.35
2011/09/09	12:28:25.27	37.943	-77.968	5.3	-0.74
2011/09/09	12:28:26.50	37.944	-77.969	1.3	-1.04
2011/09/09	12:49:53.99	37.933	-77.985	4.2	-0.14

* z_0 = −0.4 km

The AIDA Backprojection Earthquake Catalog

Date (YYYY/MM/DD)	**Time (HH:MM:SS)**	**Latitude (°N)**	**Longitude (°E)**	**Depth (km)**	**Magnitude (M_{BPI})**
2011/09/09	12:52:43.06	37.914	-78.002	2.9	-0.03
2011/09/09	14:00:45.54	37.939	-77.989	3.4	-0.96
2011/09/09	14:07:40.62	37.939	-77.987	4.2	-0.80
2011/09/09	14:08:37.88	37.939	-77.987	4.1	0.14
2011/09/09	14:10:01.17	37.905	-77.986	5.9	-0.52
2011/09/09	15:10:03.87	37.911	-77.966	8.0	-0.57
2011/09/09	15:16:35.31	37.905	-77.959	8.4	-0.57
2011/09/09	15:19:13.48	37.901	-77.949	8.5	-0.54
2011/09/09	15:21:29.14	37.901	-77.948	8.7	-0.58
2011/09/09	15:24:39.87	37.903	-77.953	8.5	-0.45
2011/09/09	15:27:06.11	37.902	-77.951	6.4	-0.66
2011/09/09	15:39:02.13	37.916	-78.000	7.0	-0.99
2011/09/09	15:40:26.24	37.930	-77.993	5.5	-0.71
2011/09/09	15:45:14.11	37.974	-77.952	5.9	-0.58
2011/09/09	15:49:40.53	37.961	-77.989	7.0	-0.82
2011/09/09	15:50:27.46	37.967	-77.975	8.7	-0.40
2011/09/09	15:53:16.92	37.940	-77.989	3.4	-0.11
2011/09/09	16:09:47.05	37.894	-77.953	8.0	-0.71
2011/09/09	16:10:20.20	37.898	-77.952	6.9	-0.85
2011/09/09	16:10:24.50	37.901	-77.951	8.9	-0.96
2011/09/09	16:11:04.66	37.901	-77.952	4.6	-0.37
2011/09/09	16:33:09.50	37.900	-77.955	8.5	-0.60
2011/09/09	16:45:46.75	37.908	-77.953	8.3	-0.54
2011/09/09	16:53:02.35	37.921	-77.943	8.1	-0.58
2011/09/09	17:00:22.28	37.923	-77.959	8.7	-0.54
2011/09/09	17:30:31.60	37.924	-77.966	5.3	-0.80
2011/09/09	17:33:29.75	37.935	-77.969	8.8	-0.71
2011/09/09	17:36:41.83	37.938	-77.940	8.8	-0.16
2011/09/09	18:08:36.20	37.976	-78.001	0.6	-1.77
2011/09/09	18:26:07.02	37.966	-77.968	8.2	-0.43
2011/09/09	18:27:07.61	37.970	-77.968	7.2	-0.66
2011/09/09	18:27:08.52	37.948	-77.993	2.0	-1.21
2011/09/09	19:59:58.48	37.915	-77.945	8.6	-1.23

* z_0 = −0.4 km

Chapter 5

Conclusion

Chapter 2 shows that EM responses due to spatially correlated, fine scale heterogeneities do not correspond to any classical half-space's response. These responses exhibit an fBm behaviour agreeing with the findings of previous observations, which suggests that not necessarily self-similar, but rather a wider class of spatially correlated heterogeneities may produce fractal-like EM responses. Moreover, degree of the spatial correlation, the contrasts in ground conductivity, and the preferred orientation of multiscale heterogeneity control the fBm behaviour. In addition, β spectral exponent values (1 <) correlates with higher degree of geological roughness and thus may characterize stochastic geologic medium in a compact manner. As a result, there is a need of more observational to confirm the aforementioned results as well as to improve our understanding of the fBm behaviour of observed electromagnetic responses.

Chapter 3 overviews the backprojection method and the influence of the seismic array, noise, and velocity model. The real data examples show the important advantage of the backprojection method over the single-seismogram detection algorithms by improving the signal-to-noise ratio of the weak aftershocks through stacking and enabling event detection that can not be achieved by analyzing individual seismograms. To overcome real data issues including aliased station spacing, inadequate array aperture, inaccurate velocity model, low signal-to-noise ratio, large noise bursts, and varying waveform polarity, four pre-processing methods are evaluated via a systematic comparison to auto-backproject large volumes of data. The comparison results indicate a remarkable success of the use of kurtosis characteristic function on auto-backprojection; however, to estimate magnitudes and additionally to refine spatial resolution, a second backprojection is required using noise-filtered raw waveforms to achieve the best of all criteria. The results also point out that gaps between the array arms, station

spacing, and temporal sampling all limit the spatial resolution of source images; moreover, to improve the velocity model over a complex geology, denser spacing and larger aperture might be required.

Chapter 4 shows the results of the 12-day aftershock catalog derived from the AIDA array and automated back-projection imaging. The AIDA backprojection catalog indicated that the dense array data enables to significantly lower the detection threshold (~ an order of magnitude) and the backprojection imaging improves the signal-to-noise ratio of weak events that cannot be detected on single seismograms. This resulted in an impressive magnitude completeness of M–1.0. A quantitative comparison with the catalog obtained from the co-deployed, unusually large temporal traditional network is presented. The comparison results shows that the dense array catalog indicates a more detailed image of seismicity in the epicentral region and also revealed additional details. The aftershock activity comprising smaller magnitudes do not show a significant change for the frequency-magnitude (b-value) relation and the temporal decay of the sequence; however, these statistics are different at shallow and greater depth, and for different completeness periods. Finally, Chapter 3 and 4 highlight the benefits and capacities of dense aftershock arrays on producing a more complete earthquake catalog.

5.1 Future Research Plan

A recent study (Milliner et al., 2016) indicates that the along-strike co-seismic slip variability is not random; in contrast, it correlates with zones of geometrical fault complexity at all scales. Based on the inferences discussed in Chapter 2, I propose a CSEM data collection

along a fault zone to assess "b-value" variations to test whether there is a correlation between the b-value variability and the fault heterogeneity. This analysis would enable us to better understand the heterogeneity in the stress field.

In Chapter 2, the geoelectrical models do not take account of vertical correlation which would result in variations in signal penetration depth. I propose to evaluate the EM responses of a two-layered conductivity model consisted of a top layer with a spatially-correlated conductivity distribution and a bottom layer with a constant conductivity, to examine the effects of fine-scale heterogeneity on signal penetration depth in rough geological environments. Furthermore, conductivity models that comprise both vertical and horizontal spatial correlations with different degree of spatial correlations, demonstrating a fracture network, can also provide a better understanding of the correlation between the roughness of EM responses and the roughness of fracture network.

Recently, there are studies that focus on stress drops and rupture velocities of small magnitude induced earthquakes (~M 2, e.g. Tomic et al., 2009); however, there is no study that shows the rupture of a tectonic earthquake at small magnitudes. The inefficient temporal and cross-line sampling rates of AIDA do not enable to reveal rupture histories of the largest events (~M2.5 - 3.8) in the catalog. On the other hand, a recent study of Wu et al. (submitted) suggests that some earthquakes in the 2011 Virginia aftershock catalog show low stress drops that may result in larger slip areas. Based on this new finding, I propose to attempt to image a few of these low stress drop events to obtain their slip histories. The AIDA backprojection resolution may become sufficient to image these earthquake sources on their fault planes through adequate time periods that allow to calculate their rupture velocities.

A successful attempt would substantially contribute to our understanding of source scaling.

Finally, I propose a study that uses both dense seismic array and CSEM monitoring for a seismically active zone for sufficient time periods with adequate spatial sampling rates. While dense array data can be used to locate earthquakes at very small magnitudes and illuminate fault zones in detail, monitoring temporal changes in fractal properties of EM signals may provide complementary information about the propagation of the aftershocks and the fault zone heterogeneity. Both will enable a better understanding of stress and strain evolution, earthquake triggering, earthquake mechanisms.

References

Tomic, J., Abercrombie, R.E.& Do Nascimento, A.F., 2009. Source parameters and rupture velocity of small M<=2.1 reservoir induced earthquakes. *Geophysical Journal International*, **179**, 2, 1013–1023.

Milliner, C. W. D., Sammis, C., Allam, A. A., Dolan, J. F., Hollingsworth, J., Leprince, S., & Ayoub, F., 2016. Resolving fine-scale heterogeneity of co-seismic slip and the relation to fault structure. *Scientific reports*, 6.

Wu, Q. & Chapman, M. C., 2017. Stress Drop Estimates and Source Scaling of the 2011 Mineral, Virginia Mainshock and Aftershocks. Submitted to *Bull. Seismol. Soc. Am.*